Manufacturability and material properties of the bimetallic material of stainless steel 316L and nickel-based superalloy Inconel 718 fabricated via laser-based powder bed fusion

Master's thesis
University of Turku
Physics
2026
B.Sc. Eetu Valtonen
Supervisors:
Professor Antti Salminen
Docent Matti Murtomaa
Associate Professor Ashish Ganvir

The originality of this thesis has been checked in accordance with the University of Turku quality assurance system using Turnitin Originality Check service.

UNIVERSITY OF TURKU
Department of Physics and Astronomy
VALTONEN, EETU Manufacturability and material properties of the bimetallic material of stainless steel 316L and nickel-based superalloy Inconel 718 fabricated via laser-based powder bed fusion.

Master's Thesis, 90 pp.
Physics
March 2026

Additive manufacturing (AM), also known as industrial three dimensional (3D) printing, is a modern production method which manufactures a workpiece directly from a digital model, often layer by layer. This method allows for designs and geometries which are prohibitively complex to manufacture using conventional techniques. Bimetallic objects are defined as consisting of two metals that are joined together and AM of bimetals is the practice of using AM techniques to produce bimetallic objects. Stainless steel 316L (316L) is a widely used cost effective alloy with good material properties for industrial applications. Nickel-based superalloy Inconel 718 (IN718) is a high-performance superalloy used in demanding conditions. The bimetallic combination of 316L-IN718 is a high-performance material combination for nuclear energy and aerospace applications, for which additive manufacturing has been proposed as a viable method of production.

The aim of this thesis is to establish an understanding of the additive manufacturing of bimetallic 316-IN718 via laser-based powder bed fusion. The thesis aims to study the additive manufacturing process for bimetallic 316L-IN718 and the properties of 316L-IN718 manufactured by laser-based powder bed fusion. This includes the study of the parameters used to manufacture IN718 onto an additively manufactured 316L substrate as well as the study of manufactured 316L-IN718 workpieces in laboratory measurements. Research is conducted to determine the manufacturability of the bimetallic combination of 316L-IN718, as well as determine the effect of an IN718 focused heat treatment plan on the properties and characteristics of the bimetallic combination.

Main findings include the successful additive manufacture of 316L-IN718 via laser-based powder bed fusion, as well as the influence of the IN718 heat treatment on the bimetallic material properties: porosity, microstructure, geometrical accuracy, hardness, corrosion rate. Hardness and corrosion rate results are compared to values found in literature and observed behavior is compared with theoretical understanding. Heat treatment is observed to cause a notable increase to the hardness of IN718 while having a minor negative effect on the hardness of 316L, with the interface gaining a minor positive effect. Heat treatment is observed to increase corrosion rate for IN718, 316L and the interface.

Future research is suggested to focus on further study of the corrosion behavior as well as dilatometry, fatigue investigation, computed tomography, residual stress analysis and helium leak tests. Overall, this thesis provides an overview of laser-based powder bed fusion, the bimetallic combination of 316L-IN718 as well as its properties and characteristics when manufactured via laser-based powder bed fusion.

Keywords: Additive manufacturing, AM, laser-based powder bed fusion of metals, PBF-LB\M, bimetal, Nickel-based superalloy Inconel 718, INCONEL718, IN718, Stainless steel 316L, SS316L, 316L, process parameters, material properties

Nomenclature:

Symbol	Explanation
A	Area of the impression (mm^2)
CI	Confidence interval (1)
$CI_{95\%}$	95% Confidence interval (1)
d_1	First diagonal of the impression (mm)
d_2	Second diagonal of the impression (mm)
d_{BP}	Diameter of the building platform (mm)
E	Potential (V)
E_{eq}	Equilibrium potential (V)
E_V	Volumetric energy density (J/m^3)
e	Index of the element in alloy (1)
F	Faraday constant (As/mol)
H	Hardness (kgf/mm^2)
HV	Vickers hardness (kgf/mm^2)
HV0.5	Vickers hardness with a 0.5 kgf load (kgf/mm^2)
HV1	Vickers hardness with a 1 kgf load (kgf/mm^2)
HV10	Vickers hardness with a 10 kgf load (kgf/mm^2)
h	Hatch spacing (µm)
i	Current density (A/m^2)
i_0	Exchange current density (A/m^2)
I	Current (mA)
I_0	Exchange current (mA)
M	Load with which the impression is made (kgf)
$M_{E,alloy}$	Equivalent weight (or equivalent mass) of the alloy (g)
$\bar{m}_{a,alloy}$	Average molar mass of the alloy (g)
$m_{a,e}$	Molar mass of an element in alloy (g)
m_{BP}	Margin for the building platform (mm)
m_S	Margin for a workpiece (mm)
n	Number of elements in alloy at or above 1% prevalence (1)
n_{FVE}	Number of free valence electrons for the alloy (1)
n_{wp}	Number of workpieces (1)
P	Laser power (W)

P_e	Prevalence of the element in alloy (1)
p_a	Number of pixels in total (1)
p_p	Number of pore-representing pixels (1)
R	Gas constant (J/(mol K))
T	Temperature (K)
t	Layer thickness (μm)
V_a	Apparent volume (mm^3)
V_p	Pore volume (mm^3)
v	Scanning speed (mm/s)
X	Sample population size (1)
x	Sample value (1)
$\bar{x}$	Sample population mean (1)
z	Confidence level value (1)
z_e	Number of electrons involved in the electrode reaction (1)
α_a	Transfer coefficient for anodic reactions (1)
α_c	Transfer coefficient for cathodic reactions (1)
ρ_{316L}	Density of 316L (g/cm3)
ρ_{BM}	Density of bimetallic combination of 316L and IN718 (g/cm3)
ρ_{IN718}	Density of IN718 (g/cm3)
σ	Population standard deviation (1)
τ	Time (s)
φ	Porosity (%)
φ_{316L}	Porosity measured from the bulk 316L (%)
φ_{BM}	Porosity measured from the bimetallic interface (%)
φ_{IN718}	Porosity measured from the bulk IN718 (%)
$\varphi_{\Delta BM}$	Difference between the porosity measured from the bimetallic interface and the mean average of the porosities measured from the bulk 316L and bulk IN718 (%)

Abbreviations	Explanation
AB	As-built
AM	Additive manufacturing
AMed	Additively manufactured
CAD	Computer assisted design
HT	Heat-treated
IN718	Nickel-based superalloy Inconel 718
PBF-LB	Laser-based powder bed fusion
PBF-LB\M	Laser-based powder bed fusion manufacturing of metals
3D	Three-dimensional
316L	Stainless steel 316L

Table of contents

1 Introduction

The additive manufacturing (AM) of metal has been a growing trend in the manufacturing industry as of late. [1] Additive manufacturing — also known as industrial three-dimensional (3D) printing — is a method of manufacture in which material is added, joined or deposited together in an iterative process to manufacture a final workpiece, often layer by layer.

AM technology has advantages over conventional reshaping-based or removal-based manufacturing methods. AM allows for linear production costs for cost-efficient small-scale production. [2] AM is useful in the manufacture of replacement parts, due to not needing a long supply chain for any given part, only the three-dimensional (3D) model and the AM machine and material. [3] This would be especially useful for machines which no longer have the support of conventional manufacture of repair parts due to, for example, the supply chain or the production lines being discontinued. AM can also be used to repair a damaged part directly instead of the fabrication of a completely new replacement part. [1]

AM also makes previously challenging levels of detail more achievable, such as specific microstructures and surfaces within a part. [1] Additionally, AM allows increased complexity due to the increased degrees of freedom in the manufacturing process compared to conventional removal or reshaping based manufacturing processes. [1] For example: AM technologies are also used in biomedicine for the production of bone implants, utilizing the aforementioned advantages of AM to make customizable, small-production scale products which would be complex to produce with conventional manufacturing methods. [4]

Additive manufacturing of multimaterials is defined in this thesis as AM used in the manufacture of a workpiece which utilizes multiple materials. Bimetallic AM is defined in this thesis as the manufacture of a workpiece utilizing two metals.

Bimetallic AM allows manufacturing of different types of bimetals: similar and dissimilar. Similar metals are defined in this thesis as metals which have similar physical properties and have similar elemental composition. Dissimilar metals are defined in this thesis as metals which have differing physical properties and elemental compositions.

The AM of similar metals would be useful in repair of broken parts, where the original parts were made without bimetallic features. [1]

The study of AM of dissimilar metals is suitable for novel designs and innovation, as it can be used to manufacture complex pieces with a material specific to the function of a given portion. [1]

The manufacture of metal pieces via AM has been under extensive study already, as seen in Figure 1.

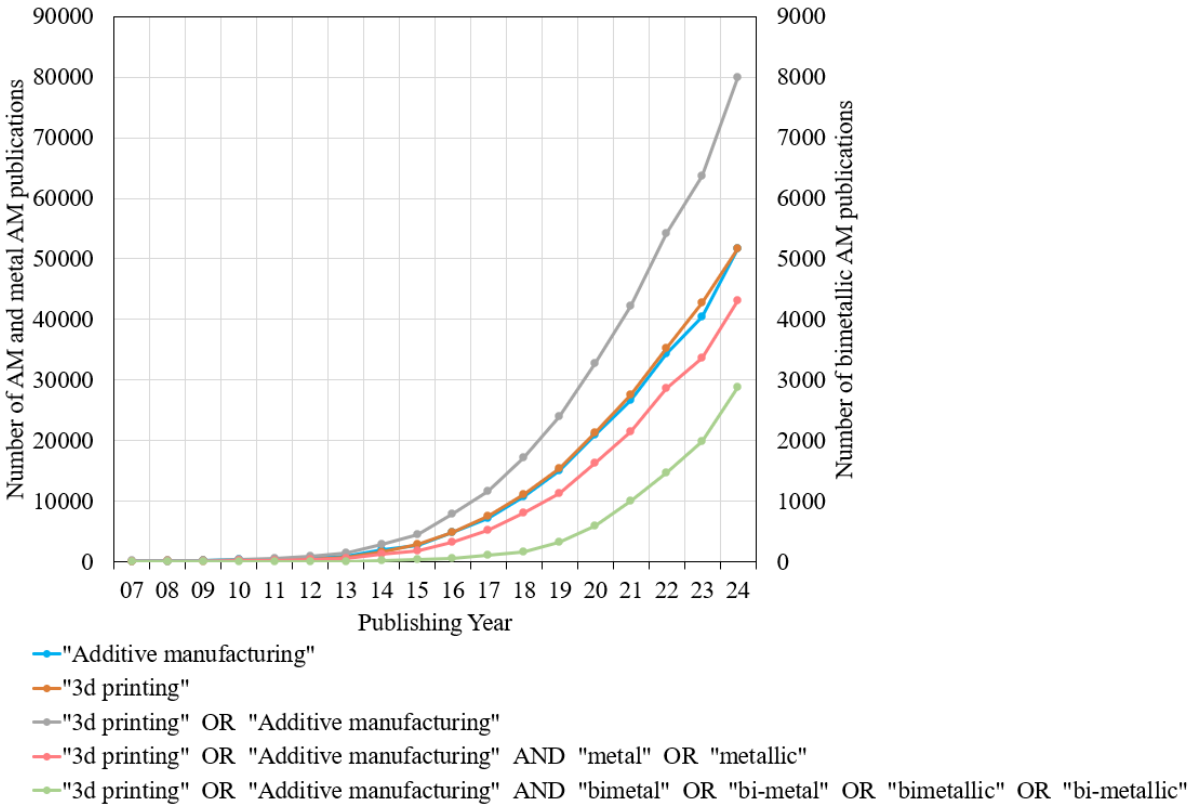

Figure 1. Research landscape of bimetal AM from 2007 to 2024 according to different search queries and keywords on Scopus. The right vertical axis is for the bimetallic results, while the left vertical axis is for the rest.

However, the use of bimetals is yet to be studied with similar rigor, as can be seen in Figure 1. This could be so because the technology naturally requires understanding of the process for single metals before it can be applied to bimetals effectively.

Figure 1 shows that the number of publications of metal AM is approximately half of the number of all AM publications. Furthermore, the number of bimetal AM publications can be seen to follow a similar curve to metal AM. The number of bimetal publications seems to follow a pattern of being one tenth of the number of metal AM publications from two years prior.

Research into laser-based powder bed fusion (PBF-LB) of dissimilar metals has seen a rise in the 2020s. This can be seen in Figure 2. [1] Figure 2 a) shows that PBF-LB research for dissimilar metals begun to grow in prominence in 2019, and Figure 2 b) shows that hardness and tensile properties are the two most common properties to be studied. Figure 2 c) shows that the most prominent metals used in the study of dissimilar metals are steels combined with either copper-based materials or Inconels.

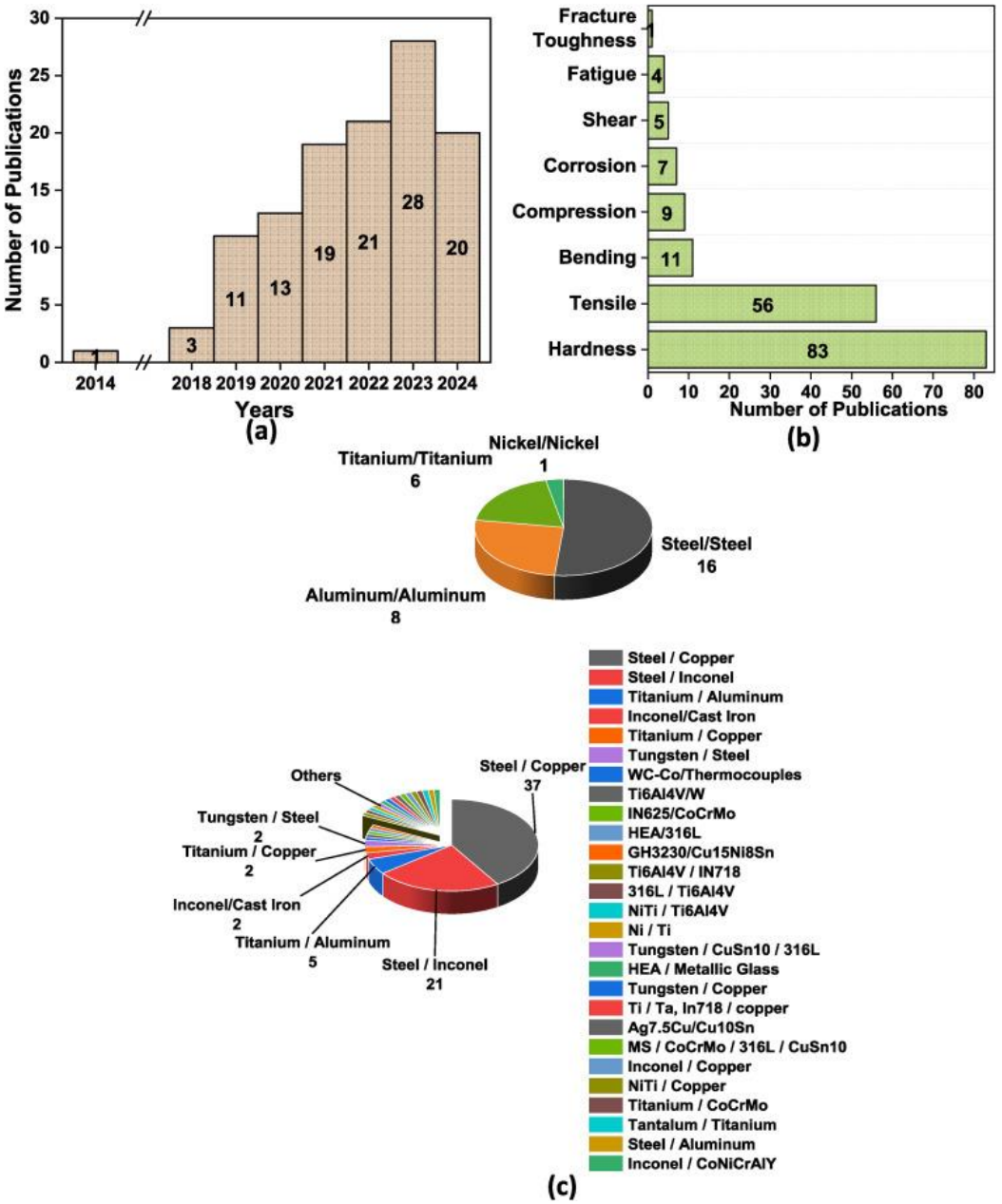

Figure 2. Figure detailing the research landscape of bimetal AM via laser-based powder bed fusion during the time from the year 2014 to the June of 2024.
a) Displays the number of publications on the topic per annum.
b) Displays the properties studied in the publications.
c) Displays the material combinations studied in the publications. [1]
Image: Ibrahim H. ZainElabdeen [1]

1.1 Aim and purpose of thesis

This thesis aims to study the bimetallic material combination of stainless steel 316L (316L) and nickel-based superalloy Inconel 718 (IN718) which are additively manufactured (AMed) via PBF-LB\M. The PBF-LB\M manufacturing process is studied via a review of the relevant literature and experimental tests and observations.

The scientific relevance of this thesis lies in the innovative nature of PBF-LB\M of dissimilar metals, as research on the topic as a whole is still rather limited. Research on the properties of the bimetallic combination of 316L-IN718 manufactured via PBF-LB\M is also limited. Additionally, this thesis contributes to the understanding of metallurgical compatibility as well as interface bonding in PBF-LB\M technology.

The industrial relevance in this thesis lies in the aforementioned innovative nature of the PBF-LB\M of dissimilar metals, as the technology allows for novel designs and applications. Especially the specific material combination of 316L-IN718 is of interest due to the combination being used in highly demanding applications. The combination of the high level of material performance and the possibilities afforded by the PBF-LB\M technology in design allow for lucrative opportunities for industry.

This thesis is a part of an industrial project, wherein the project shareholders: Wärtsilä, Valmet, Bluefors, Patria and EOS investigated and studied bimetal additive manufacturing. The “Bimetallic Research Project” focused on the “testing and characterization of bimetallic materials manufactured by laser-based powder bed fusion technology”. The goal of the project, as well as this thesis, was to create a knowledge basis for bimetallic PBF-LB\M from both a process as well as material properties point of view.

1.2 Research questions

This thesis answers five research questions:

- What is the level of manufacturability of the bimetallic combination of 316L-IN718 using the PBF-LB\M process? Can the materials be joined together reliably and effectively using the process?
- What are the material properties and physical characteristics of the bimetallic combination of 316L-IN718 manufactured via PBF-LB\M? The material properties and physical characteristics of concern being: porosity, microstructure, geometrical accuracy, hardness and corrosion behavior.
- How does the heat treatment of IN718 influence the material properties and physical characteristics of the bimetallic 316L-IN718 manufactured via PBF-LB\M? What effects does the heat treatment have on the performance and measurements of the alloys and the interface?
- What is the theoretical basis behind the behavior measured for porosity, microstructure, geometrical accuracy, hardness and corrosion behavior?
- How do the results and behavior observed of the porosity, microstructure, hardness and corrosion behavior measurements compare with results in the literature?

1.3 Research methods

PBF-LB\M manufacturing parameters for IN718 built on top of 316L are studied and evaluated by experimental testing. The study of the material combination will be performed via bimetallic 316L-IN718 workpieces. The workpieces are manufactured with PBF-LB\M by first manufacturing the 316L portion via PBF-LB\M and then using PBF-LB\M to manufacture IN718 on top of the 316L material. The quality of the bimetallic interface and manufactured IN718 is evaluated for each workpiece. A process of elimination is employed to select the parameters used in the production of the highest quality workpiece.

The experimental tests and observations on the bimetallic material combination of 316L-IN718 will be performed on a set of workpieces manufactured with the parameters corresponding to the highest quality workpiece determined in the process of elimination. Half

of the workpieces will receive heat treatment according to an IN718 heat treatment plan to allow for the study of the effect of the heat treatment on the bimetallic material combination.

The AMed bimetallic material combination of 316L-IN718 is measured for porosity, hardness, geometrical accuracy and corrosion rate in experimental tests. Observations of the porosity and microstructure of the material combination are made using microscopy. Furthermore, the influence of an IN718 heat treatment plan for the bimetallic material is determined by repeating each measurement for as-built workpieces as well as heat-treated ones.

Porosity is measured via data-analysis of micrographs of the manufactured 316L-IN718 workpieces after they are set in an epoxy cast, ground and polished.

The geometrical accuracy is measured with a 3D surface analysis microscope and determined with analysis of the measurement data.

The hardness is measured with a Vickers hardness tester after the workpieces are set in an epoxy cast, ground and polished.

The corrosion rate is measured with a potentiostat by cutting the workpieces into three types of corrosion sample: 316L, IN718 and bimetallic 316L-IN718. The corrosion samples are then soldered to copper wire, cast in epoxy, ground and polished. The potentiostat is set up utilizing a corrosion sample as the working electrode, a Ag/AgCl reference electrode and a graphite auxiliary electrode. All electrodes are held in NaCl solution and the measurement is performed for each corrosion sample. The potentiostat performs a linear sweep voltammetry, the data of which is then analysed.

Statistical analysis is performed on the porosity and hardness measurement results. The results of the experiments will be compared to values in relevant literature.

1.4 Limitations

This thesis is a general overview on the topic of PBF-LB\M and the bimetallic material combination of 316L-IN718. As such this thesis could be further analysed from a more focused material physics, metallurgy, thermodynamics or electrokinetics point of view, or from a production quality point of view.

This thesis does not contain observations of the crystallographic orientation within the studied materials and as they are out of the scope of the thesis. Due to the limitations of schedule and circumstance, this thesis will not contain dilatometry analysis or wear and tensile tests.

This thesis provides a general overview of the potential of additive manufacturing and especially PBF-LB\M, but does not consider business case calculations e.g.: production time. PBF-LB\M is chosen as the technique for this thesis due to it being the most widely used AM technology as well as its cost effectiveness and versatility in material selection. [5]
The selection of the material combination of 316L-IN718 was made due to the interest of the project shareholders in the material combination.

2 Background

AM is the practice of using an iterative process where small portions are joined to the manufactured piece incrementally, thus producing the final piece. [1] The method of AM studied in this thesis is laser-based powder bed fusion of metals (PBF-LB\M). PBF-LB\M is performed by a laser beam introducing focused thermal energy on a powder bed, causing the laser beam to heat a small volume of the powder to its melting point, forming a melt pool. [6] The PBF-LB\M method is illustrated in Figure 3.

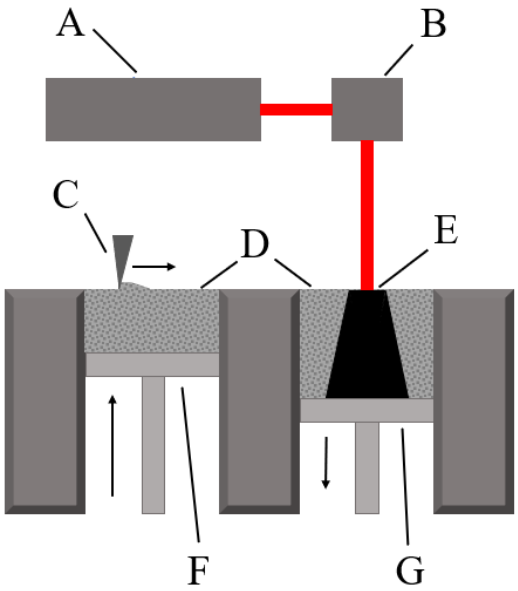

Figure 3. Illustration of the PBF-LB\M process. Figure illustrated based on reference. [7]
A) Laser
B) Mirror scanner
C) Recoating blade
D) Powder
E) Workpiece
F) Powder supply platform
G) Building platform

In Figure 3 the laser source (A) emits the laser beam which the mirror scanner (B) then reflects onto the powder bed below to a desired position and pattern. The beam melts the powder (D) and the molten powder is fused into the workpiece (E) as it solidifies. Once the desired portion of the powder bed is fused, the building platform (G) is lowered to allow for an additional layer of powder to be spread on top of the previous powder bed. The powder supply platform (F) rises so that the recoating blade (C) can move more powder (D) to make a new bed of powder to melt. [7]

Powder has lower thermal conductivity compared to solid metal. [8] Due to this difference in conductivity, most thermal energy is conducted away via the solid metal portion of a given PBF-LB\M workpiece being manufactured.

When the thermal energy is transferred away from the melt pool, it cools and solidifies, joining into the manufactured part. This is illustrated in Figure 4.

In Figure 4 the laser beam is focused onto the top surface of the powder bed, and the thermal energy introduced by the laser beam heats the powder, causing it to melt. This melting forms a melt pool. As the laser beam moves across the powder bed along the scan path, it melts and as such fuses a track or a scan track to the already built workpiece. [7]

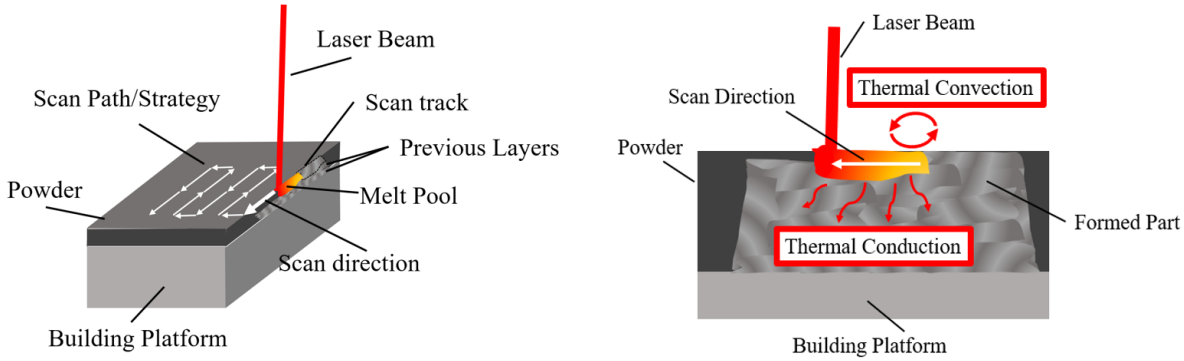

Figure 4. The diagram for the process of PBF-LB\M.
Figure illustrated based on reference. [7]

To manufacture a desired workpiece or part with PBF-LB\M, first a computer assisted design (CAD) file is made, which represents the digital three-dimensional (3D) model of the workpiece, this is illustrated in Figure 5.

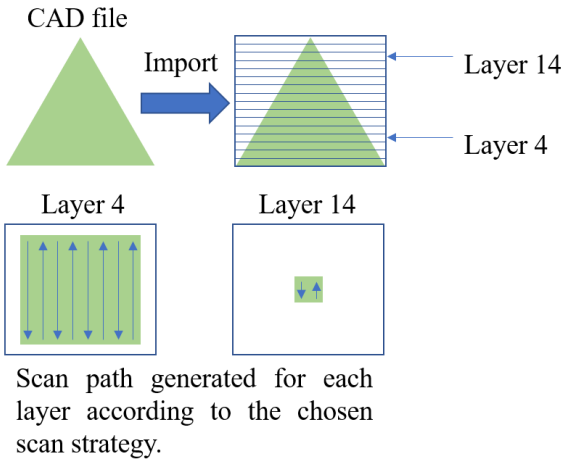

Figure 5. The CAD file is imported to the PBF-LB\M machine software, and it is sliced to layers, and a scan path for the laser beam is generated for each layer.

As Figure 5 illustrates, the CAD file of the digital 3D model of the workpiece is imported to the PBF-LB\M machine software. In the software, the model is sliced into horizontal layers. The height of the layers represents the thickness of each powder bed layer that will be spread on top of the building platform and the previous layers during the PBF-LB\M process. A scan path for the laser beam is generated for each horizontal layer of the digital 3D model by using scan lines. The act of filling an area of a layer with a dense group of scan lines is called hatching. [9] Each hatching follows a given hatching strategy, examples of which can be seen in Figure 6.

The combination of hatching strategy and process parameters such as laser power and layer thickness is called a scan strategy. [9] Scan strategies can also include layer-to-layer differences, such as rotation between layers. [10]

In reality, typical layer height, hatch spacing settings and workpiece size would require vastly more layers and scan lines than what is illustrated in Figure 5.

A contour may be used in the generation of the scan path for each layer. A contour is a scan path which functions as the outline for a hatching. Hatched scan paths can follow different kinds of hatching strategies such as a linear or a concentric strategy, which can be seen in Figure 6 a) and b).

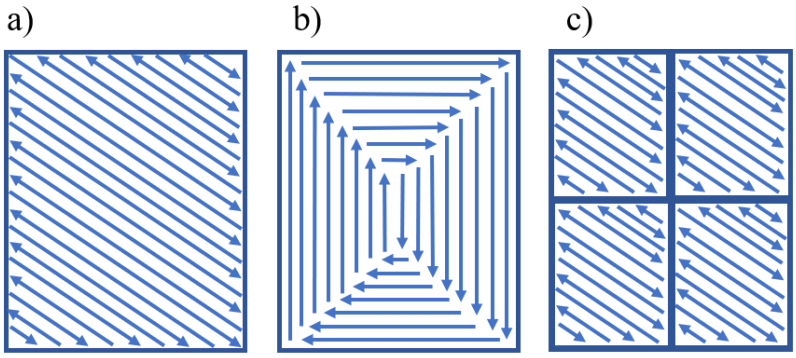

Figure 6. Different hatching strategies used in PBF-LB\M. Figure illustrated based on references. [9], [10]
a) Linear strategy
b) Concentric strategy
c) Islands with linear strategy.

Figure 6 illustrates different hatching strategies. Figure 6 a) shows the linear strategy, where the scan path goes back and forth. Figure 6 b) shows a concentric strategy, where the scan path rotates 90° to the right each time it meets an earlier scan line or the contour.
Figure 6 c) shows a linear strategy with islands, where a given area is divided into smaller regions, called islands, which all have their own hatched scan paths. [9], [10]

Due to its iterative and additive nature, AM can be used to manufacture workpieces with more complex geometries due to the increased number of degrees of freedom compared to conventional manufacturing methods such as removal and reshaping based manufacturing. [1]

Examples of this could be intricate internal designs which utilize topological optimization. Topological optimization is the practice of computing an optimal configuration for a structure for a given set of requirements and criteria. [11] Topological optimization allows for internal geometries which can, for example: minimize turbulence in flow of liquid [12], maximize heat sink effectiveness [13], [14] and minimize the weight and material needed for a stress-bearing component. [11] Examples of topological optimization are shown in Figure 7 and Figure 8.

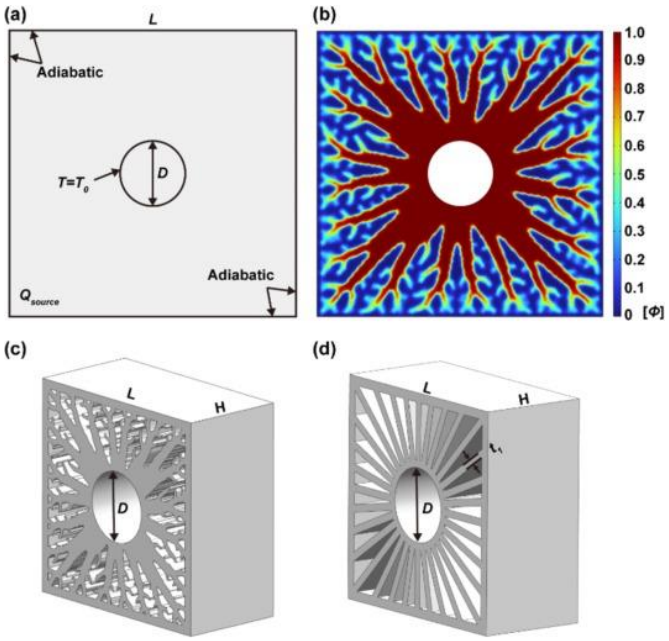

Figure 7. A topologically optimized heat sink. [13] Image: Xiaoqiang Wang [13]

Figure 7 showcases a topologically optimized heat sink. A conventional design is shown in Figure 7 d). Topological optimization is used to determine a complex internal design for the heat sink, seen in Figure 7 c). The optimization is performed by using iterative computation to simulate which geometry for the heat sink internals would conduct thermal energy away effectively, illustrated in Figure 7 b). The design allows for the heat sink to have the same external dimensions and boundary conditions — seen in Figure 7 a) — as a conventionally manufactured heat sink whilst also possessing a higher level of performance. This is due to the optimized topology allowing for increased heat transfer. [13]

Figure 8 shows a topologically optimized microchannel heat sink. The geometry of the microchannels in the heat sink were topologically optimized. The optimization improved the hydrothermal performance of the heat sink as the porous ribs cause disruption to the thermal boundary layer. [14] The thermal boundary layers being the layer after which the temperature of a liquid begins to experience a gradient from the temperature of the bulk of the liquid to the temperature of the wall as the wall is approached. [15]

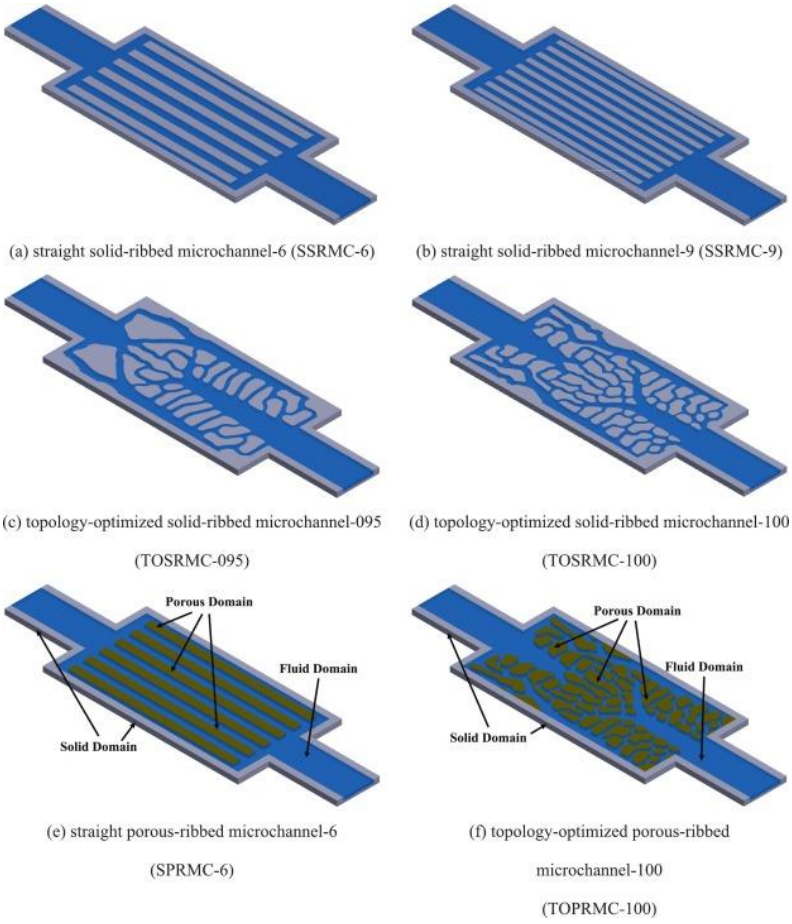

Figure 8. A topologically optimized microchannel heat sink, which can be used to cool down microchips. [14] Image: Kailu Cui [14]

The already intriguing opportunities of AM are further expanded once multi-material pieces are considered. Examples of potential applications for bimetallic 316L and IN718 are a hot-side heat exchanger for fission surface power systems [16] and as pressure tubes for nuclear fission reactors. [17]

3 PBF-LB\M

The process of PBF-LB\M has challenges and considerations in addition to its advantages. Considerations such as the selection of manufacturing parameters as well as design of the workpiece are important. Proper parameter selection results in lowering the risk of defects and outright failure. [18] Overhangs are a limitation of PBF-LB\M design and unsupported overhangs are to be avoided in workpiece design. [19]

Overhangs are illustrated in Figure 9.

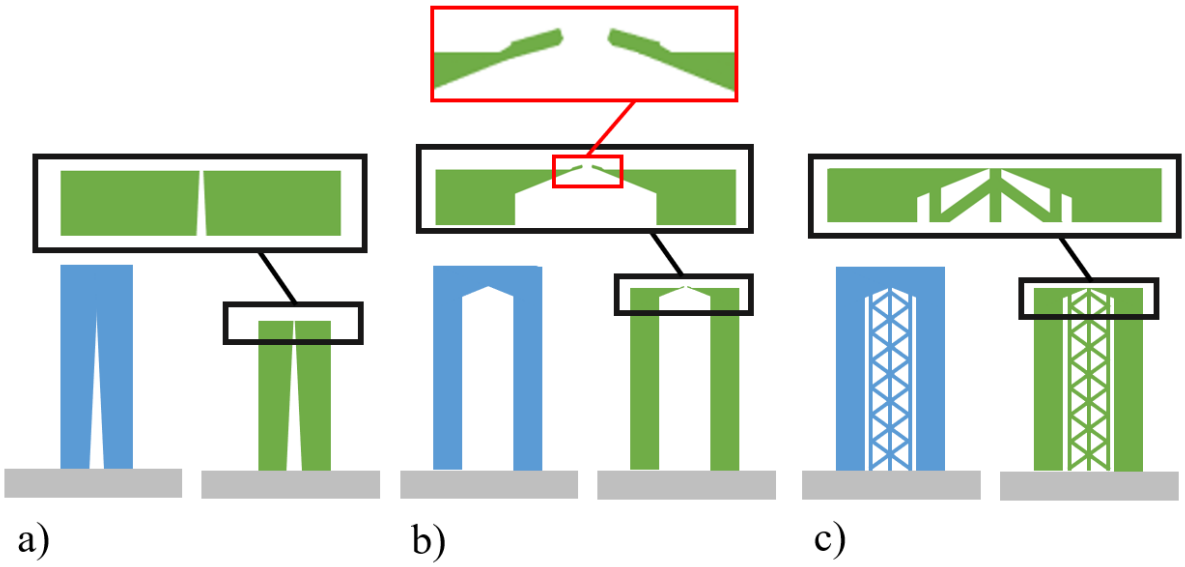

Figure 9. An illustration of the problem of overhangs.
a-c) The CAD file of the 3D model on the left in blue, with the workpiece being built on the right in green.
a) shows a steep enough angle for the overhang, no defects or issues experienced.
b) shows too shallow an angle for the overhang, causing a warping defect, which hinders recoating.
c) shows a shallow angle for the overhang but which is supported by a support structure, preventing warping.

As can be seen in Figure 9, an overhang is a portion of the design which has too little support from previously built layers. A design with an overhang that would cause a defect during fabrication can be modified to contain a support structure. Support structures prevent defects that are caused by overhangs, as illustrated in Figure 9 c). An overhang that is gradual enough can be readily manufactured, as seen in Figure 9 a).

Overhangs that are too shallow experience warping due to the thermal stresses involved in the PBF-LB\M process causing material yielding, leading to distortion and warpage. [20] Overhangs also suffer from dross formation due to the sinking of the melt pool, melt pool sinking being caused by the lack of a solid previously built layer below the melt pool. [20]

As such, designs which contain unsupported overhangs risk structural weaknesses in the finished workpiece or outright failure of the building process. The workpieces in this thesis were self-supporting and as such did not need supports.

Metal powders have properties — such as reflectivity or absorptivity — that need to be taken into account when using PBF-LB\M. The thermal energy which the laser beam can input into powders with high reflectivity is lower compared to powders with low reflectivity. [21] Furthermore, it is important to know how well the formed part's material will conduct heat away from the melt pool. Powders are all less thermally conductive than a solid piece of a given material. [22] This is due to the fact that powder particles are insulated by the atmosphere between powder particles, and that particle-to-particle heat transfer bandwidth is lower compared to bulk material due to the transfer area being close to a sphere-sphere contact area. [22]

There are many considerations during this process, for example: powder spreading dynamics to instability of the melt pool, Marangoni flow and spattering. Powder spreading dynamics are studied out of concern for the even spreading of the powder when recoating it on the building platform and on a previous layer. Instability of the melt pool is naturally undesirable due to the loss of predictability of the process, but also because a stable melt pool lowers the risk for structural weaknesses due to a reduction in porosity. [23] Marangoni flow is fluid motion caused by the high temperature gradients present in PBF-LB\M. These temperature gradients cause surface tension gradients, which causes Marangoni stress in the molten metal — this stress causing Marangoni flow in the melt pool. Marangoni flow is one of the key factors in melt pool behavior, and as such it is important to be taken into account in PBF-LB\M. [24] Spattering is the ejection of powder due to vapor jetting caused by the evaporation of metal. Spattered powder is noted as being a source of porosity. [25]

3.1 Laser-based powder bed fusion of metals for dissimilar alloys

Due to fact that PBF-LB\M for dissimilar alloys involves materials which may possess differing properties, special consideration must be given for the interface between the alloys. Consideration ought to be given to, for example:

- how well the interface between the materials will respond to the potentially different volumetric energy densities preferred for each material;

- would the two different materials combine together to form intermetallic compounds and could said compounds be potential structural weaknesses;

- would one of the two materials be better suited to be the substrate upon which the other is joined to avoid potential issues. For example: the softer and weaker material could be the one which is built directly onto the building platform, allowing for easier removal.

There are different types of interfaces between materials, such as:

- Bimaterial, where the interface changes from one material to the next without grading.
- Functionally graded, where the interface changes from one material to the next gradually, usually by the powders being mixed in specific ratios.
- Multimaterial with interlayer, where there is a third material that forms a thin interface with the two other materials. [1]

These are illustrated in Figure 10.

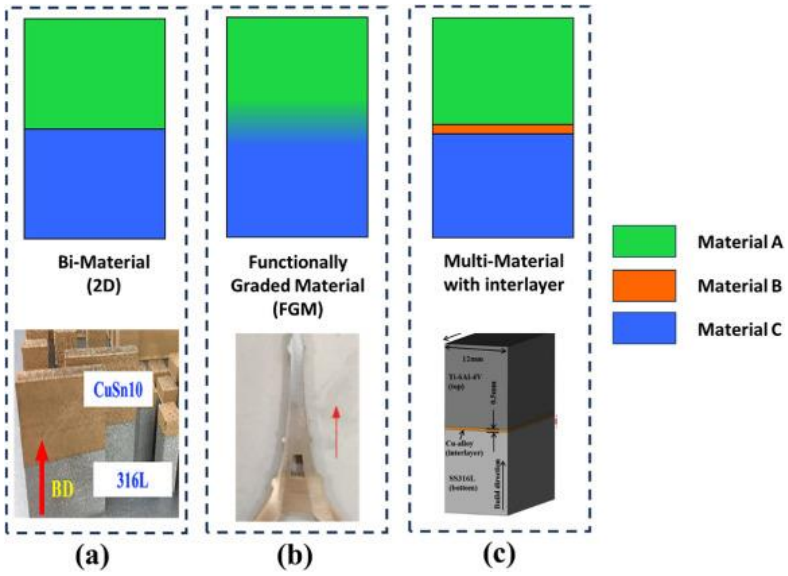

Figure 10. Illustrations for the different kinds of interfaces: a) bimaterial, b) functionally graded and c) multimaterial with interlayer. [1] Image: Ibrahim H. ZainElabdeen [1]

In this thesis, the AMed 316L-IN718 bimetallic workpieces are manufactured as bimaterial ones, similar to the illustration of Figure 10 a). This selection was made due to its simplicity to narrow the number of variables that had to be considered when planning and preparing the experiments.

3.2 Build parameters for PBF-LB\M

Parameter selection is to be done carefully, because values which correspond to too low or too high volumetric energy density risk defect formation. [26] Lack-of-fusion porosity and keyhole porosity are examples of defects caused by improper parameter selection. Lack-of-fusion porosity is caused by the inability of the material to fuse together due to too low energy density. Keyholing porosity occurs when excessive energy density causes vaporization which then leads to porosity. [27]

The parameters in a PBF-LB\M process are as follows:

- Thickness (*t*, layer thickness, µm) describes the height of the powder bed which is rolled or coated onto the building platform or on top of previous layers.
- Power (*P*, laser power, W) describes the amount of power the laser beam has.
- Speed (*v*, scanning speed, mm/s) describes the speed at which the laser beam travels the scan path on the powder bed.
- Hatch (*h*, hatch spacing, µm) describes the minimum distance between two scan lines in a scan path.
- Spot size (*d*, spot diameter, µm) describes the diameter of the laser beam on the surface of the powder bed.

The energy input of a laser beam into a powder bed is calculated via volumetric energy density (E_V) according to Equation 1: [28]

$$E_V = \frac{P}{vht} \quad (1)$$

Where *P* is the power of the laser beam, *v* is the scanning speed of the laser beam, *h* is the hatch spacing for the scan path and *t* is the layer thickness of the powder bed.

High laser power is the parameter most connected to build speed [29], due to higher laser powers allowing for increased scanning speeds whilst maintaining effective volumetric energy density. Build speed being the rate at which volume can be manufactured using PBF-LB\M.

However, high laser power (1000 W) may be responsible for crack formation. [29] Increased laser power could make the system more vulnerable to defect formation if other parameters are not carefully selected, due to increased energy input causing volatility in the system.

4 Materials

This chapter explores the materials used in this thesis.

The materials used in PBF-LB\M differ from those used in conventional manufacturing mainly due to the material being powder instead of — for example — solid sheets. Additionally, some materials such as IN718 are difficult to machine with conventional methods. [30] Due to the difficulties of conventional manufacturing methods such as cutting [30] the use of PBF-LB\M or other AM methods to manufacture IN718 is made more appealing.

4.1 Stainless steel 316L

Stainless steel 316L is a widely used metal, due to its desirable properties such as its corrosion resistance, strength and plasticity. [29] Huang et al. noted that the study of PBF-LB for the purposes of manufacturing 316L has been under extensive study. [29]

Stainless steel is preferrable in piping and steam-generating plants as well as other medium-to-high temperature environments due to its high resistance to corrosion and fatigue and good mechanical properties, in addition to its cost-effectiveness. [31]

Table 1 shows build parameters of 316L manufactured via PBF-LB\M upon a substrate of IN718 and their calculated volumetric energy densities from different literature sources.

Table 1. The list of parameters used to fabricate 316L upon an IN718 substrate.

AM Parameters					Ref.
P [W]	v [mm/s]	h [µm]	t [µm]	E_V [J/m^3]	
320	650	140	50	7.03E+10	[32]
175-225	550-640	120	50	-	[33]
90	700	56	40	5.74E+10	[34]
Average:				6.39E+10	

Table 1 shows the volumetric energy density calculated with Equation 1. It is worth noting that the usefulness of volumetric energy density is shown in Table 1, due to the fact that it allows for some comparison between parameter profiles which are different in every parameter, yet may still be similar in energy density.

Steel alloys manufactured by PBF-LB\M are observed to have a tortuous interface pattern. [1] An example of this can be seen in Figure 11 b).

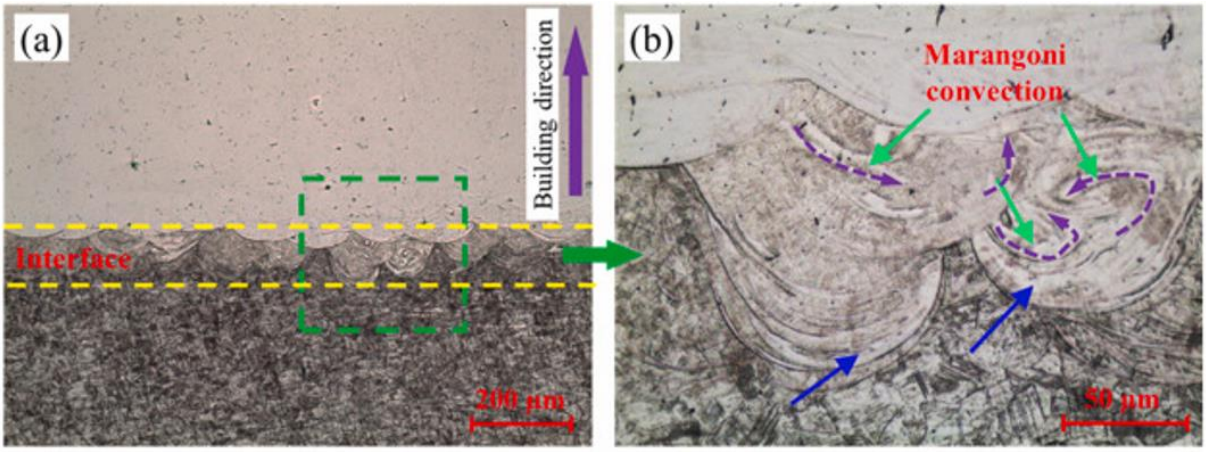

Figure 11. Micrographs of a bimetallic CrMn stainless steel and maraging steel 1 interface. Made by fabricating maraging steel 1 using PBF-LB\M on top of cast CrMn stainless steel. Optical micrographs of a) low b) high magnification are provided.
Note the Marangoni convection behavior seen in the steel-steel interface. [35] Image: Yuchao Bai [35]

As can be seen from Figure 11 b) the Marangoni convection causes specific spiral patterns in the cross-section, seen at the interface. There are three clear different layers which can be identified from Figure 11 b), as round patterns overlapping each other. Notice that in Figure 11 the first layer of the top material — whilst clearly separate from the substrate — has a different hue to it compared to the bulk of the later top material. This implies that the first one, two or three layers experience a gradient in being a mixture of the top and substrate materials before being full bulk top material.

The tortuous pattern between the two steels in Figure 11 is noteworthy, as similar phenomena are observed during the conduction of this thesis.

4.2 Nickel-based superalloy Inconel 718

Nickel-based superalloy Inconel 718 (IN718) is a high performance material used widely in fields such as aerocraft, energy and space industry. [1] IN718, due to it being a superalloy, has good properties for extreme environments where high strength, creep resistance and toughness is needed. [1]

According to Tucho et al.: "*IN718 is a face-centered cubic, austenite (γ) solid supersaturated solution matrix rich in Ni, Cr, and Fe, an intermetallic Laves phase (Ni, Fe, Cr)2(Nb, Mo and Ti), and precipitated phases of IN-718 alloy that mainly consist of the γ'' (Ni3Nb) phase, γ' (Ni3(Al, Ti)) phase, δ (Ni3Nb) phase, and MC carbides*" [36]

IN718 is known for its ability to maintain good mechanical properties up to 650 °C. It is used in aerospace, nuclear, chemical and petrochemical applications where its high strength, corrosion resistance and fatigue resistance are valued. Additional applications are: marine architecture, electronic components, pollution control equipment and pulp, paper or metal processing mills. [36]

IN718 possesses good weldability and is one of the most fabricated alloys in PBF-LB. [36]

Table 2 shows build parameters of IN718 manufactured via PBF-LB\M upon a substrate of 316L and their calculated volumetric energy densities.

Table 2. The list of parameters used to fabricate IN718 upon a 316L substrate.

AM Parameters					Ref.
P [W]	v [mm/s]	h [µm]	t [µm]	E_V [J/m^3]	
300	900	80	30	1.39E+11	[37]
300	900	80	30	1.39E+11	[16]
100	700	140	50	2.04E+10	[32]
95	800	50	20	1.19E+11	[38]
300	900	80	30	1.39E+11	[39]
300	900	80	30	1.39E+11	[40]
300	900	80	30	1.39E+11	[41]
100-300	300-2100	-	45	-	[42]
300	650	110	50	8.39E+10	[43]
285	960	110	40	6.75E+10	[44]
250-350	850-1050	90	40	-	[45]
100	200	140	30	1.19E+11	[46]
Average:				1.10E+11	

Note the different parameters given in Table 2. While there is variety in the parameters, the set of 300 W, 900 mm/s, 80 µm and 30 µm — for laser power, scanning speed, hatch spacing and layer thickness respectively — are the most often mentioned set.

Comparison between Table 2 and Table 1 shows that IN718 being built on top of 316L is studied seemingly more than 316L upon IN718. [1]

Table 1 and Table 2 are based on the review paper by ZainElabdeen et al. from which the references in said tables were acquired. The paper gives insight into the research landscape, as it is a review of the state-of-the-art in multimaterial PBF-LB\M. [1] The reason for the greater number of publications which study IN718 built on a 316L substrate could be due to increased feasibility and convenience of removal after manufacture. It is simpler to remove 316L from the building platform than it is to remove IN718. IN718 needing more time or more specialized equipment to remove than 316L due to, e.g. its greater hardness and its work hardening phenomenon. [30]

5 Heat treatment of IN718

This chapter explores the theory for the heat treatment method that was used in the experimental portion of this thesis. IN718 is a material that experiences notable improvements from heat treatment. The heat treatment plan for the workpieces used in this thesis was chosen to be as follows:

1. Solution annealing for 2 hours at 954 °C
2. Water quenching
3. Ageing treatment for 8 hours at 718 °C
4. Ageing treatment for 10 hours at 621 °C.

It was decided during the duration of conducting the thesis that solution annealing would be performed at 954 °C for two hours. The values of solution annealing and ageing treatments have similarity to ones provided in literature. [47] Quenching in water after solution annealing is also present in literature. [48]

The purpose of the solution annealing is to homogenize the alloy. The quenching is performed to rapidly cool the homogenized alloy, as slow cooling rates at or below 7 Kelvin per second would cause the formation of δ phases. [47] The formation of δ phases in the material is undesirable due to the δ phase facilitating cracking. [36] After the homogenization of the alloy during solution annealing, the ageing treatment is then employed to produce desirable γ′ and γ″ phases which enhance hardness. [49]

6 Aim and purpose of the experimental part

The aim and purpose of the experimental part of this thesis was to study the manufacturability of bimetallic 316L-IN718 using PBF-LB\M, as well as the properties of the materials as a bimetallic combination — both as-built and heat-treated.

The thesis was split into three phases:

1. The planning phase
2. The optimization phase
3. The experimental phase

The thesis workflow is illustrated in Figure 12.

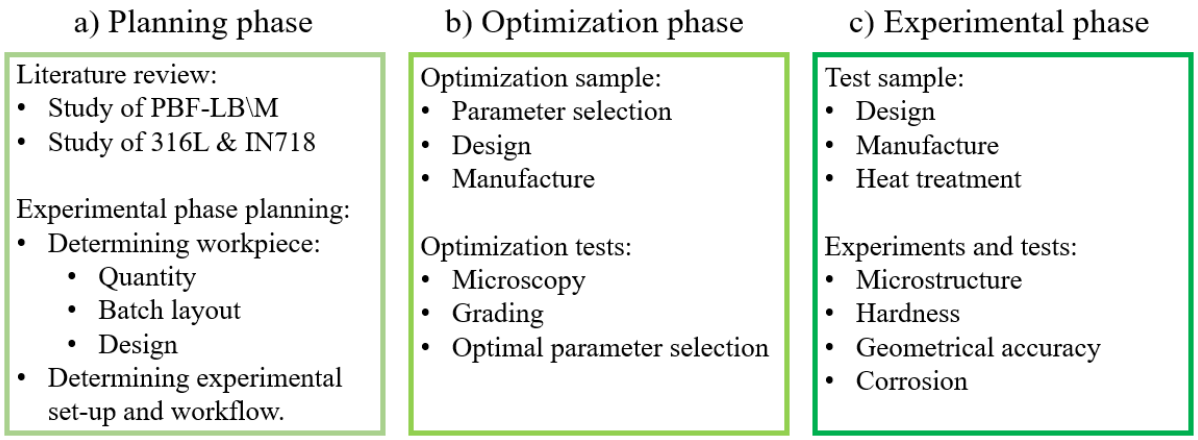

Figure 12. A diagram of the thesis workflow.

The planning phase mentioned in Figure 12 a) included:

- The review of the literature, the study of PBF-LB\M as a technology and the study of the 316L-IN718 materials from the point of view of PBF-LB\M and use as a bimetallic combination.
- The planning of experiments from the formulation of the workpiece quantity and layout for each batch of workpieces produced to the geometry and design of the workpieces.
- The determining of the hardware and software which would be used in the experiments as well as establishment of the experimental workflow.

The optimization phase mentioned in Figure 12 b) included:

- The selection of the parameters used in the PBF-LB\M process to manufacture the 316L and the IN718 portions of each workpiece.
- The adjustments of the design of the workpieces.
- The manufacture of the workpieces to determine optimal parameters for the IN718 built on top of the 316L. Optimal parameters being defined as that set of parameters used in manufacture of IN718 on top of 316L which resulted in the least porosity and best interface for the IN718 out of all the parameters used.
- The microscopy of the workpieces as well as the evaluation and grading of the quality of IN718 parameters, resulting in the selection of the best parameter set out of each parameter set tested.

The experimental phase mentioned in Figure 12 c) included:

- Adjustments to the workpiece design for the experimental phase as well as the manufacture of the workpieces for experiments and tests. Adjustments including the increase of the height of the 316L portion to allow for a margin which was used in removal from the building platform.
- The heat treatment of the workpieces using the IN718 heat treatment plan.
- The preparation of the workpieces for their respective tests and measurements. As well as the conduction of said tests and measurements for workpieces both as-built and heat-treated, including:
    - The porosity and microstructure measurements with polished workpieces and a microscope, as well as digital data-analysis and statistical analysis to determine the porosity and the confidence interval of the porosity.
    - The hardness measurements using the hardness tester, as well as the digital data-analysis and statistical analysis to determine the hardness and the confidence interval of the hardness.

- The geometrical accuracy measurements utilizing the 3D surface analysis microscope as well as the digital data-analysis to determine the deviation of the manufactured workpieces from the digital workpiece design.
- The corrosion measurements utilizing the potentiostat as well as the digital data-analysis to determine the corrosion rate after an open circuit potential measurement.

This thesis also compares the experimental results, measurements and behavior and with the theoretical understanding and literature.

7 Experimental set-up

This chapter will describe the experimental set-up which refers to the arrangement and configuration of equipment, materials, and procedures used to conduct the experiments.

7.1 Powder materials

This chapter describes the powders that were used to manufacture the AMed bimetallic 316L-IN718 workpieces used in the experiments.

7.1.1 The stainless steel 316L powder

The powder that was used to AM the workpieces was similar as described in standard 316L ASTM A276 / DIN EN 10088 / 1.4404, produced by SLM Solutions. Table 3 illustrates the chemical composition for 316L ASTM A276 / DIN EN 10088 / 1.4404.

Table 3. The powder composition of the used 316L ASTM A276 / DIN EN 10088 / 1.4404 [50]

ASTM A276										
	Fe	Cr	Ni	Mo	Mn	Si	P	C	S	N
Min.	Bal.	16.00	10.00	2.00						
Max.		18.00	14.00	3.00	2.00	1.00	0.045	0.030	0.030	-
DIN EN 10088										
	Fe	Cr	Ni	Mo	Mn	Si	P	C	S	N
Min.	Bal.	16.50	10.0	2.00						
Max.		18.50	13.0	2.50	2.00	1.00	0.045	0.030	0.030	0.10

As Table 3 shows, iron has the highest prevalence in the 316L alloy, with a minimum amount of 61.895 and a maximum of 72.00 in ASTM A276. In DIN EN 10088 the minimum amount being 62.895 and the maximum being 71.50.

The averages of the ASTM A276 / DIN EN 10088 / 1.4404 values from the Table 3 are detailed in Figure 13.

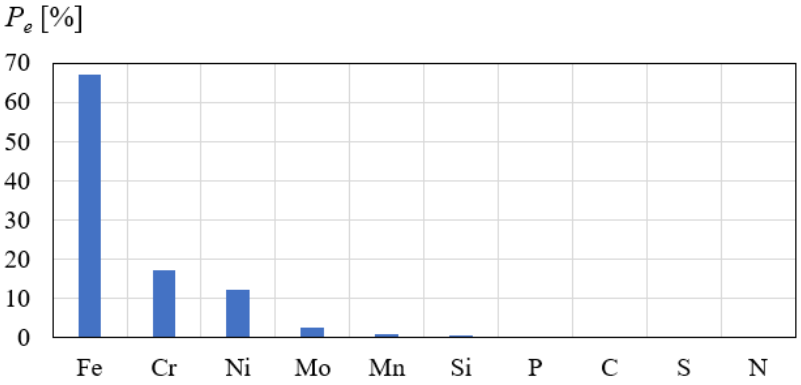

Figure 13. The mean average of the minimum and maximum value in the alloy 316L based on ASTM A276 / DIN EN 10088 / 1.4404 [50]

As Table 3 and Figure 13 show, 316L ASTM A276 / DIN EN 10088 / 1.4404 is an iron-based alloy, with notable prevalences (P_e [%]) for chromium, nickel, molybdenum and manganese.

Table 4 shows the powder properties for 316L ASTM A276 / DIN EN 10088 / 1.4404.

Table 4. The powder properties of 316L ASTM A276 / DIN EN 10088 / 1.4404 [50]

Particle size	10 – 45 µm
Mass density	≈ 7.9 g/cm^3
Particle shape	Spherical

7.1.2 The nickel-based superalloy Inconel 718 powder

The powder that was used to AM the workpieces was similar as described in standard IN718 ASTM F3055 / ASTM B637 / AMS5664, produced by SLM Solutions. Table 3 illustrates the chemical composition for IN718 ASTM F3055 / ASTM B637 / AMS5664.

Table 5. The powder composition of the used IN718 ASTM F3055 / ASTM B637 / AMS5664 [51]

IN718 ASTM F3055 / ASTM B637 / AMS5664															
	Fe	Ni	Cr	Ta+Nb	Mo	Ti	Co	Al	Si	Mn	Cu	C	P	S	B
Min	Bal.	50	17	4.75	2.8	0.65		0.2							
Max		55	21	5.5	3.3	1.15	1	0.8	0.35	0.35	0.3	0.08	0.015	0.015	0.006

As Table 5 shows, nickel has the highest prevalence in the IN718 alloy. The prevalence of iron in IN718 ASTM F3055 is 24.6 at maximum and 11.134 at minimum. The averages of the IN718 ASTM F3055 / ASTM B637 / AMS5664 values from the Table 5 are detailed in Figure 14.

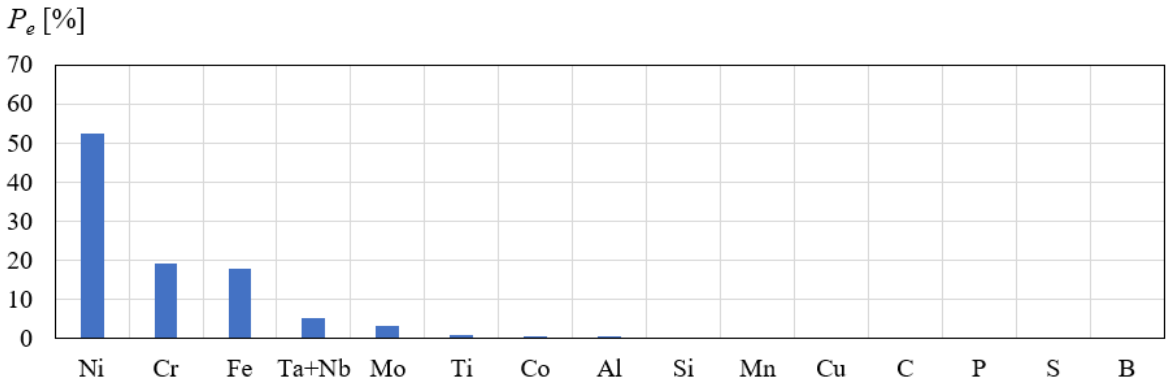

Figure 14. The mean average of the minimum and maximum value in the alloy IN718 based on ASTM F3055 / ASTM B637 / AMS5664. [51]

As Table 5 and Figure 14 show, IN718 ASTM F3055 / ASTM B637 / AMS5664 is a nickel-based alloy, with notable prevalences (P_e [%]) for chromium, iron, molybdenum, tantalum and niobium.

Table 6 gives the powder properties for IN718 ASTM F3055 / ASTM B637 / AMS5664.

Table 6. The powder properties of IN718 ASTM F3055 / ASTM B637 / AMS5664 [51]

Particle size	10 – 45 µm
Mass density	≈ 8.2 g/cm^3
Particle shape	Spherical

7.2 Additive manufacturing, machining and heat treatment hardware

This chapter goes over the hardware used in the conduction of the thesis. Including the PBF-LB\M machine, the furnace used for heat treatment, the saw with which workpieces were cut and the polishing machine with which the workpieces were ground and polished.

The hardware that was used is listed in Table 7.

Table 7. All hardware used for AM, machining and heat treatment during the conduction of the thesis.

Machine	Manufacturer	Name
PBF-LB\M machine	Aconity3D	Aconity MIDI+
Heat treatment furnace	Nabertherm	N7
Metal belt saw	Optimum	Opti S 290G
Polishing machine	Struers	Laboforce-100

Aconity MIDI+ is an open source PBF-LB\M machine. [52], [53] Aconity MIDI+ specifications as reported by Piiroinen [52] are:

- Build space: diameter 250 mm, height 250 mm.
- Laser configuration: IPG photonics CW, fiber laser, l = 1070nm, max power: 400 W
- Optics configuration: F-Theta, 3D scanning
- Spot size: 80 – 500 µm
- Layer thickness minimum: 10 µm
- Scan speed maximum: 12 m/s

The Nabertherm N7 furnace used for heat treatment in this thesis had a maximum temperature of 1100 °C according to the machine plaque. It was observed to have a heating rate of approximately 400 – 450 °C per hour. The furnace was always operated by setting it to heat up to a desired temperature from room temperature.

The Optimum Opti S 290 G metal belt saw was used to cut workpieces out of the building platforms as well as to cut the corrosion samples from the workpieces. The machine was operated manually and by utilizing the slower cutting speeds and a cutting fluid.

The Struers Laboforce-100 was utilized with specimen holder, single specimen holder and manually during the conduction of this thesis. Variable rotations of the specimen holder and the grinding platform were used. SiC papers ranging from grits of 120 – 4000 were used. Diamond suspension fluid of 9, 3 and 1 µm were used. The specific fineness of SiC paper or diamond suspension fluid used in a given experiment or measurement preparation is given during the description of that experiment or measurement.

7.3 Measuring instruments

This chapter goes over the measuring instruments used in the conduction of the thesis. Including the microscope, hardness tester, 3D surface analysis microscope and the potentiostat. The used instruments are given in Table 8.

Table 8. All measuring instruments used during the conduction of the thesis.

Instrument	Manufacturer	Name
Microscope	Motic	AE2000MET
Hardness tester	Innovatest	Falcon 600
3D surface analysis microscope	Alicona	InfiniteFocus G6
Potentiostat	Ivium	Vertex

The Motic AE2000MET objective specifications are given in Table 9. [54]

Table 9. Motic AE2000MET objective specifications. [54]

Objective	Numerical aperture	Working distance [mm]
LM Plan BD 5X	0.13	17.3
LM Plan BD 10X	0.25	16.3
LM Plan BD 20X	0.4	7.3
LM Plan BD 50X	0.55	7.2
LM Plan BD 100X	0.8	1.7
LM Plan 5X	0.13	20.3
LM Plan 10X	0.25	17.5
LM Plan 20X	0.4	8.1
LM Plan 50X	0.55	8.4
LM Plan 100X	0.8	2

As Table 9 shows, the magnifications available range from 5X to 100X. Specific magnification used in a given experiment or measurement preparation is given during the description of that experiment or measurement.

The Innovatest Falcon 600 was the hardness tester used to conduct the thesis. It was used to conduct single point HV10 measurements with the dwell time of 10 seconds.

The Alicona Infinitefocus G6 was the optical surface roughness measuring device or 3D surface analysis microscope used to measure the geometrical accuracy of the workpieces in this thesis. The objective specific features are given in Table 10.

Table 10. The Alicona Infinitefocus G6 objective specifications. [55]

Objective name	1900 WD30	800 WD37	800 WD17	400 WD30	400 WD19	150 WD11	80 WD4
Working distance [mm]	30	37	17.5	30	19	11	4.5
Lateral measurement range (X, Y) [mm]	3.8	1.6	1.6	0.8	0.8	0.3	0.16
Measurement point distance [µm]	1.77	0.72	0.72	0.36	0.36	0.14	0.07
Measurement noise [nm]	80	40	15	20	5	2	1
Vertical resolution [nm]	250	130	50	80	30	15	10

The Ivium Vertex potentiostat was used with a Ag/AgCl reference electrode and a Graphite auxiliary electrode. Measurements were performed in a 3.5 % by weight NaCl solution.

7.4 Design Software

This chapter discloses the design software used in the conduction of the thesis. Including the software used to design the workpieces, the layout of the building platform, and with which the PBF-LB\M machine was controlled. The used software is given in Table 11.

Table 11. All software used during the conduction of the thesis.

Software used for	Producer	Name
design of workpiece geometry	PTC	Creo 9.0.1.0
design of building platform layout	Autodesk	Netfabb 2025
control of the PBF-LB\M machine	Aconity3D	AconitySTUDIO

As can be seen from Table 11, PTC Greo 9.0.1.0 was the software used to design the workpiece geometry. Workpiece geometry including the height of the 316L and the IN718 portions, the length of the sides of the workpieces as well as the rounding radii of the vertical edges. Autodesk Netfabb 2025 was used to design the building platform layout. The building platform layout being the pattern and orientation in which the workpieces would be built on top of the building platform. Aconity3D AconitySTUDIO was used to control the PBF-LB\M machine, it was used to select parameters and control the PBF-LB\M process.

8 Experimental procedure (part A: PBF-LB\M of the 316L-IN718 workpieces)

To manufacture workpieces for study, first a plan for their layout on the building platform was formed. The layout of the building platform determines where each workpiece is located on the building platform. Then the digital 3D model of workpieces themselves were made using Creo 9.0.1.0. Afterwards the workpiece geometries were ported to Autodesk Netfabb 2025 to have the digital 3D models of the workpieces be allocated on the digital model of the building platform. The workpieces and their dimensions are illustrated in Figure 15.

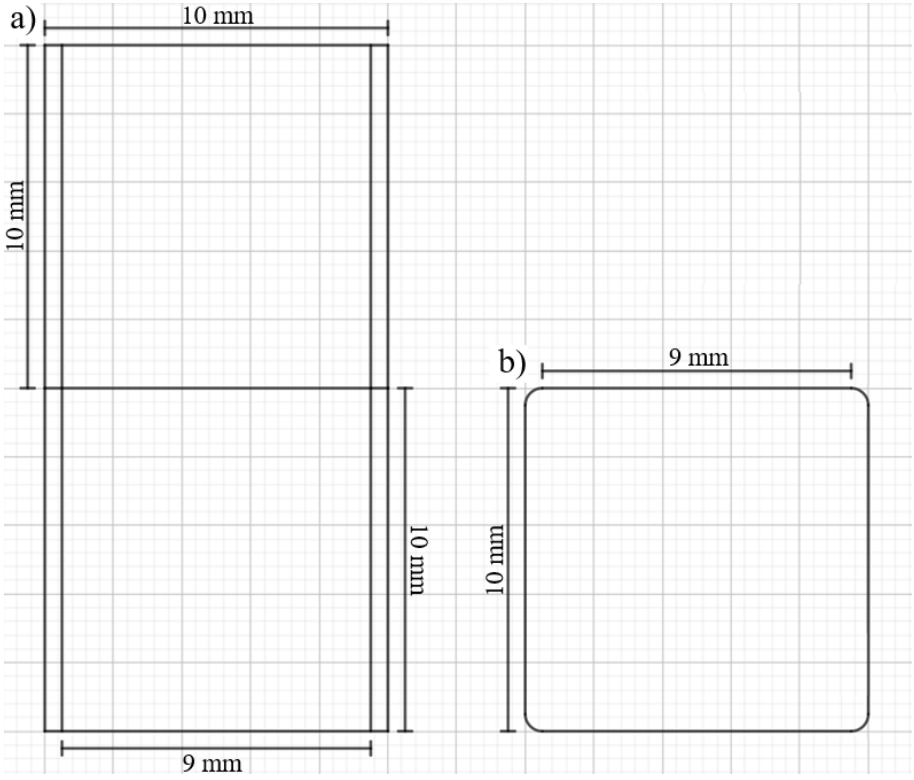

Figure 15. An illustration of the workpiece geometries.
a) shows the horizontal view of the workpiece geometry.
b) shows the vertical view of the workpiece geometry.

Figure 15 shows the geometry of the workpiece. In Figure 15 a) one can see the design of the workpiece geometry from a horizontal point of view, and in Figure 15 b) from the vertical point of view. The rounding radius is 0.5 mm for the vertical edges. 316L is manufactured first to act as a substrate for the IN718.

The design of the workpiece was determined to be two cubes built on top of each other. The vertical edges were set to have a rounding radius of 0.5 mm. This was done due to the fact that sharp vertical edges, which require a build plan with sharp corners, could cause issues during the PBF-LB\M process as sharp corners would experience increased thermal stresses.

Markings and identification text for the workpieces would be manufactured as 0.3 mm protrusions from one of the vertical sides.

To determine the effects of the IN718 heat treatment plan on the bimetallic combination of 316L-IN718, it was decided that each test, measurement or experiment should have an as-built and a heat-treated workpiece. Taking this into consideration, it was calculated that the number of workpieces that could be built on the same building platform was 12. The calculation was performed with Equation 2.

$$n_{wp} = \frac{d_{\mathrm{BP}} - 2m_{\mathrm{DP}}}{\sqrt{2}(l_{\mathrm{wp}}) + m_{\mathrm{S}}} \tag{2}$$

Where n_{wp} is the number of workpieces, d_{BP} is the diameter of the building platform, m_{BP} is the outer margin of the building platform, l_{wp} is the length of the side of a workpiece and m_{S} is the margin between the workpieces.

This was concluded after:

- taking into account the margin around the edge of the building platform and
- ensuring that no workpiece overlap more than 1 mm with other workpieces on the recoating blade width.

The number of workpieces were determined with Equation 2 using: d_{BP} = 250 mm, m_{BP} = 20 mm, l_{wp} = 10 mm and m_{s} = 3 mm.

$$n_{wp} = \frac{d_{\mathrm{BP}} - 2m_{\mathrm{DP}}}{\sqrt{2}(l_{\mathrm{wp}}) + m_{\mathrm{S}}} = \frac{250\ \mathrm{mm} - 40\ \mathrm{mm}}{\sqrt{2}(10\ \mathrm{mm}) + 3\ \mathrm{mm}} \approx 12.25$$

As can be seen from the result, it was possible to allocate 12 workpieces while having a mean average margin between workpieces of at least 3 mm.

The geometry of manufactured workpieces can be seen in Figure 16.

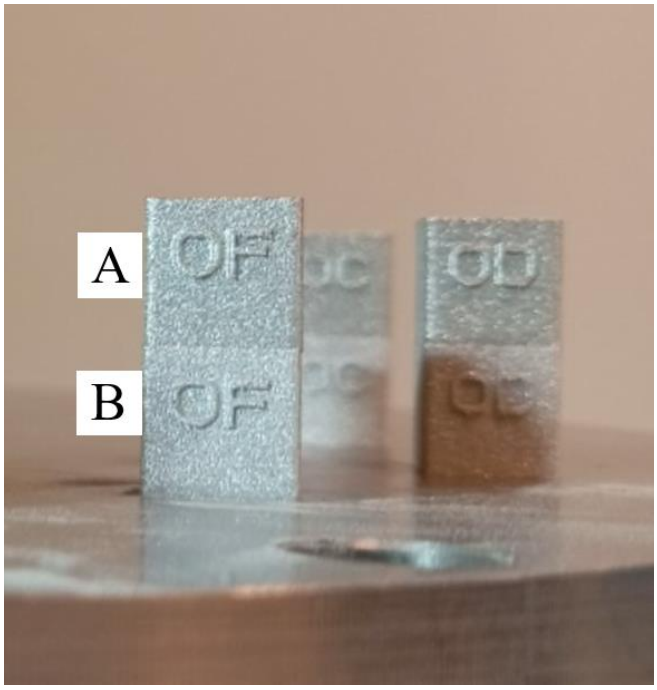

Figure 16. Workpieces built onto the building platform that have not yet been removed. The marking “OF”, “OD” and “OC” identified the workpieces, the markings are 0.3 mm protrusions from the side.
A) IN718 is built on top of the 316L substrate.
B) 316L is built on top of the building platform.

As Figure 16 shows, the cube located beneath the workpiece (A) was made of 316L, whereas the cube located above the workpiece (B) was made from IN718. This was decided because of the comparative ease of removal from the building platform is greater with 316L. The markings on the workpieces were made to allow for tracking of the workpieces. The first letter “O” in these workpieces designates their use as “optimization” workpieces, ergo: the workpieces were meant to be used in the determination of the best parameters for IN718 built on a 316L substrate using PBF-LB\M. The second letters ranged from “A” to “L” in alphabetical order, and they were used to distinguish workpieces from each other within the same batch. As a note: the first letter was changed from “O” to “T” after the optimization phase had ended, the “T” standing for “test” as the workpieces would be used in the experimental phase for testing and measurements.

In Netfabb, the layout was set so that no workpiece would be behind another from the direction of the recoating blade. The workpieces were each set to face the recoating blade in a 45° angle to ensure that each workpiece would not present a flat surface to the recoating blade. This was done to make the movement of the recoating blade as smooth as possible,

minimizing the risk of an upward bump when the coater blade moved over a workpiece. The workpiece layout is illustrated in Fig. 12.

Before the placements of the workpieces, it was decided to have the workpieces be placed in such a manner as to fulfil the following criteria.

The workpieces were to be placed so that they:

- would not be under the laser scanner that was above the left side of the building platform.
- were no closer than 7 mm from each other.
- were so that no workpiece was directly behind another from the blade direction for no more than at most 1 mm of the blade width.

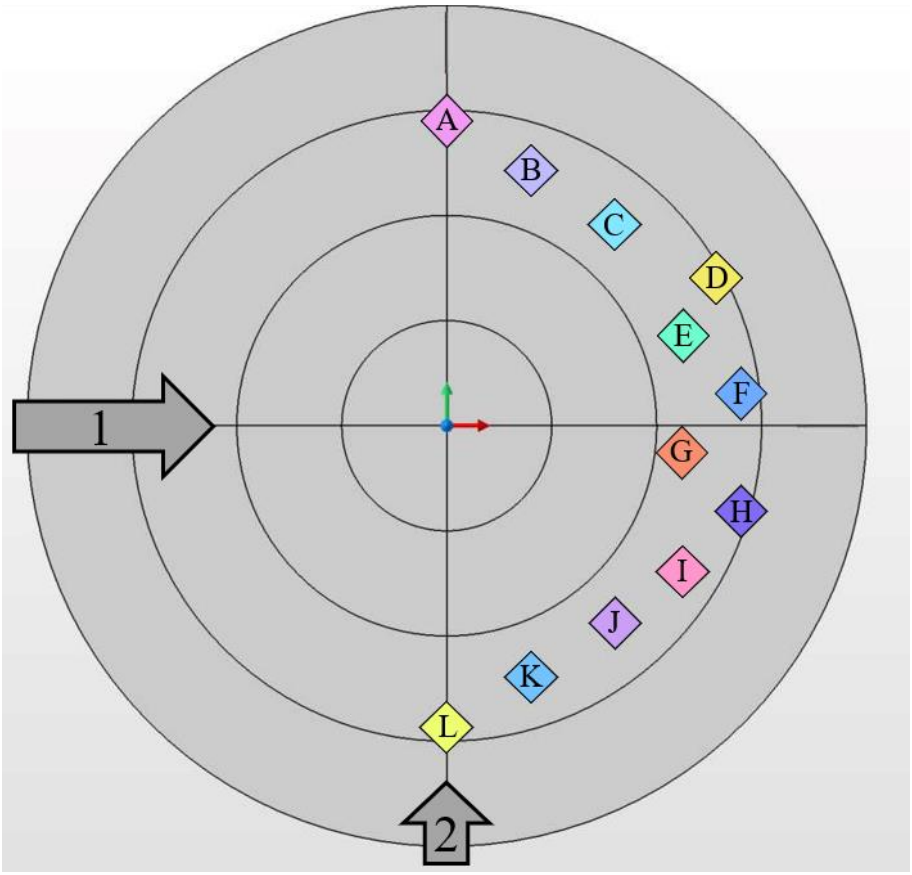

Figure 17. The placement of the workpieces on the building platform illustrated.
1) Shows the direction and starting point of the recoating blade.
2) Shows the direction from which Argon is supplied.
A-L) Show the allocation of different workpieces on the building platform.

As Figure 17 the digital models of the workpieces to be manufactured are positioned along a rough arc near to the right of the building platform, due to the aforementioned criterion of the workpieces not being under the laser scanner.

The positions for the digital models on the building platform were input to Netfabb as X and Y coordinates, representing mm on the building platform. The digital models would be centered on these coordinates.

The coordinate values for the placement of the workpieces on the building platform are given in Table 12. These values determine the point at which the underside of the digital 3D model of the sample would be centered. Note that the three decimal values are used due to this being the input given to Netfabb and as such AconitySTUDIO.

Table 12. The coordinates for the placement of the workpieces on the building platform as well as the coordinates of the building platform center for reference. The decimal accuracy is set to the given amount for sake of repeatability, as those values were given to the PBF-LB\M machine.

Position of Workpiece	X [mm]	Y [mm]
Building platform center	125	125
Workpiece A	125	215.875
Workpiece B	150	200.875
Workpiece C	175	184.875
Workpiece D	205	169.375
Workpiece E	195	151.875
Workpiece F	212.5	134.375
Workpiece G	195	116.875
Workpiece H	212.5	99.375
Workpiece I	195	81.875
Workpiece J	175	66.375
Workpiece K	150	50.375
Workpiece L	125	35.375

Table 12 gives the coordinates for the workpiece placements, which follow the arch-like pattern as noted in Figure 17. The origo in Figure 17 is in the coordinates of the building platform center given in Table 12.

Once the Netfabb file was ready, the file was used to control the Aconity MIDI+ machine itself using AconitySTUDIO.

8.1 Optimization workpieces

The optimization workpieces were manufactured with the dimensions of 10 mm by 10 mm, with 10 mm tall lower and upper sections. The manufacturing parameters for the lower portions made of 316L are given in Table 13. These values were decided during conducting the thesis, and were based on the values suggested by the Aconity MIDI+ operator.

Table 13. The manufacturing parameters for the 316L optimization workpieces. 316L used the same parameters for every workpiece ID.

Sample ID	P [W]	v [mm/s]	t [µm]	h [µm]	E_V [J/m^3]
OA-OL	150	900	30	80	6.94E+10

Similar suggested values for IN718 are given in Table 14.

Table 14. The suggested parameters for the IN718

P [W]	v [mm/s]	t [µm]	h [µm]	E_V [J/m^3]
150	800	30	80	7.81E+10

The values shown in Figure 14 were decided upon during the conduction of this thesis after consulting advisors concerning the IN718 parameter selection.

To study the bimetallic manufacturability of IN718 on AMed 316L, the parameters used to manufacture each IN718 portion of the different workpieces were made variable, as seen in Table 15.

It was decided that, to make testing simpler, the only two parameters to be varied were the laser power P and the scanning speed v. It was decided that the scanning speed would be varied by 100 mm/s to each side of the suggested value of 800 mm/s, so the tested speeds would be 700, 800 and 900 mm/s. Then for laser power, it was decided that the power would be varied from 150 W with a range from -10 W to +20 W. So, the tested laser powers would be 140, 150, 160 and 170 W. It was decided that 10 W would be a large enough step to not be redundant, but also a small enough step to capture finer resolution within the parameter space. The parameter combination of laser power P and scanning speed v are given in Table 15.

Table 15. The manufacturing parameters for the IN718 optimization workpieces.

Sample ID	P [W]	v [mm/s]	t [µm]	h [µm]	EV [J/m3]
OA	140	700	30	80	8.33E+10
OB	150	700	30	80	8.93E+10
OC	160	700	30	80	9.52E+10
OD	170	700	30	80	1.01E+11
OE	140	800	30	80	7.29E+10
OF	150	800	30	80	7.81E+10
OG	160	800	30	80	8.33E+10
OH	170	800	30	80	8.85E+10
OI	140	900	30	80	6.48E+10
OJ	150	900	30	80	6.94E+10
OK	160	900	30	80	7.41E+10
OL	170	900	30	80	7.87E+10

After the workpieces were manufactured, they were removed from the building platform, and they then were ground and polished.

After grinding and polishing the workpieces were micrographed with a microscope.

From these microscopy images the workpieces were graded based on the quality of the IN718. Main focus was on determining which workpiece — and as such, which parameters — had the best interface and the least porosity of the IN718 present. The selection was performed with a process of elimination. Eliminations were done with two rounds, first was an elimination of nine of all the twelve workpieces. After the first round the three selected workpieces would undergo further polishing, after which these three workpieces would also undergo a selection via elimination. This way it was determined which parameters out of the options available were the best for IN718. This method was chosen due to the time constraints of the project.

The parameters that would be selected would be used in the manufacture of the IN718 for the test workpieces.

The microscope images were graded with a quality rating with grades from 1 to 5, where 1 is unacceptable, 2 is impermissible, 3 is permissible, 4 is acceptable and 5 is pristine. The main grading criteria were:

- a lack of porosity in IN718
- smoothness of texture of IN718
- the quality of interface between 316L and IN718

The polishing of the workpieces was done on the first round with a procedure of grinding with diamond sheets with the grits of 200, 600 and 1200, then with diamond fluid of 9 μm and 3 μm.

Each step was performed for a minimum of 2 minutes, however during the execution of this preparation phase, the exact times varied as it was done until it resulted in an even surface. This meant that sometimes a setting was used for quite a lot longer than 2 minutes.

The polishing of the workpieces was done on the second round with a procedure of grinding with SiC paper with the grit of 4000 then with diamond fluid of 1 μm.

8.2 Test workpieces

The parameters used to manufacture the IN718 portion of the test workpieces were decided to be P = 170 W and v =700 m/s.

Note that over the course of manufacturing the test workpieces, it was observed that the 316L of the first batch of workpieces meant for testing was excessively porous. This porosity was thought to having been possibly caused by a leak in the argon supply of the PBF-LB\M machine that was detected after the manufacture of the test workpieces. In addition to this, it was considered that it could have been due to the use of recycled powder. It was calculated that the argon leak — which was repaired after being detected — may not have been solely responsible for the unexpected porosity.

Due to the poor quality of the first batch of workpieces meant for testing, it was decided to manufacture of a second batch. It was decided that the volumetric energy density for the building parameters of the 316L in the second batch of workpieces meant for testing would be increased by approximately 15%. This decision was made after consulting the PBF-LB\M

machine operator and an advisor, as the increased volumetric energy density would lower the porosity of the 316L assuming that the porosity originated due to the powder being recycled. The volumetric energy density increase was achieved by setting the laser power to 160 W and lowering the scanning speed to 835 mm/s. This is illustrated in Table 16.

Table 16. The main manufacturing parameters for the 316L test workpieces for the first test workpiece batch and the second. 316L did not use different parameters for different Samples ID.

Sample ID	P [W]	v [mm/s]	t [µm]	h [µm]	E_V [J/m^3]
First batch of workpieces meant for testing					
TA-TL	150	900	30	80	6.94E+10
Second batch of workpieces meant for testing					
TA-TL	160	835	30	80	7.98E+10

The second batch of test workpieces was made, and the 316L in them had been observed to be of a lesser porosity compared to the first batch, and as such it was elected that the second batch of test workpieces would be used in the experiments and measurements. The workpieces still contained some porosity in them, but in the interest of the schedule, they were admitted for tests and measurements.

As such, **the parameters used to manufacture each 316L-IN718 workpiece that were used in testing** are given in Table 17.

Table 17. The manufacturing parameters of 316L and IN718 for workpieces that were used in testing.

Material	P [W]	v [mm/s]	t [µm]	h [µm]	E_V [J/m^3]
316L	160	835	30	80	7.98E+10
IN718	170	700	30	80	1.01E+11

The design of the workpieces was also modified for the workpieces that were to be used in testing. Figure 18 shows the design.

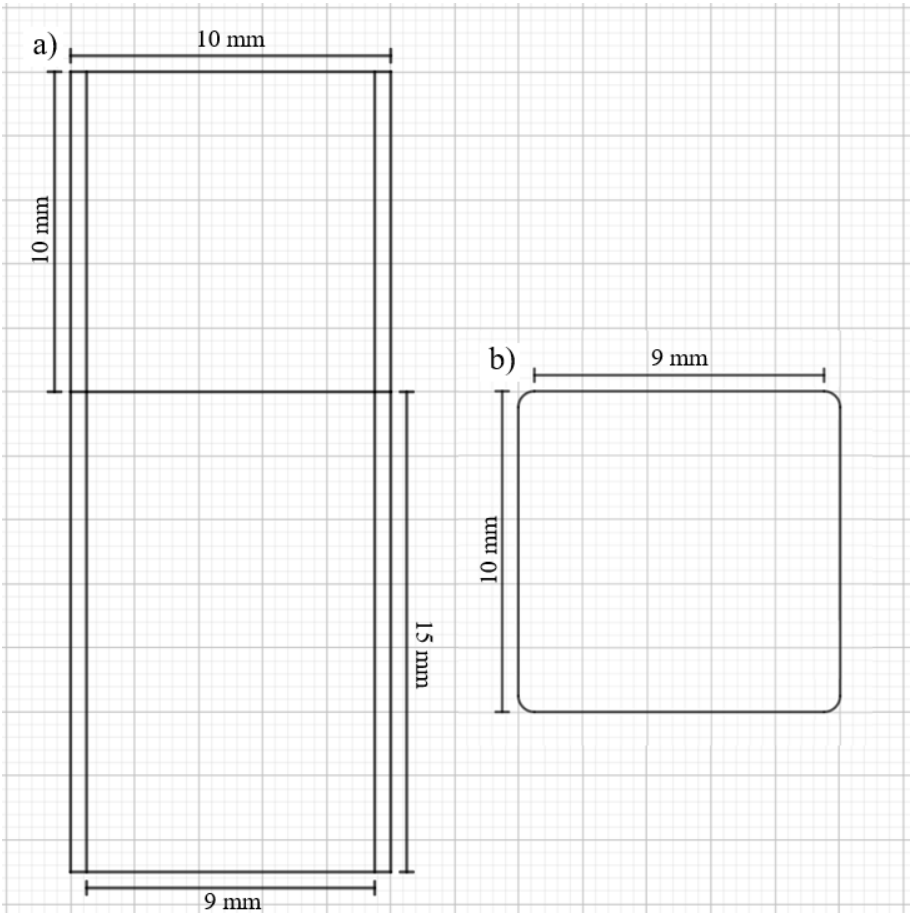

Figure 18. An illustration of the test workpiece geometries.
a) shows the horizontal view of the workpiece geometry.
b) shows the vertical view of the workpiece geometry.

Figure 18 shows the geometry of the workpiece. In Figure 18 a) one can see the design of the workpiece geometry from a horizontal point of view, and in Figure 18 b) from the vertical point of view. The rounding radius is 0.5 mm for the vertical edges. 316L has the height of 15 mm, and is manufactured first to act as a substrate for the IN718 which has the height of 10 mm.

The design was altered for the workpieces that were to be used in testing to allow for a margin of removal, since the workpieces would be cut from the building platform, and the additional 5 mm enabled the detached workpieces to have at least 10 mm of 316L.

The placements of the tests workpieces on the building platform were similar to the ones provided in Table 12, however, it is of note that two of the workpieces were made to be cylindrical, which would have been used in dilatometry tests. These dilatometry tests were set to be out-of-scope of this thesis due to the fact that the machine meant to be used in the dilatometry measurements was unfortunately rendered out-of-order.

The test batch workpiece layout on the building platform is given in Figure 19.

The dilatometry workpieces were cylindrical, with the lower 316L portion being made with a diameter of 7 mm and the upper IN718 portion with a diameter of 6 mm. This was selected at the time so to allow the workpieces to be machined to a diameter of 3 mm. They also had their IN718 portion have the height of 11 mm, which would have allowed for fine machining of the length of IN718 to be exactly the wanted 10 mm.

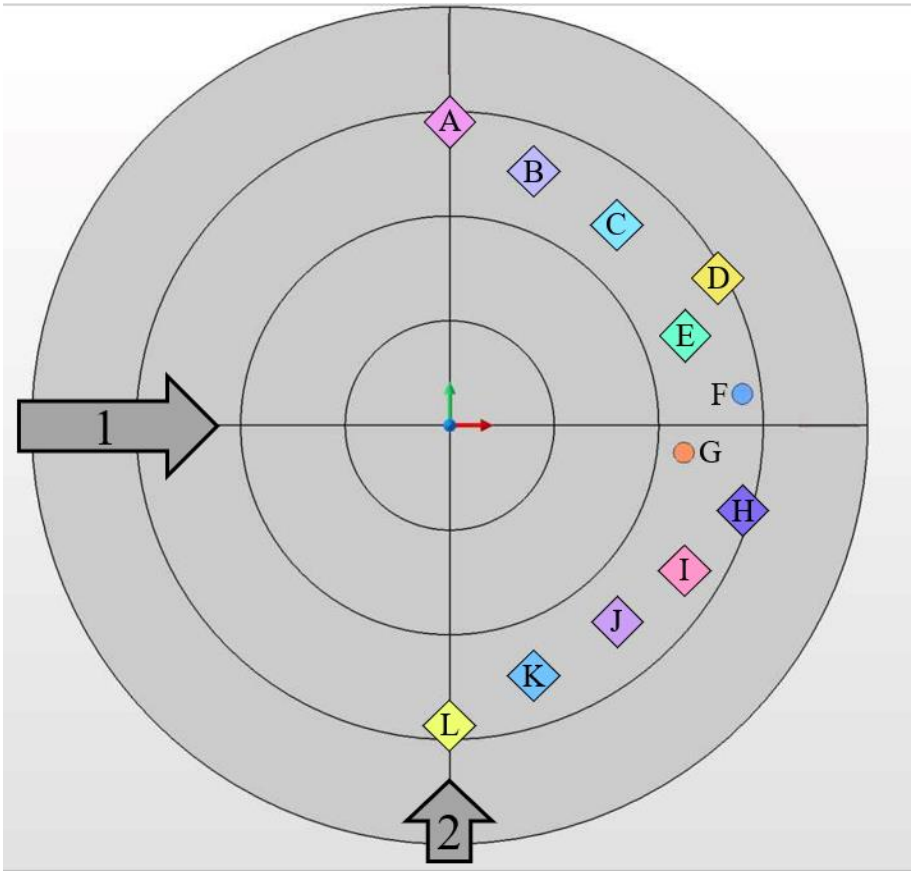

Figure 19. The placement of the workpieces on the building platform illustrated.
1) Shows the direction and starting point of the recoating blade.
2) Shows the direction from which Argon is supplied.
A-L) Show the allocation of different workpieces on the building platform.
F-G) Show the placement of the two workpieces meant to be used in the dilatometry tests.

8.3 Heat treatment

Half of the workpieces were selected to be heat-treated. The workpieces selected for heat treatment were manufactured in the positions of B, D, F, H, J and L as seen in Table 12.

The heat treatment used for the 316L-IN718 workpieces was as such:

1. Solution annealing for 2 hours at 954 °C
2. Water Quenching
3. Ageing treatment for 8 hours at 718 °C
4. Ageing treatment for 10 hours at 621 °C.

The solution annealing was performed by placing the workpieces in the furnace once it had reached the target temperature of 954 °C. Then after the target time of two hours had been reached the workpieces were removed one at a time from the furnace and quenched in water. The furnace was let to cool and once the furnace had cooled, the next step was begun. The workpieces were placed in the furnace, then the furnace was heated to the target temperature of 718 °C. The furnace had an approximate temperature increase of 400 – 450 °C per hour. Once the furnace had reached the target temperature it was maintained for the aforementioned 8 hours, after which the workpieces were removed and let to cool in the ambient air. Then once the furnace had cooled to room temperature again, the workpieces were placed in and the furnace was set to heat to the target temperature of 621 °C and said temperature was maintained for 10 hours, after which the workpieces were removed and let to cool in the ambient air.

9 Experimental procedure (part B: the tests for the 316L-IN718 workpieces)

This chapter details how the experiments were carried out in the laboratory with the aforementioned equipment.

This chapter will utilize the following Equation 3 and Equation 4 for determining standard deviation and confidence interval respectively:

$$\sigma = \sqrt{\frac{\sum(x-\bar{x})^2}{X}} \tag{3}$$

$$\mathrm{CI} = \bar{x} \pm z \frac{s}{\sqrt{n}} \rightarrow \mathrm{CI}_{95\%} \approx \bar{x} \pm 1.96 \frac{\sigma}{\sqrt{X}} \tag{4}$$

where σ is the population standard deviation, x is the sample value, $\bar{x}$ is the sample population mean, X is the sample population size, CI is the confidence interval, $\mathrm{CI}_{95\%}$ is the 95% confidence interval, z is the confidence level value (which is assumed to be 1.96).

9.1 Porosity and microstructure

The porosity of the workpieces was determined by using the microscope to take micrographs of the workpieces “TE” (as-built) and “TH” (heat-treated). The microscope was set to use the lens of ten times magnification. Note that the camera with which these micrographs were taken had a lens of 0.5 magnification.

The workpieces were set to epoxy, after which they were polished using the polishing machine. The polishing protocol used was SiC papers with grits of: 120, 220, 500, 800, 1200, 2000, 4000 and then 3 µm diamond fluid.

The force applied was 15 N per workpiece, and the rotation speed of the workpiece holder and the polishing surface were varied. Polishing times for each phase were a minimum of 2 minutes, with additional time spent on a given phase until an event surface was achieved.

The workpieces were then etched using a 10% by weight solution of Oxalic Acid ($H_2C_2O_4$ or $(COOH)_2$) for 3 minutes.

The workpieces were then micrographed with the microscope. Fifteen micrographs were taken with the aforementioned magnification from both workpieces: five of the bulk 316L, five of the bulk IN718 and five so that the interface lay in the middle of the micrograph.

These micrographs were analysed using a Python program. The program utilizes an image threshold technique to determine the pixels of the image to be either “dark” or “light”. The purpose of this is to count how many pixels out of the sum total of the picture are from pores. By setting the threshold value properly one can have both the pixels corresponding to pores and the non-pore corresponding pixels counted.

Porosity is defined by Equation 5. [56]

$$\varphi = \frac{V_\mathrm{p}}{V_\mathrm{a}} \tag{5}$$

Where φ is porosity, V_p is the pore volume and V_a is the apparent volume.

However, due to the method employed in this thesis, porosity is determined with Equation 6.

$$\varphi = \frac{p_\mathrm{p}}{p_\mathrm{a}} \tag{6}$$

Where φ is porosity, p_p is the number of pore-representing pixels and p_a is the total amount of pixels.

The threshold value selected for the Python program was “0.50”. This selection was done due to it capturing the detail of the porosity whilst not capturing surface marks and remnants from grinding and polishing.

Equation 7 is used to determine the comparative level of porosity near the interface as opposed to the bulk materials.

$$\varphi_{\Delta\mathrm{BM}} = \varphi_{\mathrm{BM}} - \frac{\varphi_{316\mathrm{L}}+\varphi_{\mathrm{IN718}}}{2} \tag{7}$$

where $\varphi_{\Delta\mathrm{BM}}$ is the difference between the porosity measured from the bimetallic interface and the mean average of the porosities measured from the bulk 316L and bulk IN718, φ_{BM} is the porosity measured from the bimetallic interface, $\varphi_{316\mathrm{L}}$ is the porosity measured from the bulk 316L and φ_{IN718} is the porosity measured from the bulk IN718.

9.2 Geometrical accuracy

The workpieces “TA” (as-built) and “TB” (heat-treated) were selected to be the ones used in determining the geometrical accuracy of the bimetallic workpieces. The goal was to determine how closely the features of the bimetallic workpieces matched the ones dictated by the CAD file. Both workpieces were measured so that the front of the workpiece would face upwards, after which the workpiece would be scanned with the Alicona 3D surface analysis microscope. The microscope would form a point cloud of the workpiece’s front, which then could be analysed for surface measurement, as seen in Figure 20.

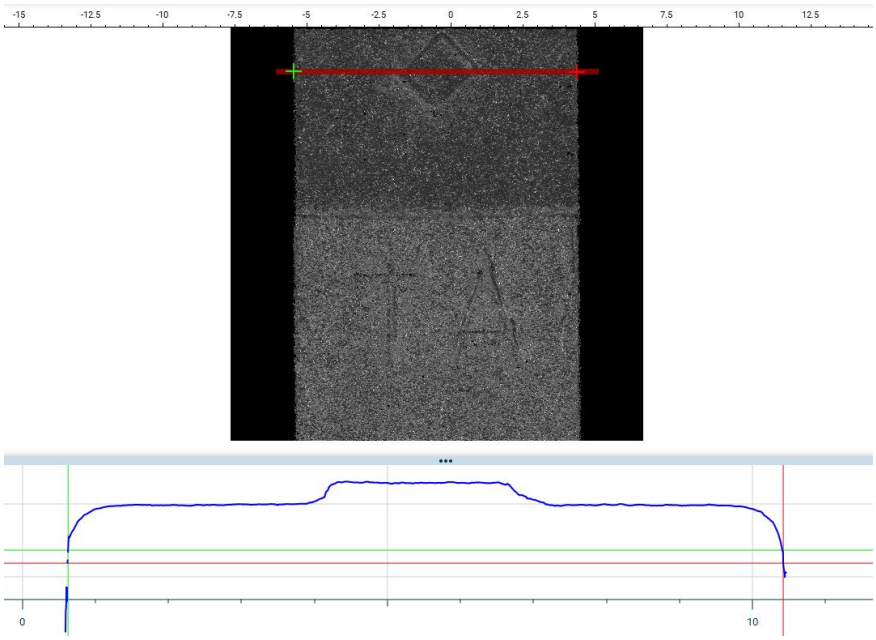

Figure 20. A screen print of the graphical user interface with which Alicona was operated.

In Figure 20 a line is drawn over of the diamond symbol by the machine operator to measure both the side-to-side width of the workpiece, the radii of the vertical edges as well as the offset of the diamond marking itself. The IN718 portion of the as-built workpiece is measured in the screen print.

With this method, the workpieces were measured for different geometric features from the point cloud. The workpieces were measured with seven lines, as seen in Figure 21.

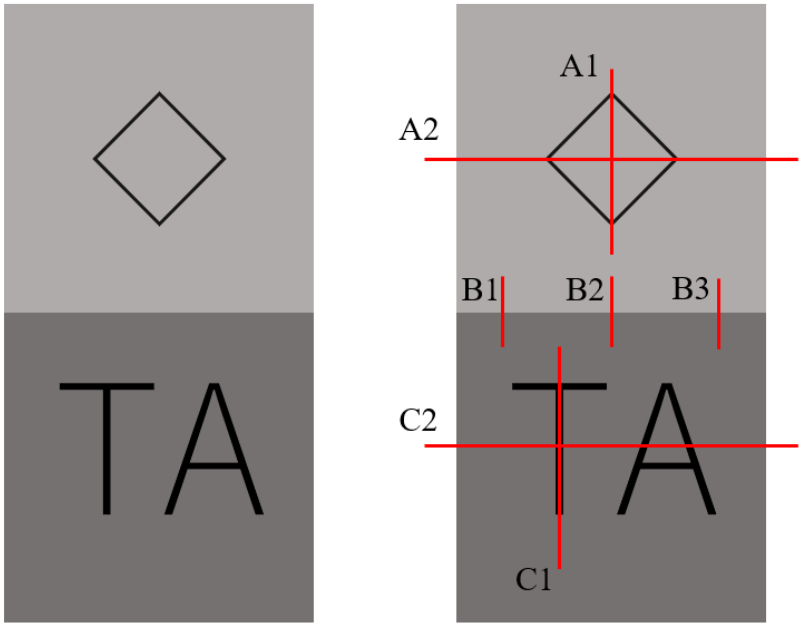

Figure 21. An illustration of the measurement lines over the point cloud.
A1) The vertical line over the IN718 diamond-shaped protrusion.
A2) The horizontal line over the IN718 diamond-shaped protrusion and from side-to-side.
B1–B3) Vertical lines over the interface.
C1) The vertical line over the 316L letter marking protrusion.
C2) The horizontal line over the 316L letter marking protrusions and from side-to-side.

Figure 21 illustrates the measurements that were to be done to determine the geometrical accuracy. A2 and C2 determined the geometric accuracy of the width and the rounding radii. A1, A2, C1 and C2 determined the geometric accuracy of the protrusions. B1, B2 and B3 determined offset between the different material portions.

The measurements as illustrated by Figure 20 and Figure 21 were then compared to the ideal measurements of the workpiece as illustrated by Figure 22.

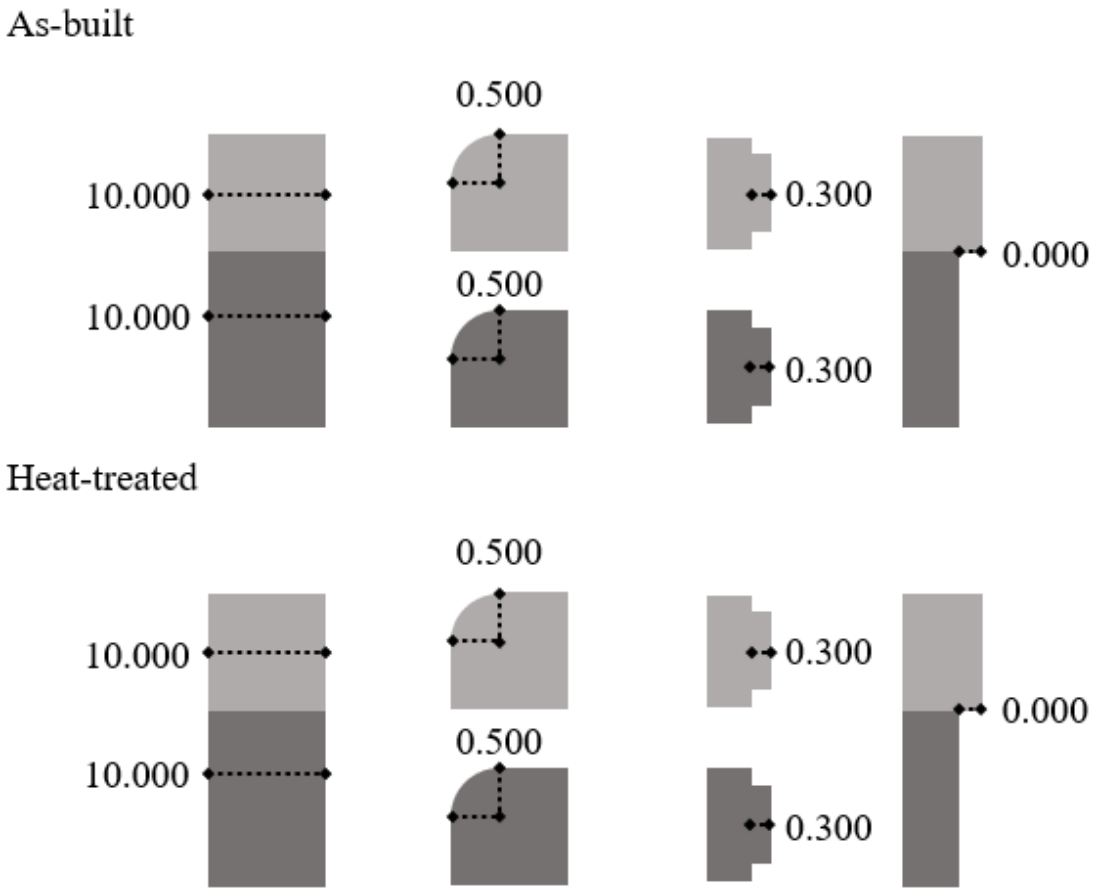

Figure 22. The ideal measurements of the workpieces based on the digital model dimensions given in millimeters.

As can be seen from Figure 22, the measurements for both 316L and IN718 would be:

- a side-to-side width of 10.000 mm.
- a rounding radius of 0.500 mm.
- a depth of the marking protrusion of 0.300 mm.
- an offset between the materials of 0.000 mm.

These measurements were compared with the values measured from the workpieces via the 3D surface analysis microscope to determine the geometrical accuracy.

9.3 Hardness measurements

The hardness measurements were conducted using a heat-treated workpiece and an as-built workpiece. The workpieces used were “TK” (as-built) and “TL” (heat-treated).

The workpieces were prepared by placing them into epoxy so that after grinding and polishing both materials would be exposed and polished. The workpieces were ground and polished using the grits of 120, 220, 500, 800, 1200, 2000 and 4000. Then the workpieces were placed on the hardness tester. The tests were conducted with Vickers hardness test: HV10 using the 10 times magnification lens of the hardness tester.

The protocol for the measurements was elected to be done with single point measurements which were repeated and the placement determined on a case-by-case basis for each measurement. This approach was chosen to avoid notable pores in the material, and to be sure that all measurements meant to measure the interface were actually centered on the interface.

The measurements for each bulk material, 316L or IN718, were taken from 5 different arbitrary points from each material to avoid pores. The bulk material measurements were taken from points outside the vicinity of the interface or the edges of the workpiece, so that the measurements would be taken from fully homogenous 316L or IN718. The Interface was measured from 10 different arbitrary points, so that pores were avoided. The indentation points that measured the interface were placed so that the middle of the indent was on the interface line. The measurements were done for both an as-built and a heat-treated sample. The measurements were performed so that no indentation or measurement would influence another by being taken from positions that were far enough away from each other.

The interface was identified in-situ during each measurement. Figure 23 showcases the use of the microscope to detect the interface.

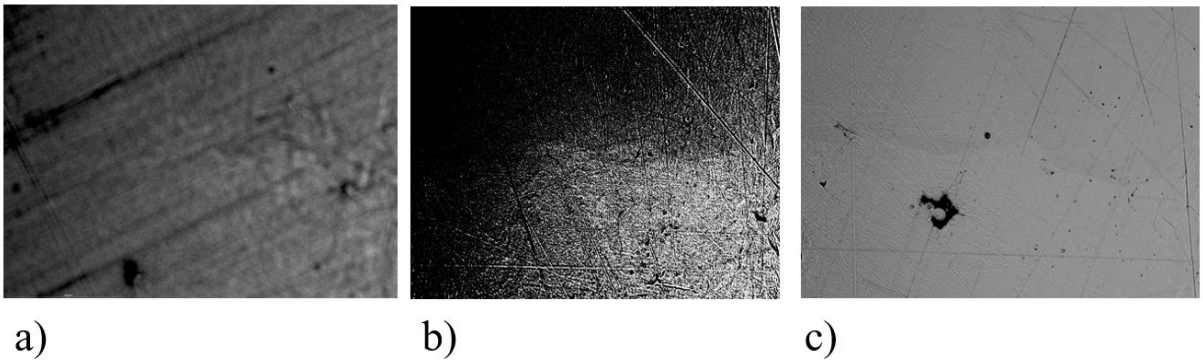

Figure 23. Different micrographs taken from the interface, using different settings for focus, contrast, light and exposure.
a) The blurry, out-of-focus image shows the general trend of the interface.
b) The sharp, in-focus and high contrast image shows the clear difference between the two materials.
c) The sharp, in-focus and low contrast image shows the interface with high detail.

As can be seen in Figure 23, the interface of the two metals can be observed with different settings on the microscope and camera. A combination of adjusting these settings was employed in the measurement procedure to detect the interface. Once a location for measurement on the workpiece surface was selected, the measurement would be commenced. A measurement report is seen in Figure 24.

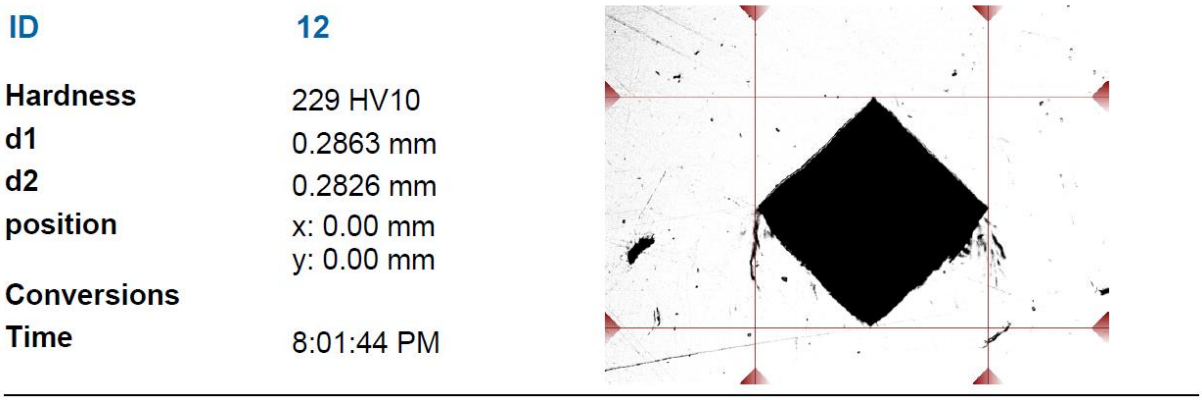

Figure 24. A snapshot of the automatically generated report for measurement 12 of the heat-treated "TL" workpiece. Measurement 12 was made at the interface.

As can be seen in Figure 24, after the indentation was done it would be measured. The software would calculate the corresponding HV10 value from the measurement. It is of note that the interface is only scantly visible in Figure 24, this is due to the fact that the microscopy values were adjusted to create clear contrast between the indentation and the surface.

Hardness is defined by Equation 8. [57]

$$H = \frac{M}{A} \tag{8}$$

Where H is hardness, M is the load applied and A is the area of the impression.

The hardness test utilized in this thesis is the Vickers hardness test. The test is performed with a square pyramid with a 136° angle between opposing faces. The Vickers hardness is defined by dividing the load M by the area of the impression, which can be calculated by knowing the square pyramid and the corners of the impression. [58]

As such, the calculation for the Vickers hardness used is given in Equation 9.

$$\mathrm{HV} = \frac{M}{\frac{d_1 d_2}{2 \sin 68°}} \tag{9}$$

Where HV is Vickers hardness, M is the load applied and d_1 is the first diagonal of the impression and d_2 is the second.

9.4 Corrosion tests

The corrosion tests were performed using a potentiostat. A potentiostat is a device that applies a potential to electrodes and measures the current that flows through an anolyte solution. [59]

A potentiostat may be used to determine the corrosion rate of a given material via determining the electric current which corresponds to the corrosion reaction occurring.

Corrosion rate in this thesis is given in mm/a, or the amount of thickness in millimetres which the corrosion penetrates in a year.

The corrosion tests were performed with 6 corrosion samples made from the test workpieces “TC” (as-built) and “TD” (heat-treated). The corrosion samples were 10 mm by 10 mm by 5 mm by dimensions. The corrosion samples were made of bulk IN718 and 316L as well as the bimetallic combination of both. The workpiece cuts are illustrated in Figure 25.

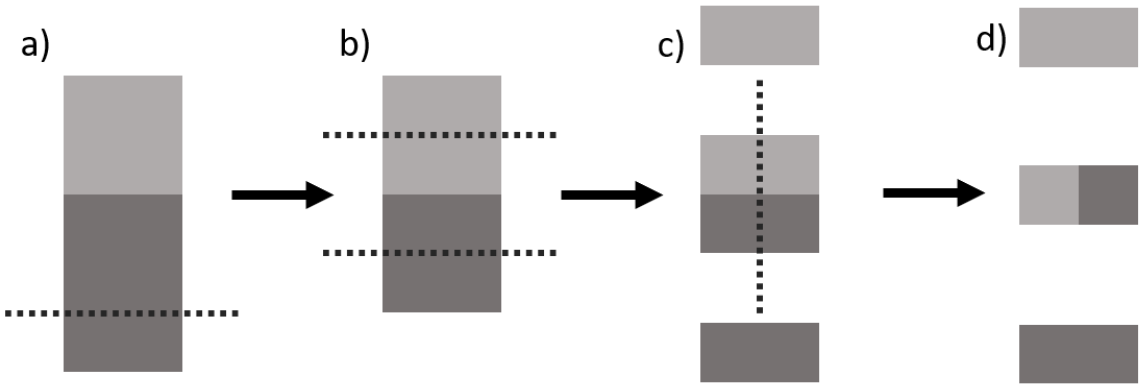

Figure 25. The cuts performed on the 316L-IN718 workpieces.
a) Excess 316L is cut so that 10 mm remains.
b) The bulk portions are cut so that both result in a 5 mm tall 10 mm wide square cuboid.
c) The remaining 10 mm bimetal cube is cut into similar, bimetal, square cuboids.
d) The resulting three square cuboid corrosion test samples needed for the experiments.

These corrosion samples were cut from the test workpieces, then they were tin-soldered to copper wires, then epoxied, as seen in Figure 26.

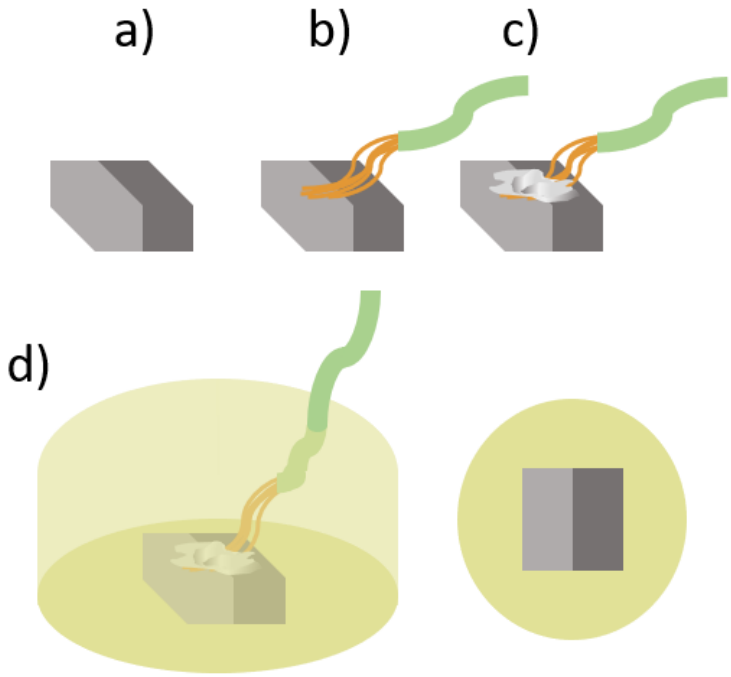

Figure 26. The preparation of the corrosion samples.
a-c) Copper wire is connected to a corrosion sample via tin soldering.
d) The corrosion sample is set in epoxy resin so that only the bottom face is not covered.

These epoxied samples were ground and polished with the grits of 120, 220, 500, 800, and 1200. The resulting corrosion samples were such that they had one exposed surface each with

the approximate area of 100 mm^2 which was either one material in the bulk IN718 and 316L samples or one 100 mm^2 surface where 50 mm^2 was IN718 and 50 mm^2 was 316L.

So, all in all, **three as-built and three heat-treated corrosion samples**, two 316L samples, two IN718 samples and two bimetallic samples, six different sample types in total.

The corrosion behavior was measured using the corrosion samples as the working electrode, a Ag/AgCl electrode as the reference electrode and a graphite electrode as the auxiliary electrode, all submerged in a NaCl solution during the tests. The solution was 3.5% NaCl by weight. This set-up is illustrated in Figure 27.

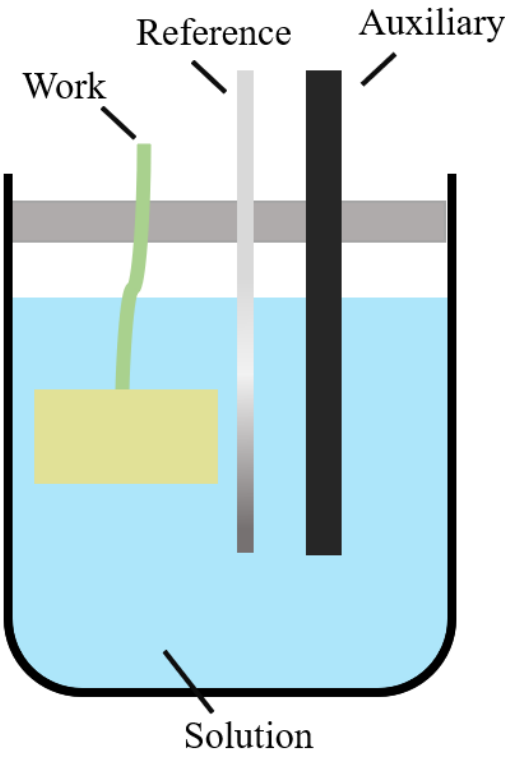

Figure 27. The illustration of the experimental set-up. Where the corrosion sample is the working electrode, the Ag/AgCl electrode is the reference electrode and the graphite electrode works as the auxiliary electrode, all submerged in the 3.5% by weight NaCl solution.

The experiments were conducted for each sample by first performing a 3600 second long "Eoc Monitor" measurement using the Ivium software, followed by "Tafel Plot" with the settings of "E Step" of 1 mV, "Scan Rate" of 5 mV/s. The range of measurements was decided to be -0.3 V downwards and +0.5 V upwards from the nearest 0.1 V of where the "Eoc Monitor" graph ended after 3600 seconds.

These settings naturally resulted in the “Tafel Plot” scan time being 160 seconds. After measurement, a corrosion rate analysis was performed for each “Tafel Plot”.

Three analyses were performed by the potentiostat software for the corrosion rate: Slope, Tafel and Model. Out of these analyses, it was determined which outcome, if any, out of the results was the outlier. In cases where outliers were detected they would be discounted and assumed to be erroneous due to the analysis software’s difficulty to fit a given analysis function to each measurement graph. This procedure resulted in the Model analysis being the one selected as the most trusted option in each measurement, with either both or one of the Slope or Tafel analyses congruing with it in each measurement as illustrated in Figure 28.

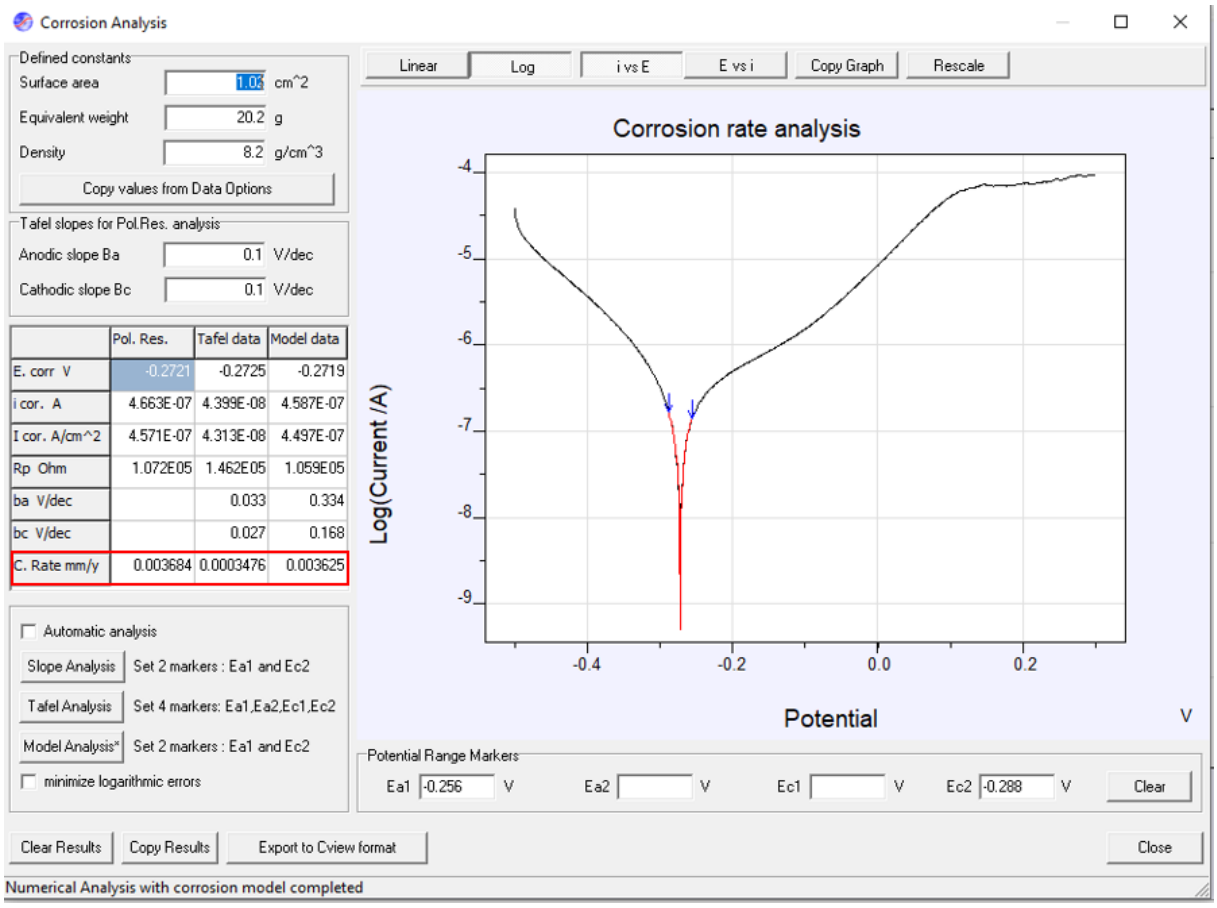

Figure 28. A screen print of the corrosion analysis graphical user interface, showing the corrosion rate analysis of the heat-treated IN718 corrosion sample. Note the corrosion rate measurement, outlined in red. As it can be seen, the “Tafel data” corrosion rate is an outlier in the order of magnitude to the “Pol. Res.” and “Model data” corrosion rates. This most likely is caused by “Tafel Analysis” having been unable to fit properly to the measurement data.

As can be seen from Figure 28, the corrosion behavior analysis required three quantities: the surface area, the equivalent weight (or equivalent mass) and the density. The densities are provided in Table 4 and Table 6. The densities were assumed to be the same for as-built and

heat-treated. The densities of the bimetallic corrosion samples were estimated by using Equation 10.

$$\rho_{\mathrm{BM}} \sim \frac{\rho_{316\mathrm{L}} + \rho_{\mathrm{IN718}}}{2} \tag{10}$$

where $\rho_{316\mathrm{L}}$ is the density of 316L, ρ_{IN718} is the density of IN718 and ρ_{BM} is the density of the bimetallic combination of 316L and IN718, as the equation assumes that the average density of the bimetallic material is the mean average of the two alloys.

The surface areas were measured using a millimetre calliper by having the jaws be flush along the square cross-section of the polished corrosion samples.

The area of the samples was estimated to be larger than which were directly measured with the callipers, in the case that:

- The samples had set into a non-normal angle in the epoxy.
- The samples had been polished so that the cross-section was non-normal.
- The samples had been polished so that the exposed surface was slightly curved.

The different influences that were taken into account during area estimation are illustrated in Figure 29.

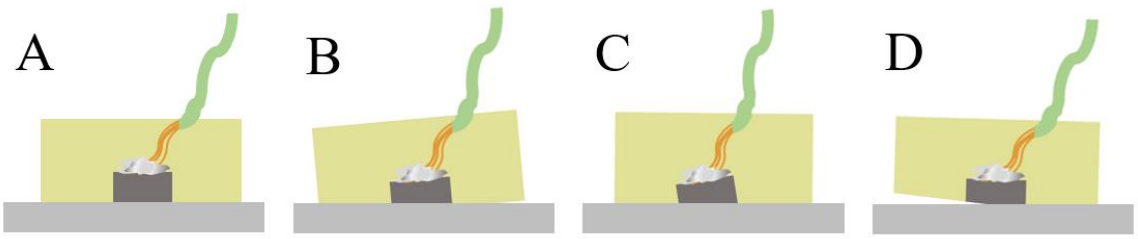

Figure 29. Illustration of the correct (A) and exaggerated sources of increased area (B-D).
A) The sample is set properly in epoxy, and the polishing angle is correct.
B) The sample is set properly in epoxy, but the polishing angle is off.
C) The sample angle is off in the epoxy, but the polishing angle is correct.
D) The sample is polished with two different polishing angles so that the last polishing angle is not full.

In Figure 29, (A) represents the ideal polish, while (B-D) have increased area due to deviation from the ideal angle.

These estimations were done ad hoc during the course of the laboratory experiments.

Lastly, the equivalent weight was determined by a process of determining:

- The average amount of each element present in 316L or IN718.
- The molar mass for each element [60] in alloy at or above 1% prevalence.
- The weighted-by-element-prevalence mean molar mass of the alloy.
- The approximate free valence electron count of the alloys. Based on the most prevalent elements count.

To determine the amount of Fe present in 316L, the minimum and maximum amounts of the other elements in alloy were summed and then from the sum of the minima was subtracted from 100 %, determining the maximum Fe prevalence. Likewise, the minimum prevalence was determined by subtracting the sum of the maxima from 100 %.

The prevalence of Ni present in IN718 was determined using the same procedure as for the Fe in 316L.

The weighted-by-element-prevalence mean molar mass was estimated using Equation 11.

$$\bar{m}_{\mathrm{a,alloy}} \sim \sum_{e=1}^{n} m_{\mathrm{a},i} P_i \tag{11}$$

Where $\bar{m}_{\mathrm{a,alloy}}$ is the average molar mass of the alloy, n is the number of elements at or above 1% prevalence in the alloy, e is the index of the element in alloy, $m_{\mathrm{a},e}$ is the molar mass of an element in alloy and P_e is the prevalence of the element in alloy.

The equivalent weight for each alloy was estimated using Equation 12.

$$M_{\mathrm{E,alloy}} \sim \frac{\bar{m}_{\mathrm{a,alloy}}}{n_{FVE}} \tag{12}$$

Where $M_{\mathrm{E,alloy}}$ is the equivalent weight of the alloy, $\bar{m}_{\mathrm{a,alloy}}$ is the average molar mass of the alloy, n_{FVE} is the number of free valence electrons for the alloy.

The n_{FVE} for each alloy was determined by post hoc justification: the count was elected to be 2 for 316L and 3 for IN718. This is within the boundaries of the free valence electrons in Fe (316L) and Ni (IN718). This selection resulted in equivalent weights similar to those that were determined and utilized in laboratory experiments performed for two other theses which were a part of the same project as this thesis.

As such this post hoc justification is deemed reasonable given that it keeps the equivalent weight — and thus the method of experiment for the corrosion analysis performed with the measurement software — comparable between all three theses in the project.

9.4.1 The Butler-Volmer equation

The corrosion rate analysis utilized in this thesis is represented in theory by the Butler-Volmer equation, which is given in Equation 13. [61], [62]

$$i = i_0[e^{\left(\frac{\alpha_a z_e F}{RT}(E-E_{eq})\right)} - e^{(\frac{-\alpha_c z_e F}{RT}(E-E_{eq}))}] \quad (13)$$

Where i is the current density, i_0 is the exchange current density, α_a transfer coefficient for anodic reactions, z_e is the number of electrons involved in the electrode reaction, F is the Faraday constant, R is gas constant, T is the temperature, E is the potential, E_{eq} is the equilibrium potential, and α_c is the transfer coefficient for cathodic reactions.

Sometimes the Butler-Volmer equation is used with the assumption in Equation 14. [63]

$$\alpha_a + \alpha_c = 1 \quad (14)$$

This is based on a specific interpretation of electron transfer, which does not apply for systems with non-elementary reactions. [64], [65]

In the case of this thesis, the constraint described by Equation 14 does not seem to hold. This could be speculated to be due to the rather complex nature of alloy corrosion, and especially the corrosion behavior of a bimetallic combination of alloys, but this topic would need further study.

Due to the format of the raw corrosion data collected by Ivium Vertex, to which the Butler-Volmer equation would be fitted, the equation was modified to use current instead of current density, as seen in Equation 15.

$$I = I_0[e^{\left(\frac{\alpha_a z_e F}{RT}(E-E_{eq})\right)} - e^{(\frac{-\alpha_c z_e F}{RT}(E-E_{eq}))}] \quad (15)$$

Where I is the current, I_0 is the exchange current, α_a transfer coefficient for anodic reactions, z_e is the number of electrons involved in the electrode reaction, F is the Faraday constant, R is gas constant, T is the temperature, E is the potential, E_{eq} is the equilibrium potential, and α_c is the transfer coefficient for cathodic reactions.

Equation 15 was fitted to the corrosion data acquired from the corrosion analysis manually. Manual selection of parameters was chosen due to what seemed to be secondary corrosion events occurring during the corrosion analysis measurement, as such, a fit function such as least squares could lead to improper results for the values of α_a, α_c and E_{eq}. An example of a manual fit is seen in Figure 30.

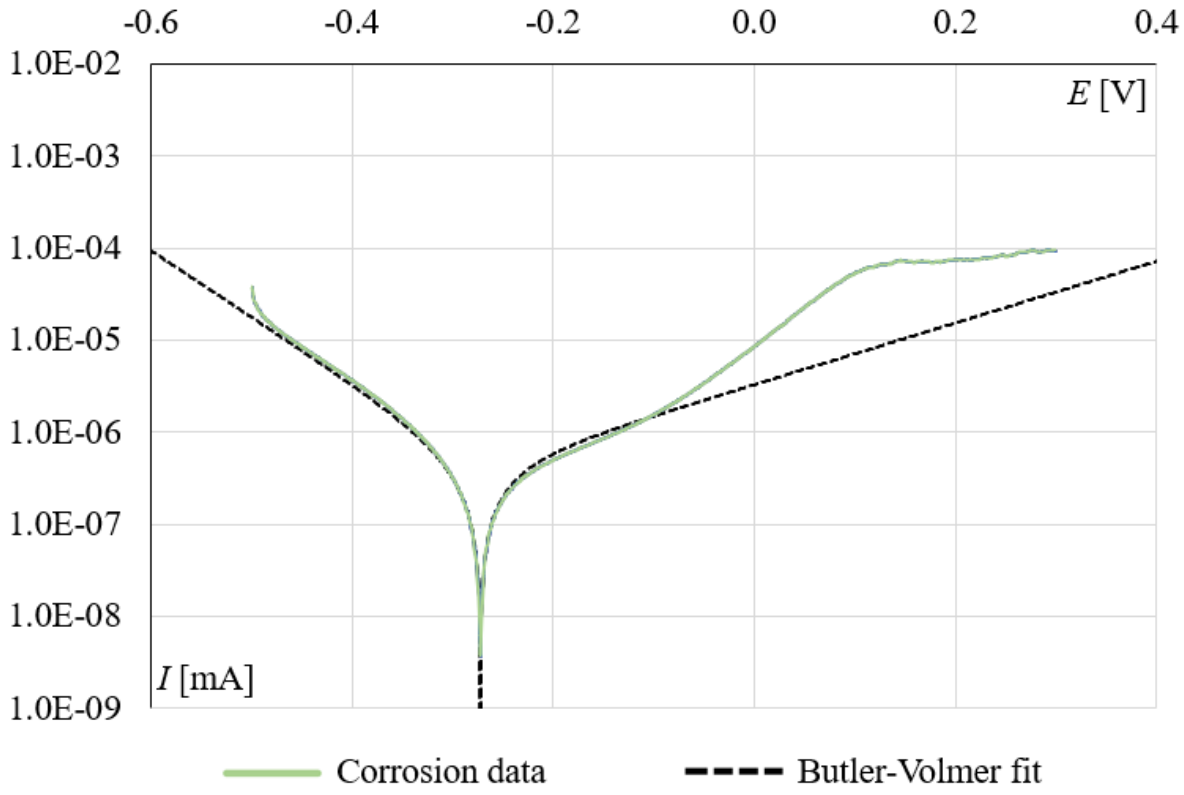

Figure 30. A graph showing a manual Butler-Volmer fit to the corrosion data. Fit done to the corrosion data of the heat-treated IN718 sample.

Figure 30 shows the corrosion data of the heat-treated IN718 sample. As can be seen, there seems to be a climb akin to another reaction occurring after -0.2 V, which could make a least squares method fit improper. However, it is noted that a least squares method fit could be successful, if the range of datapoints to which the fit would be made were limited, but it would then make the selection of the datapoint ranges the determining factor in fit suitability.

A Butler-Volmer fit was performed for data from each corrosion measurement. Each fit had the value of $T = 298$ K. The value of z_e was set to 3 for IN718 data and 2 for 316L and interface data, to represent the most prevalent elements in each sample: Ni, Fe and Fe, respectively. This was chosen to remain consistent with the aforementioned method by which equivalent weight was determined.

I_0, α_a, E_{eq}, and α_c were set as the parameters for the fit. I was set to be a function of E. Note that to produce the graph in Figure 30, a base 10 logarithmic scale was set for the vertical-axis and the values of I were set as absolute values.

10 Results and discussion (part A: PBF-LB\M of the 316L-IN718 workpieces)

This chapter details the results from the manufacture of the workpieces meant for optimization and testing.

10.1 Optimization workpieces

The first round of elimination resulted in workpieces with the parameters of v = 700 mm/s and P = 140, 150 and 170 W being selected for the second round. These parameters were used in the manufacture workpieces “OA”, “OB” and “OD” respectively. The micrographs of these workpieces can be seen in Figure 31.

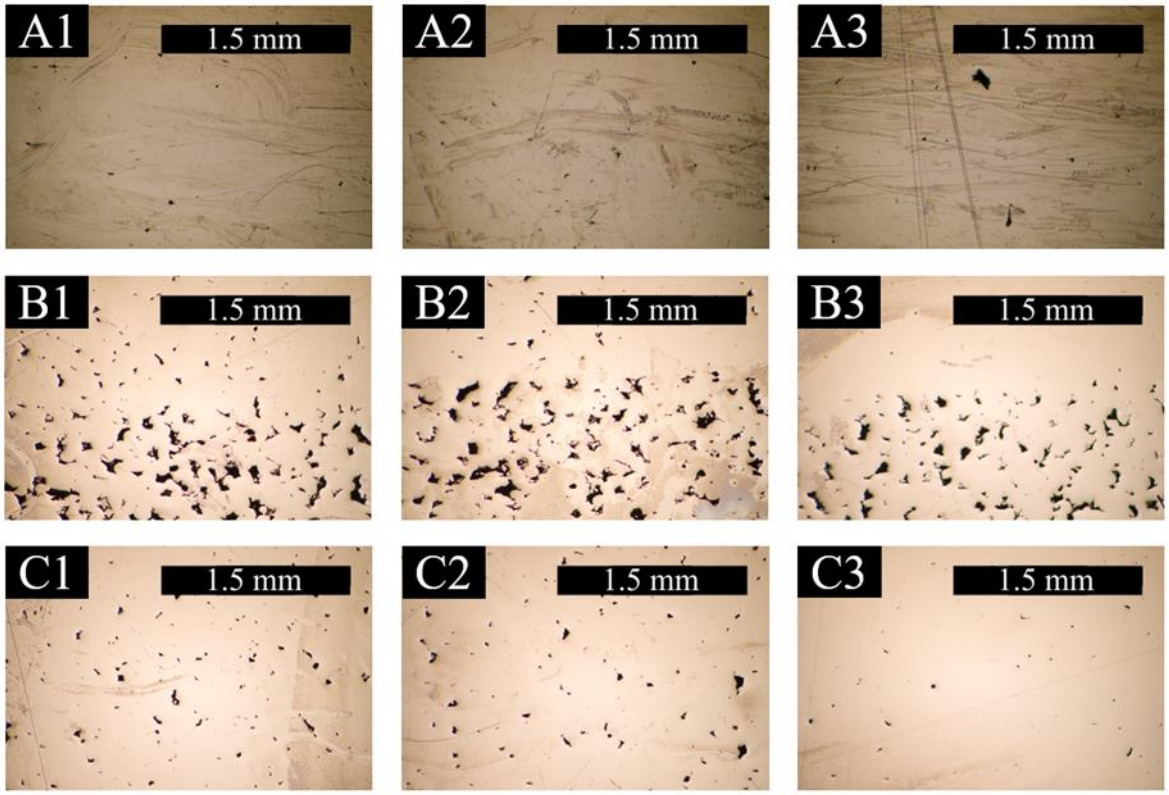

Figure 31. Micrographs of the workpieces.
A-B) Micrographs taken so that the interface is in the middle of the image, with 316L below and IN718 above.
A) Micrographs after the first round of polishing.
B) Micrographs after the second round of polishing.
C) Micrographs of IN718 bulk after second round of polishing
1) Micrographs of workpiece manufactured with v = 700 mm/s and P = 140 W
2) Micrographs of workpiece manufactured with v = 700 mm/s and P = 150 W
3) Micrographs of workpiece manufactured with v = 700 mm/s and P = 170 W

The parameters which produced "OD" (v = 700 mm/s, P = 170 W) were ultimately selected as the best out of all candidates.

Of note in Figure 31 (A1-B3) is the contrast in quality of the 316L. This was an unexpected outcome, as continued polishing lead to sudden increase in detected porosity. The reason for this is hard to estimate, but it could be that some of the discs used to polish the workpieces were contaminated with large particles, which then scraped out material, leaving the pores that can be seen in Figure 31 b). However, the pores resemble lack-of-fusion pores, and as such the curious result could be the product of both the lack-of-fusion defect as well as contamination of the discs.

The grading of the workpieces on the first round is given in Table 18 below, evaluated on a scale of 1 to 5.

Table 18. The grading for the different workpieces after the first round of polishing. The manufacturing parameters are shown under "Workpiece" and the "Grade given to a micrograph" columns show the grade given.

First Round of Polishing					
	Grade given to a micrograph				
Workpiece	1st Image	2nd Image	3rd Image	4th Image	Average
v = 700 mm/s P = 140 W	3	3	4	4	3.5
v = 700 mm/s P = 150 W	3	3	5	3	3.5
v = 700 mm/s P = 160 W	3	3	3	3	3
v = 700 mm/s P = 170 W	2	4	3	4	3.25
v = 800 mm/s P = 140 W	2	2	2	2	2
v = 800 mm/s P = 150 W	2	2	2	2	2
v = 800 mm/s P = 160 W	3	2	3	3	2.75
v = 800 mm/s P = 170 W	2	3	3	2	2.5
v = 900 mm/s P = 140 W	2	1	1	1	1.25
v = 900 mm/s P = 150 W	2	2	2	2	2
v = 900 mm/s P = 160 W	2	2	2	2	2
v = 900 mm/s P = 170 W	2	1	1	2	1.5

The grading of the workpieces on the second round is given and Table 19.

Table 19. The grading for the different workpieces after the second round of polishing. The manufacturing parameters are shown under "Workpiece" and the "Grade given to a micrograph" columns show the grade given.

Second Round of Polishing						
	Grade given to a micrograph					
Workpiece	1st Image	2nd Image	3rd Image	4th Image	5th Image	Average
v = 700 mm/s P = 140 W	3	3	4	3	3	3.2
v = 700 mm/s P = 150 W	4	4	4	3	3	3.6
v = 700 mm/s P = 170 W	5	4	3	3	5	4.0

Due to this selection process, the building parameters of IN718 with workpiece "OD" (P = 170 W, v = 700 mm/s) were selected as the ones to be used in the fabrication of the test workpieces. All tests performed during the experimental phase utilized workpieces manufactured with the parameters of (v = 700 mm/s, P = 170 W).

The results show that the increased volumetric energy density of parameters v = 700 mm/s, P = 170 W led to the best quality of IN718. It could be that the lesser volumetric energy densities caused lack-of-fusion defects due to too little energy input to the system, but this needs further study. The interface was not seen to contain notable defects in the scale of microscopy used.

10.2 Test workpieces and heat treatment

This chapter details the results of the first and the second batch of test workpiece manufacture.

After the first batch of test workpieces was made, it was discovered that the 316L in the workpieces had unexpected high porosity. An example of this can be seen in Figure 32.

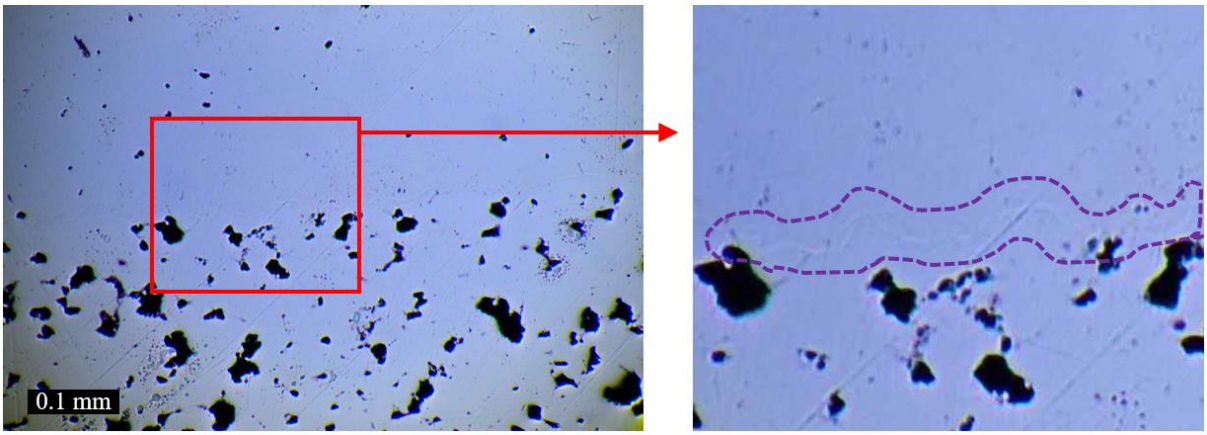

Figure 32. A micrograph from a heat-treated workpiece of the **first test workpiece batch**. 316L is below and IN718 is above. One can see the interface as a faint light outline between the two materials, inside the purple dotted line in the area highlighted by the red square. Note the high porosity of the 316L.

Due to the unexpected porosity seen in Figure 32, it was decided that a second batch of workpieces had to be made, to ensure reasonable results. And as described previously, the volumetric energy density was increased for the 316L portion.

The second batch was manufactured, and the porosity had been reduced to acceptable levels, as can be seen in Figure 35 a).

Figure 33 shows the workpieces after they were removed from the building platform and after the heat treatment plan was executed for half of them.

Figure 33. A photograph of all twelve workpieces from the second test batch. The workpieces are set from designation “TA” to “TL”, in alphabetical order, from left to right. Every other workpiece is heat-treated, and has undergone notable oxidization on the surface during the heat treatment. The two middle parts were the workpieces meant for dilatometry tests, which fell out of the scope of this thesis.

The experimental phase was begun once it was confirmed that the workpieces are of high enough quality to be used in the tests.

11 Results and discussion (part B: the tests for the 316L-IN718 workpieces)

This chapter details the results from the experiments.

All measurements were done with workpieces manufactured with parameters as shown in Table 17. The designation of the letters "A-L" refers to the position of the workpieces on the building platform as described in Table 12.

11.1 Porosity and microstructure

Table 20 and Table 21 give the porosity calculated via the Python program, following the logic of Equation 6.

φ of the first micrograph of as-built IN718, where $p_p = 22250$ and $p_a = 6282656$, is determined using Equation 6:

$$\varphi = \frac{p_p}{p_a} = \frac{22250}{6282656} = 0.003541496 \approx 0.35\%$$

Of note in is the fact that there seemed to be an outlier among the 316L results ($\varphi = 2.61\%$). With the outlier, the average φ would have been 1.32 %, the σ would have been ± 0.66 % and the 95% confidence interval would have been 1.32 ± 1.28 %.

Removing the outlier resulted in the following: the average φ was 1.00 %, the σ was ± 0.12 % and the 95% confidence interval was 1.00 ± 0.22 %.

As can be seen, removing the outlier significantly lowers the standard deviation of the measurements, and makes the range of the 95% confidence interval less than one fifth of the previous. Therefore, **the outlier result was discarded.**

Table 20 shows the results after the removal of the outlier is performed.

Table 20. The measurements from the as-built workpiece “TE” without the outlier 316L measurement.

Porosity		
IN718	316L	Interface
0.35 %	1.19 %	0.46 %
0.19 %	0.91 %	0.73 %
0.43 %	0.94 %	0.46 %
0.29 %	0.95 %	0.47 %
0.19 %		0.35 %
AVG: 0.29 %	AVG: 1.00 %	AVG: 0.49 %
σ: ± 0.10 %	σ: ± 0.12 %	σ: 0.13 %
95% confidence interval:		
IN718:	316L:	Interface:
0.29 ± 0.19 %	1.00 ± 0.22 %	0.49 ± 0.25 %

The porosity results for the heat-treated workpiece TH are provided in Table 21 below.

Table 21. The measurements from the heat-treated workpiece TH.

Porosity		
IN718	316L	Interface
0.25 %	1.78 %	0.87 %
0.29 %	1.92 %	0.79 %
0.37 %	1.78 %	0.98 %
0.31 %	1.87 %	1.27 %
0.42 %	1.52 %	0.64 %
AVG: 0.33 %	AVG: 1.77 %	AVG: 0.91 %
σ: ± 0.06 %	σ: ± 0.14 %	σ: ± 0.22 %
95% confidence interval:		
IN718:	316L:	Interface:
0.33 ± 0.12 %	1.77 ± 0.27 %	0.91 ± 0.42 %

Figure 34 shows the results of Table 20 and Table 21.

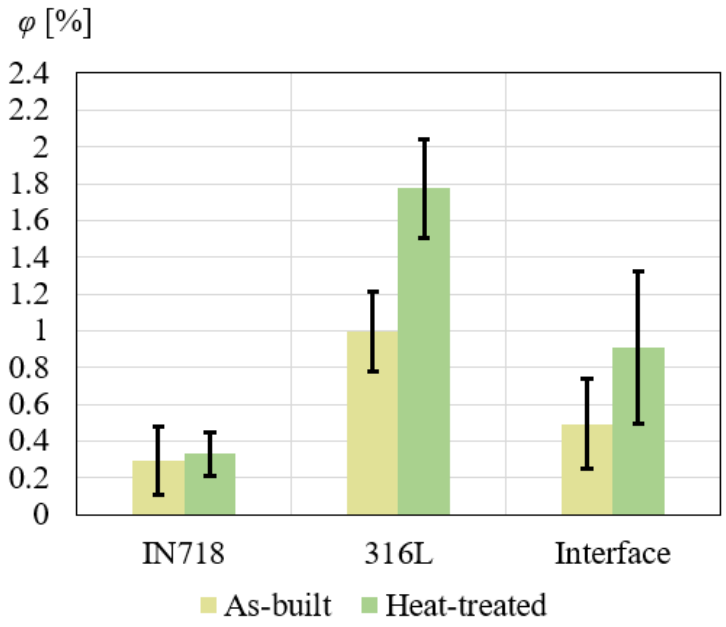

Figure 34. The 95% Confidence intervals for the levels of porosity of each type of measurement from Table 20 and Table 21 represented.

As Figure 34 shows, the least porosity was encountered in IN718. 316L had notable porosity, near 1% for as-built and almost 1.8% for heat-treated. The as-built porosity could be caused by the circumstance that the workpieces were manufactured using recycled 316L powder, as the use of recycled powder is attributed to increases in porosity via changes to particle size and morphology as well as the chemical composition of the powder. [66] And as the heat treatment plan was meant for IN718, the porosity of 316L could have risen due to thermal stresses expanding pores.

Porosity can result from either systematic or stochastic flaws in PBF-LB. According to Snow et al., systematic flaws are defined as flaws that occur due to part geometry, hatching strategy or process parameters, and are as such related to the build plan. Systematic flaws are more localized to specific portions or areas of the built workpiece compared to stochastic flaws and their locations are more predictable. For example: lack-of-fusion flaws can be systematic - (hatching strategy) or stochastic (particle packing or spatter). Stochastic flaws are defined as flaws that are probabilistic in nature and as such the location of stochastic flaws in a finished workpiece is harder to predict. Examples of stochastic flaws are gas porosity, keyholing, random power fluctuations and spatter induced flaws. [67]

The porosity studied in this thesis is presumed to be caused by stochastic flaws, as systematic flaws related to the hatch and contour as well as the end of scan tracks are avoided due to the polishing process removing enough material from the surface.

Figure 34 shows that heat treatment increased porosity for each workpiece. It is also worthy of note that the interface porosity increased notably in the heat treatment.

The interface measurements loosely correspond to the mean average of the two bulk material measurements, both for as-built and heat-treated. As such the increase of the porosity measured from the interface after heat treatment could mostly be attributed to the increase in the porosity of 316L after heat treatment. However, it is important to note that **the porosity measured from the interface was less than the mean average of the 316L and IN718 porosities** for both as-built and heat-treated workpieces. This is determined for both as-built and heat-treated porosity measurements by using Equation 7. The values used for φ_{BM}, φ_{316L}, and φ_{IN718} being the calculated averages as shown in Table 20 and Table 21.

As-built:

$$\varphi_{\Delta BM} = \varphi_{BM} - \frac{\varphi_{316L} + \varphi_{IN718}}{2} = 0.49\% - \frac{1.00\% + 0.29\%}{2} = -0.155\%$$

Heat-treated:

$$\varphi_{\Delta BM} = \varphi_{BM} - \frac{\varphi_{316L} + \varphi_{IN718}}{2} = 0.91\% - \frac{1.77\% + 0.33\%}{2} = -0.14\%$$

The $\varphi_{\Delta BM}$ being -0.155% for as-built and -0.14% for heat-treated. This result could imply that the interface contains less porosity than the bulk materials, as otherwise the mean average of the 316L and IN718 porosities would be the same as or similar to the porosity at the interface. The porosity of the interface being lower than the mean average of the bulk porosities suggests that the metallurgical bonding between 316L and IN718 is sound, as low porosity of the interface is noted as indicating good metallurgical bonding. [37] However, this matter would require further study.

As comparison, Mohd Yusuf et al. reported an overall porosity content of 0.81% for bimetallic 316L-IN718, with a 0.27% porosity content for the interfacial region. Mohd Yusuf et al. manufactured both the 316L and IN718 portions with a laser power of 300 W, a scanning speed of 900 mm/s, a layer thickness of 30 µm and a hatch spacing of 80 µm. [37]

Figure 35 shows a micrograph of the as-built workpiece at the interface for the purposes of visual analysis of the microstructure.

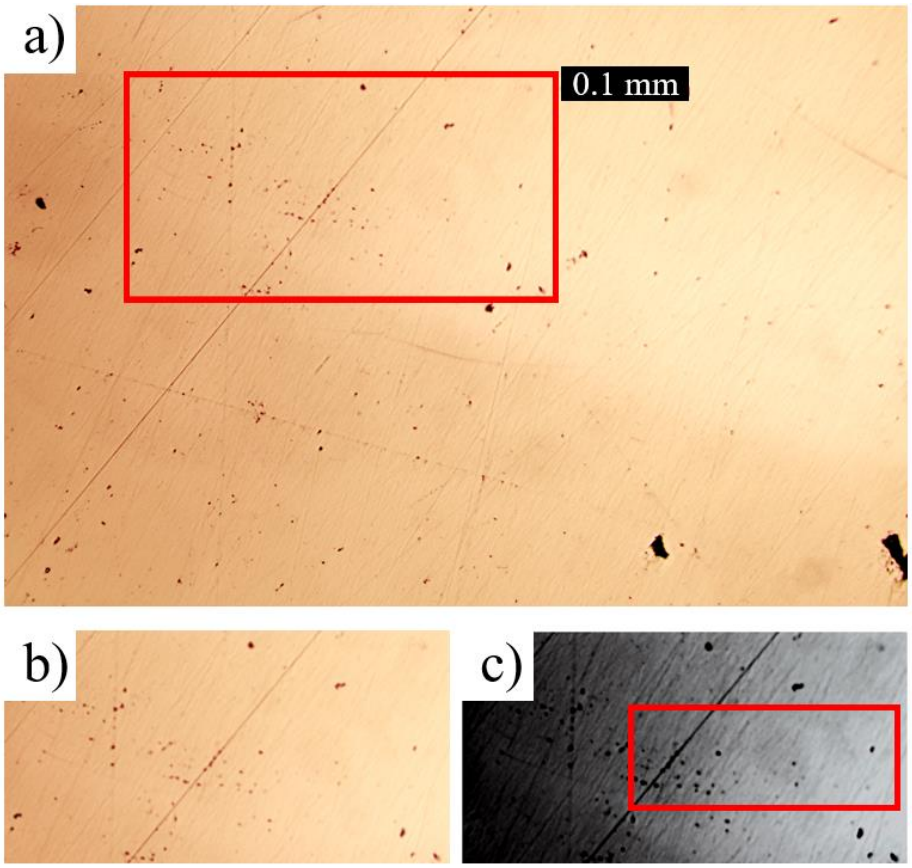

Figure 35. a) A micrograph of the as-built workpiece “TE”, taken with a lens using 20 times magnification with a camera lens using 0.5 times magnification. IN718 is above, 316L is below.
b) The area highlighted with the red square in a).
c) The area in b) with adjusted contrast, where the transition from one material to another is highlighted

As can be seen from Figure 35, the transition zone from one material to the other contains porosity. However, the porosity in the transition zone seems to be present in a level of similar magnitude as in bulk materials. As such the interface seems to have an acceptable integrity.

However, the porosity highlighted in Figure 35 c) could be melt pool porosity at the interface. The porosity seemingly being in the first layer of IN718 being manufactured on top of the 316L substrate. A similar phenomenon can be seen in Figure 36 and Figure 37.

Figure 36 shows a micrograph of the heat-treated workpiece at the interface.

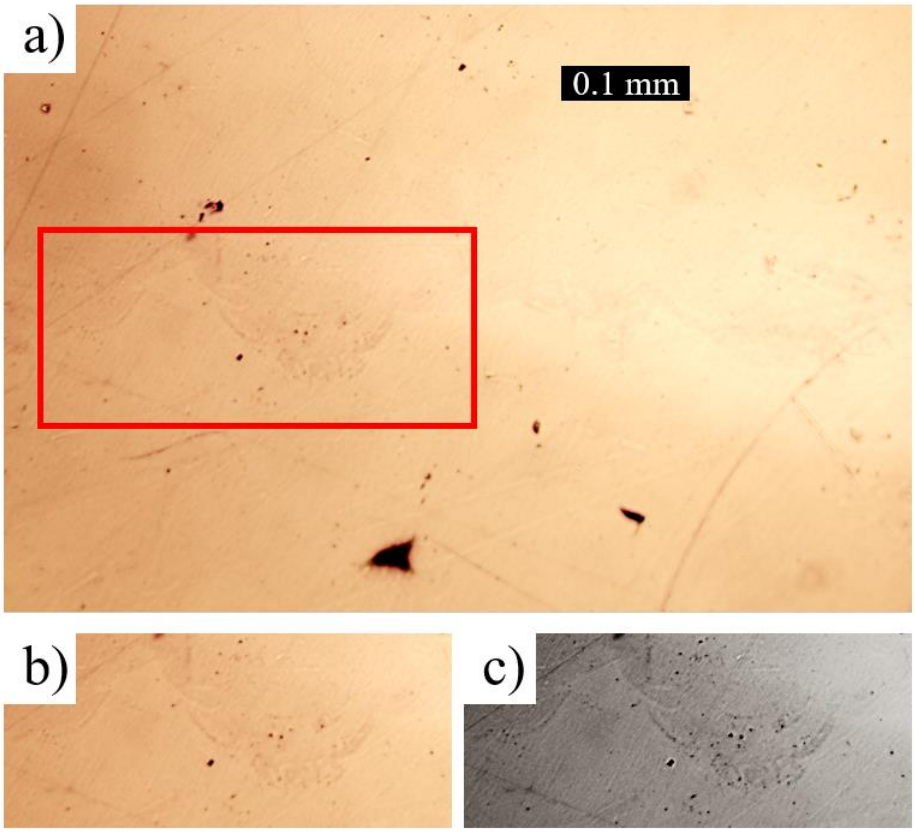

Figure 36. a) A micrograph of the heat-treated workpiece “TH”, taken with a lens using 20 times magnification with a camera lens using 0.5 times magnification. IN718 is above, 316L is below.
b) The area marked with the red square in a).
c) The area in b) with adjusted contrast, the transition zone can be seen readily.

Porosity is seen to occur near the interface and on it in certain portions in Figure 36, but there are also portions where seemingly no porosity is present. Furthermore, it is of note that the micrographs of the heat-treated workpieces are clearer in their microstructure. It is speculated that heat treatment could have made the material more responsive to the etchant. This is corroborated by the corrosion tests, where every heat-treated workpiece possessed a higher corrosion rate compared to their as-built counterpart. However, this would need further study.

In Figure 36 c), the flow of IN718 and 316L can be seen with a small curved line of 316L fraying from the bulk into the IN718. Figure 36 c) is further analysed in Figure 37.

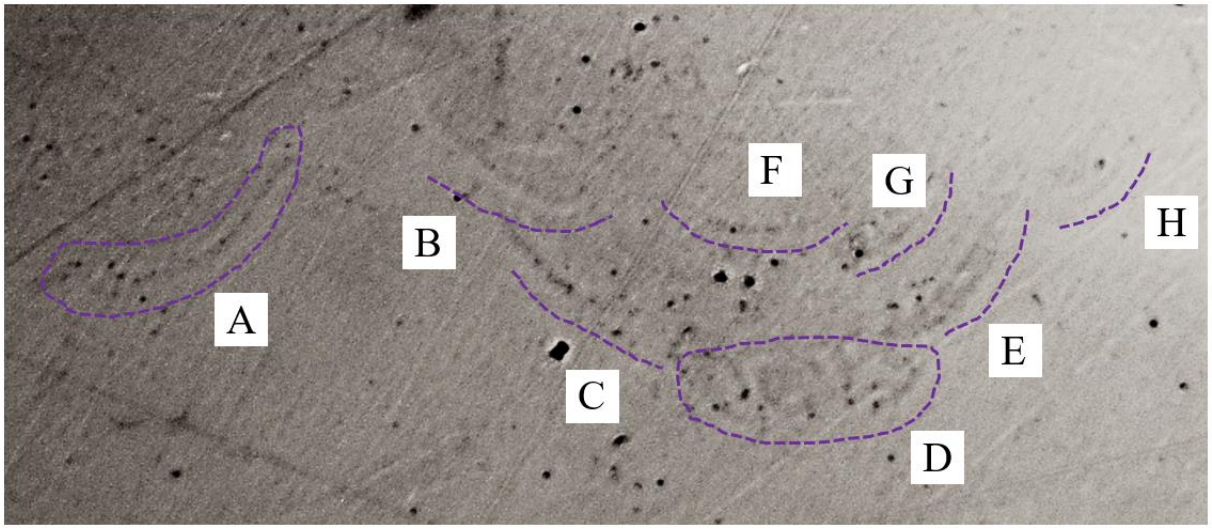

Figure 37. Analysis of the micrograph seen in Figure 36 c). The interface is in the center, 316L is below and IN718 is above.
A) The bottom of a scan track with melt pool porosity.
B) A fraying barb of 316L that has departed from the scan track, potentially caused by Marangoni convection.
C-E) The bottom of multiple scan tracks next to each other.
C) The bottom of a scan track with melt pool porosity.
D) IN718 precipitation into the 316L substrate.
F-G) Meltpool porosity of a scan track corresponding to a new layer built on a previous one (C-E).
E) Interface at the edge of a scan track.
H) Interface at the edge of a scan track above E.

Figure 37 shows the material interface. The interface, which is the line over which 316L begins to have IN718 built on top of it, is seen to be tortuous.

The following is speculative analysis of the micrograph:

- (A) Shows meltpool porosity on an IN718 scan track built over the 316L substrate.
- (B) Shows a thin barb-like mass of 316L that has frayed and separated from the scan track, potentially caused by Marangoni convection.
- (C-E) Shows the bottom of multiple scan tracks next to each other. (C) Shows that the scan track has melt pool porosity, yet in (E) there is no melt pool porosity.
- D) Shows meltpool porosity and or cracking on the 316L substrate, causing IN718 precipitation into the 316L substrate.
- F-G) Show meltpool porosity of a scan track corresponding to a layer above (C-E).
- H) Shows the 316L substrate elevation increasing after, continuing the tortuous pattern.

However, it is important to remember that the list above is speculative and that this topic would need further study.

Figure 36 c) contains a similar Marangoni convection effect can be seen as in Figure 11 b), this is shown in Figure 38.

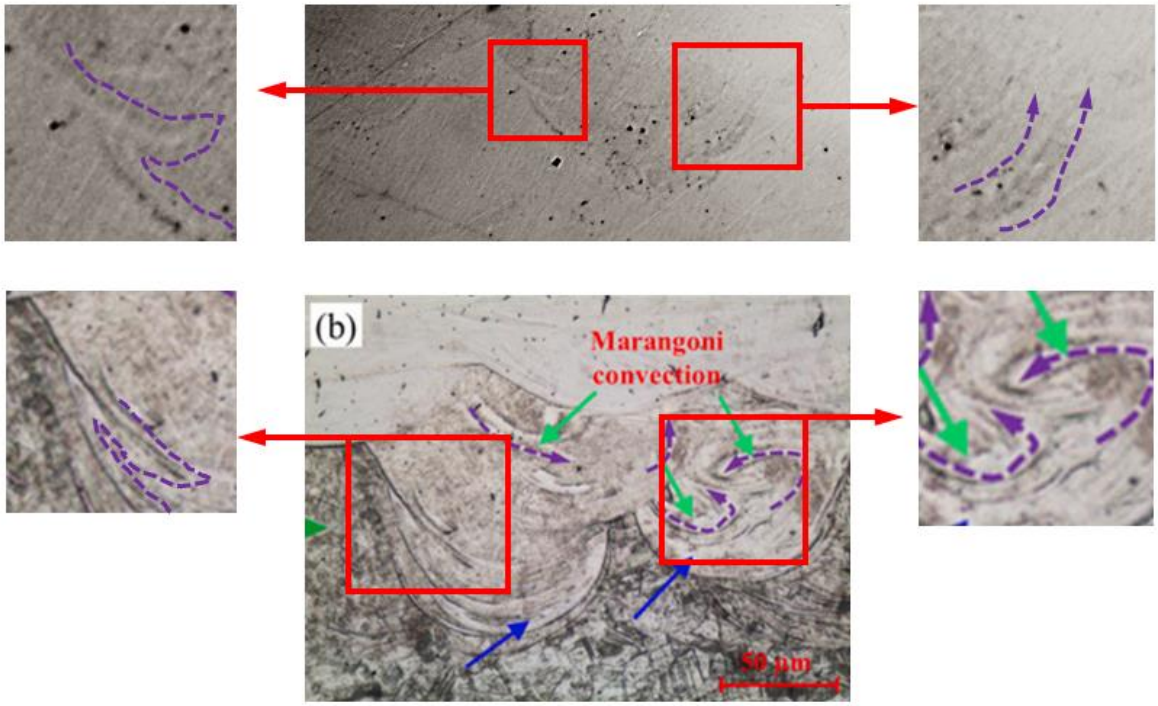

Figure 38. A comparison between Figure 36 c) and Figure 11 b), and notes of similar interface phenomena. [35]

As can be seen from Figure 38, the behavior of the 316L steel substrate is similar to that which was observed with a CrMn stainless steel substrate. [35] Note the barb-like fraying can be seen in both Figure 11 b) and Figure 36 c), as shown in Figure 38.

To reiterate, it is noted that the interface between IN718 and 316L possesses a tortuous wavy interface pattern. Furthermore the interface region contains patterns of substrate precipitating to the upper material similar to patterns in literature which are attributed to Marangoni convection with other steels. [35] It is noted that the interface also has IN718 precipitation in the 316L substrate potentially due to melt pool cracking, the voids of which the molten IN718 filled. Lastly, as can be seen, the interface between IN718 and 316L occurs over multiple scan tracks, and as such has a slight graduality before the material becomes full IN718 bulk. This gradual area seems to be within one to three layers, with the first layer built on the 316L substrate experiencing most of the gradual shift in material composition.

11.2 Geometrical accuracy

The measurements for the geometrical accuracy are provided in Table 22. Side-to-side is measured from the left and right surfaces of the workpiece. Rounding radius is measured from the beginning of the radius at the side and the end on the top surface. Surface-to-letter compares the level between the marking and the workpiece surface. IN718-to-316L measures the offset between the materials on both sides of the interface.

Table 22. The geometrical accuracy measurements for the as-built and heat-treated workpieces. The decimal accuracy is set to the given amount to allow for the finer measurements to not be subsumed by the side-to-side measurements.

As-built				
[mm]	Side-to-side	Radius	Surface-to-letter	IN718-to-316L
IN718	9.870	0.589	0.304	
316L	9.904	0.552	0.293	
Interface				-0.028
Heat-treated				
[mm]	Side-to-side	Radius	Surface-to-letter	IN718-to-316L
IN718	9.858	0.596	0.309	
316L	9.948	0.515	0.295	
Interface				-0.034

The ideal measurements are given in Table 23, which represent the values that the CAD file was made with.

The ideal measures are shown in Table 23.

Table 23. The geometrical accuracy measurements for the ideal workpiece.

[mm]	Side-to-side	Radius	Surface-to-letter	IN718-to-316L
IN718	10.000	0.500	0.300	
316L	10.000	0.500	0.300	
Interface				0.000

The deviation from ideal measures are shown in Table 24.

Table 24. The geometrical accuracy measurements for the as-built and heat-treated workpieces.

As-built deviation				
[mm]	Side-to-side	Radius	Surface-to-letter	IN718-to-316L
IN718	0.130	0.089	0.004	
316L	0.096	0.052	0.007	
Interface				0.028
Heat-treated deviation				
[mm]	Side-to-side	Radius	Surface-to-letter	IN718-to-316L
IN718	0.142	0.096	0.009	
316L	0.052	0.015	0.005	
Interface				0.034

Figure 39 shows the deviation of the workpiece dimensions from the ideal workpiece dimensions measured in the geometrical accuracy tests.

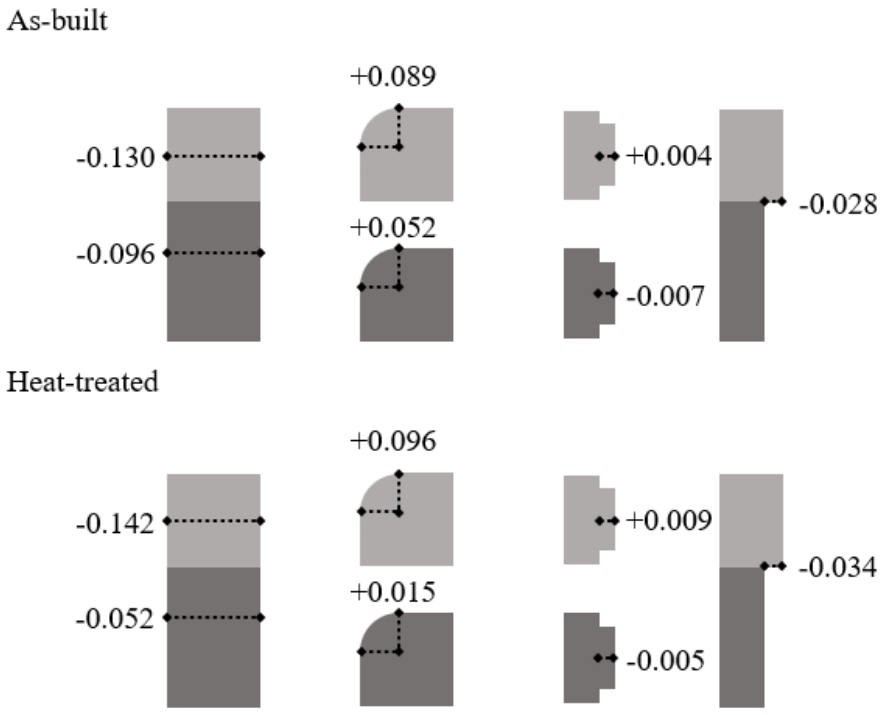

Figure 39. The deviation of the measured workpiece dimensions from the ideal workpiece dimensions given in millimeters. The negative sign signifies a dimension smaller than the ideal while a positive signifies opposite.

No quantitative error analysis can be performed on these values due to the fact that the values come from a single measurement.

For comparison, Veetil et al. studied 316L workpieces manufactured via PBF-LB with a nominal diameter of 10.0 mm that was increased to a real print diameter of 10.5 mm. Veetil et al. observed that all samples built had as-built diameters lie in the range of 10.07 mm to 10.12 mm. [68]
Furthermore, Gradl et al. observed a systematic mean tolerance of 23.8 ± 5.5 µm with a 99.9% confidence interval for features of IN718 and also determined an upper control limit of +220 µm and a lower control limit of -260 µm for IN718 manufactured via PBF-LB\M. Gradl et al. determined their results from IN718 geometric feature build plates manufactured via PBF-LB. [69]

Comparing the results of this thesis to the observations of Gradl et al., it can be noted that the measurements are within the determined control limits and the surface-to-letter measurements are well within the systematic mean tolerance. [69]
It can also be noted that all of the side-to-side measurements are below the ideal measurement and none over. This possibly being due to a similar shrinkage occurring for the 316L-IN718 workpieces that was reported to have occurred for the 316L workpieces by Veetil et al. [68]

It is difficult to estimate the effect that heat treatment has for the geometrical accuracy. This is due to the workpieces that were measured being different ones, and not the same one before and after heat treatment. This decision was made due to the limits of the project schedule. However, it would also be difficult to attribute any single cause to the geometry changing, as many factors influence the outcome of the changes to geometrical accuracy due to heat treatment. It is speculated that the influence of the heat treatment to the pieces would be the result of differences in thermal characteristics between the materials. From thermal conductivity to thermal expansion coefficients. These differences could cause thermal stresses and as such warpage and deformation based on thermal expansion and contraction. However, this matter would require further study.

11.3 Hardness measurements

The measurements for the as-built workpiece TK is provided in Table 25.

The basis for the calculation which the hardness test software used to determine Vickers hardness is shown in Equation 9.

Table 25. The measurements from the as-built workpiece TK.

HV10 [kgf/mm^2]			
IN718	316L	Interface	
255	190	203	220
265	198	216	226
280	190	223	231
280	182	215	229
276	190	218	201
AVG: 271.2	AVG: 190.0	AVG: 218.2	
σ: ± 9.8	σ: ± 5.1	σ: ± 9.5	
95% confidence interval:			
IN718:	316L:	Interface:	
271 ± 20	190 ± 10	218 ± 19	

The measurements for the heat-treated workpiece TL is provided in Table 26.

Table 26. The measurements from the heat-treated workpiece TL.

HV10 [kgf/mm^2]			
IN718	316L	Interface	
438	182	227	218
436	177	229	230
423	180	242	217
422	189	234	226
424	182	250	239
AVG: 428.6	AVG: 182.0	AVG: 231.2	
σ: ± 6.9	σ: ± 3.9	σ: ± 9.8	
95% confidence interval:			
IN718:	316L:	Interface:	
429 ± 14	182 ± 8	231 ± 20	

Note from Table 25 and Table 26 how the heat treatment influences the material properties, with a notable improvement to the hardness of IN718 and a minor detriment to 316L.

Figure 40 shows the results of Table 25 and Table 26.

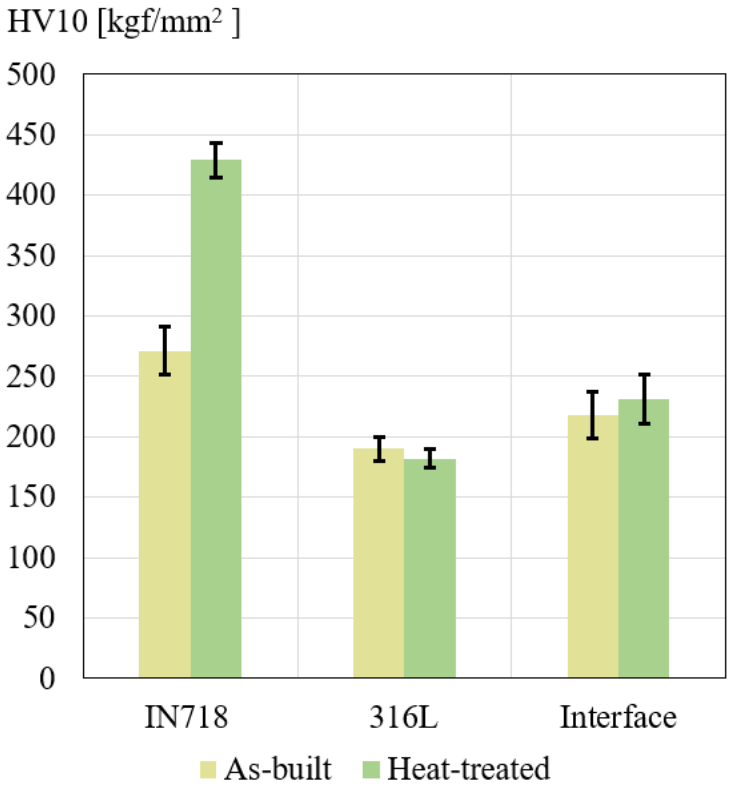

Figure 40. The 95% Confidence intervals for the HV10 values of each type of measurement from Table 25 and Table 26 represented.

As Figure 40 shows, the heat treatment greatly improved the hardness test performance of IN718. The heat treatment also seems to have caused a detriment to the hardness of the 316L. Given that the heat treatment was meant for IN718, and as such it was not optimized for the enhancement of 316L, the result is deemed to not be concerning. The interface became slightly harder after the heat treatment.

The result of the increased hardness in IN718 could be attributed to the promotion of the formation of γ′ and γ″ phases during the ageing treatment. [49] The γ′ and γ″ phases are coherent with the austenitic γ matrix. [70] The γ″ phase is a centered tetragonal structure, the precipitates of which adopt a disc-like structure during ageing. γ″ is the more influential phase out of γ′ and γ″, as it is more prominent out of the two hardening phases and as the hardening effect of γ″ is greater. [70]

The main strengthening mechanisms of the precipitates of the γ″ phase is coherence deformation. [70] Precipitates of the γ″ phase acts as an inhibitor to dislocation movement. [71]

For context: mechanisms that impede dislocations due to the creation of additional surfaces are:

- The creation of additional matrix-precipitate interfaces (chemical strengthening).
- Stacking fault formation in the precipitate (stacking fault strengthening).
- Formation of antiphase domain boundaries in the precipitate (order strengthening). [72]

316L manufactured via PBF-LB\M is shown to experience a loss of hardness when undergoing heat treatment at 700 °C for 3 hours. [73] According to Suárez Ocaño et al. [73] the hardness changed from approximately 216 HV1 to approximately 191 HV1. As such, the observed drop in hardness for 316L in this thesis after the IN718 heat treatment is not anomalous when compared with the effect reported by Suárez Ocaño et al.

The hardness of the materials studied in this thesis are compared to values found in literature in Table 27.

Table 27. The hardness values studied in this thesis compared to values found in literature.

Origin:	This thesis			Naskar et al. [74]	Suárez Ocaño et al. [73]	Grzelak et al. [75]
Type:	HV 10 [kgf/mm2] (standard deviation)			HV0.5	HV1	HV0.5
Material:	IN718:	316L:	Interface:	**IN718**	**316L**	**316L**
As-built:	271.2 ± 9.8	190.0 ± 5.1	218.2 ± 9.5	327 ± 6	-	216.44 ± 3.65
Heat-treated:	428.6 ± 6.9	182.0 ± 3.9	231.2 ± 9.8	485 ± 5[*]	191 ± 3[†]	-
[*]Heat treatment: 1093 °C for 2 hours, 980 °C for 1 hour, 720 °C for 8 hours, 620 °C for 8 hours. [74]						
[†]Heat treatment: 450 °C for 4 hours, 700 °C for 3 hours. [73]						

The values found in literature given in Table 27 can be seen to be reminiscent of the values measured in this thesis. Naskar et al., Suárez Ocaño et al. and Grzelak et al. all performed their measurements with material manufactured via PBF-LB\M. [73], [74], [75]

As can be seen from Table 27, the values of IN718 follow a similar increase in hardness between the results in this thesis and as reported Naskar et al. [74] However, the values reported by Naskar et al. are approximately 55 HV greater for as-built and heat-treated.

The heat treatment protocol used by Naskar et al. was:

- Homogenization at 1093 °C for 2 hours
- Air cooling to room temperature
- Solution annealing at 980 °C for 1 hour
- Air cooling to room temperature
- Ageing treatment at 720 °C for 8 hours
- Cooling to 620 °C with a cooling rate of 55 °C/h.
- Continuing ageing treatment at 620 °C for 8 hours. [74]

It was concluded that the heat treatment Naskar et al. [74] was similar enough to the one employed in this thesis to warrant comparison.

Table 27 shows that the hardness of 316L is approximately 25 HV1 (as-built, [75]) and 10 HV1 (heat-treated, [73]) greater compared to the HV10 values measured in this thesis.

While Grzelak et al. [75] did not report a heat treatment plan, Suárez Ocaño et al. [73] reported the following heat treatment plan for 316L manufactured via PBF-LB\M:

- Heated from room temperature to 450 °C at a rate of 10 °C/min
- Kept at 450 °C for 4 hours.
- Cooled from 450 °C to room temperature at a rate of 10 °C/min
- Heated from room temperature to 700 °C at a rate of 10 °C/min
- Kept at 700 °C for 3 hours.
- Cooled from 700 °C to room temperature at a rate of 10 °C/min

The heat treatment reported by Suárez Ocaño et al. [73] is different to the one used in this thesis, it was still included in the comparison due to the prolonged time the 316L was kept at 700 °C possible having similar effects in the microstructure of 316L as the heat treatment of 8 hours at 718 °C that was used in this thesis.

11.4 Corrosion tests

The results of the "Eoc monitor" measurements are given in Appendix 2.

The corrosion rate measurements for the as-built and heat-treated samples are provided in Table 28.

Table 28. The corrosion rate measurements from the as-built and heat-treated corrosion samples. All results were acquired using model analysis of the Ivium Vertex software.

Corrosion Rate		
	As-built [mm/a]	Heat-treated [mm/a]
316L	0.11	0.13
Interface	0.0011	0.0044
IN718	0.0029	0.0036

As can be seen on the Table 28, the results follow a pattern of heat treatment causing an increase in corrosion rate. This could be due to the fact that the heat treatment caused the formation of corrosion-prone phases in the materials or because it disrupted the passive film.

The results of Table 28 are seen in Figure 41.

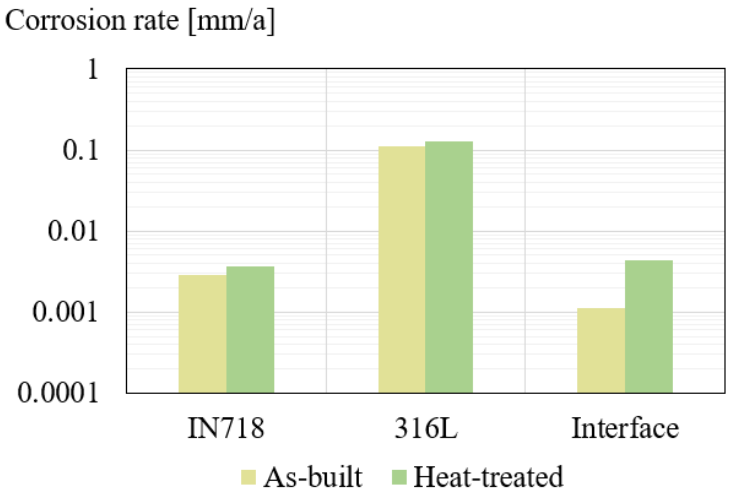

Figure 41. The results of the corrosion rate measurements. Note the logarithmic scale and the gridlines.

In Figure 41, notice the difference in the order of magnitude between the corrosion rates of 316L and the corrosion rates of IN718 and the interface. This could be due to the use of recycled powder and the noted porosity in the samples giving more surface area for the corrosion to take place on.

No quantitative error analysis can be performed on these values due to the fact that the values come from a single measurement.

Table 29 compares the values for the corrosion rate measured in this thesis with ones reported by literature.

Table 29. The corrosion rate values studied in this thesis compared to values found in literature.

Corrosion rate [mm/a]						
Origin:	This thesis			Siddaiah et al. [76]	Mythreyi et al. [77]	Yousif et al. [78]
Material:	IN718:	316L:	Interface:	**IN718**	**IN718**	**316L**
As-built:	0.0029	0.11	0.0011	0.082	0.27 ± 0.06	0.000721
Heat-treated:	0.0036	0.13	0.0044	-	22.45 ± 0.06*	-
*Heat treatment: 1065 °C for 1 hour, 720 °C for 8 hours, 620 °C for 8 hours. [77]						

The heat treatment by Mythreyi et al. [77] reported the following heat treatment plan for IN718 manufactured via PBF-LB\M:

- Solution annealing at 1065 °C for 1 hour
- Fan cooling
- Double ageing treatment at 720 °C and 620 °C for 8 hours each.
- Air cooling
- Shot peening

Yousif et al. noted that: "…*the results in this work clearly show the relationship between porosity and corrosion rate.*" [78] As such, the high corrosion rate measured for 316L in this thesis being possibly connected to the notable porosity observed is mirrored in the literature.

Pores increase corrosion rate due to them acting as catalytic sites in which pitting corrosion occurs. [78] Pores also impede the formation of an uniform protective film on the surface, allowing for localized corrosion. [78]

As such, further study of the corrosion behavior of 316L manufactured via PBF-LB\M and heat-treated with a heat treatment plan optimized for IN718 would be warranted.

Further study could allow to determine the level of influence that porosity has and to see the level of corrosion for samples without notable porosity.

Table 30 gives the parameters I_0, α_a, E_{eq}, and α_c determined from Equation 15 being fitted to the raw corrosion data.

Table 30. The parameters: I_0, α_a, E_{eq}, and α_c determined by fitting the Butler-Volmer equation (Equation 15) to corrosion data from each corrosion sample, both for as-built (AB) and heat-treated (HT) data.

Sample:	AB IN718	HT IN718	AB Interface	HT Interface	AB 316L	HT 316L
z_e [1]	3	3	2	2	2	2
I_0 [mA]	7.60E-7	4.00E-7	1.55E-7	1.75E-5	2.65E-5	2.00E-5
α_a [1]	0.020	0.065	0.035	0.055	0.055	0.04
α_c [1]	-0.15	-0.14	-0.14	-0.105	-0.04	-0.04
E_{eq} [V]	-0.267	-0.272	-0.225	-0.570	-0.631	-0.663

When reading Table 30, it is good to keep in mind that these values were acquired with a manual fit, and that the raw corrosion data from the measurements did not necessarily align well with the Butler-Volmer equation when fitted due to the data potentially having recorded other corrosion events. As such this topic would warrant further research.

Given the degree of reliability that is to be expected for the results, it is suggested to limit observations to the differences in order of magnitudes when reading Table 30. As can be seen from Table 30 the notable difference after heat treatment occurs for the interface. The exchange current increases by approximately two orders of magnitude.

Exchange current density, and by extension, exchange current, is linked to the rate constant in chemical reactions, being analogous to it. [79], [80] As such the results given in Table 30 are in agreement with the results given in Table 29.

The raw corrosion data and the Butler-Volmer fits are illustrated in Figure 42.

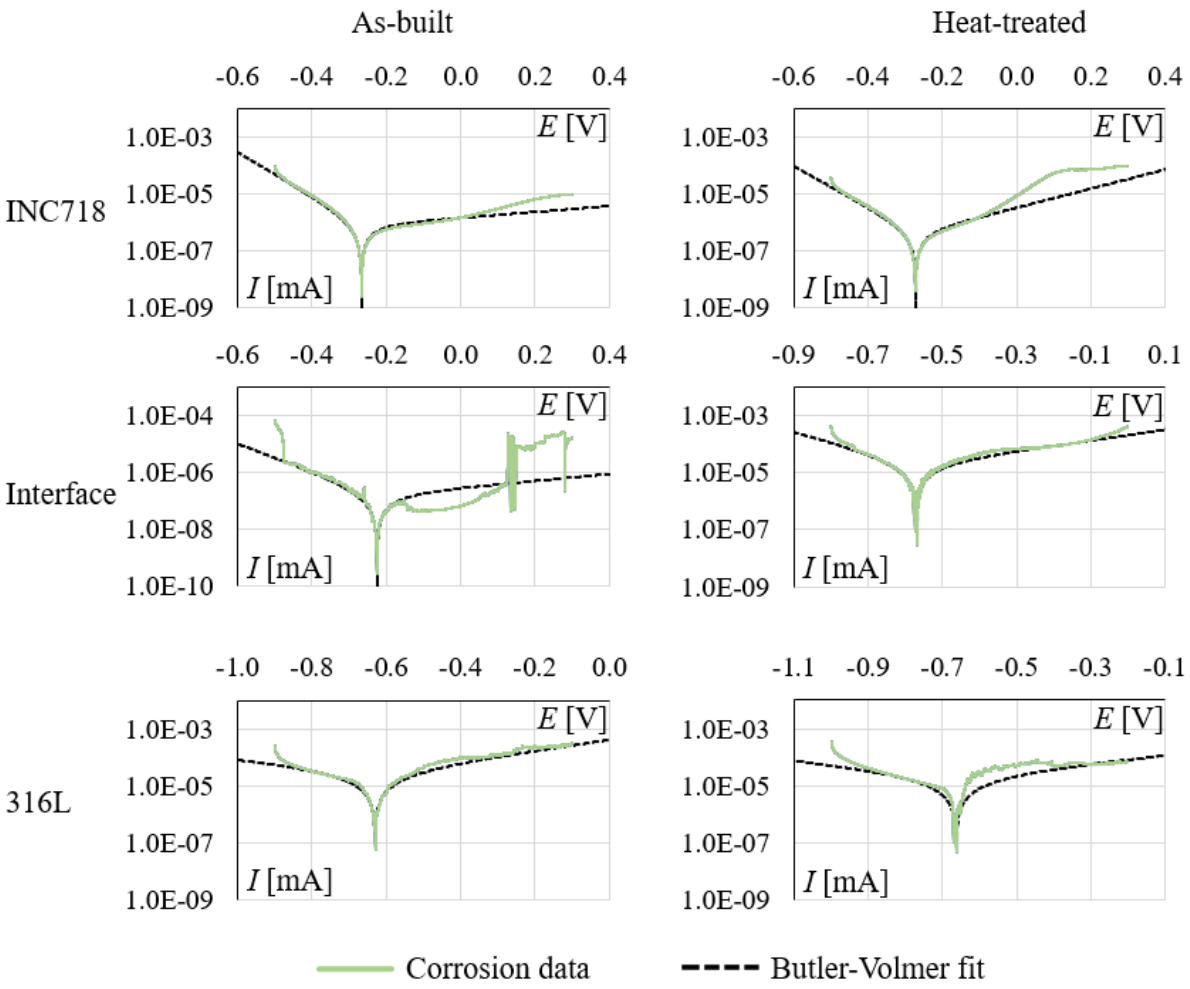

Figure 42. The raw data from the corrosion measurements and the Butler-Volmer equations fitted to them.

Figure 42 shows the corrosion data from each measurement. The anodic transfer coefficient determines the angle of the exponential plateau towards negative while the cathodic transfer coefficient determines the exponential plateau for the positive. It can be seen that when the measurement is begun at the minimum potential, the current decays exponentially to the anodic exponential plateau.

As seen in Figure 42, a secondary increase in current can be seen in the cathodic region of the IN718 current measurements both as-build and heat-treated. These increases in current beginning in the vicinity of -0.1 V and decelerating in the proximity to 0.2 V. This is speculated to be a secondary reaction beginning in the vicinity of -0.1 V, the growth of which then would plateau to its own cathodic transfer coefficient after 0.2 V, but this topic would require further study.

In Figure 42 there is a notable difference in the behavior of the corrosion samples for the interface between as-built and heat-treated. The behavior seen in the as-built current is speculated to occur due to porosity and powder which was not oxidized due to it not being heat-treated. However, this explanation does have a problem in the fact that any powder within lack-of-fusion pores inside the interface sample would have formed under the Argon atmosphere of the PBF-LB\M machine, and as such the amount of oxygen present to allow oxidation would be limited. As such, this behavior would require further research.

The measurements performed on 316L as shown in the Figure 42 can be seen to have noisy yet recognizable patterns.

Of note in the 316L corrosion behavior in Figure 42 is the anodic side in the vicinity of -0.7 V, with the data having a minute deviation compared to the Butler-Volmer equation fit. The deviation can be seen as a delay in the decrease of current when the anodic side approaches the equilibrium potential (E_{eq}). This could be the result of a lesser reaction with a lower anodic transfer coefficient but a slightly more positive equilibrium potential (E_{eq}). The feature of the sharper and later decrease to the equilibrium potential (E_{eq}) is speculated to be a linear combination of the currents caused by the proposed lesser reaction and the most prominent reaction in the system. However, further research is warranted.

Additionally in the cathodic side of the 316L measurements shown in Figure 42: there seems to be a ridge in the region of -0.7 V to -0.4 V which experiences its own plateau. This ridge being more pronounced for the heat-treated sample.

The noted behavior on both the anodic and cathodic sides for the 316L measurements seen in Figure 42 could be the effect of another, less prominent reaction occurring. This reaction having a similar equilibrium potential as the prominent equilibrium potential. This less prominent reaction also seemingly possessing a lower anodic and cathodic coefficient. However, further research would be warranted.

It is observed that the interface measurement for the as-built sample behaves more like the IN718 sample measurements. While the interface measurement for the heat treatment sample behaves more akin to the 316L sample measurements. This can be seen when comparing the values of E_{eq} and I_0 shown in Table 30 and Figure 42. This behavior was unexpected, and would warrant further research.

All of the above considerations and speculations are susceptible to the uncertainty of the data collected, due to the method being single sweep. Which is to say, there were no repeat potential sweep measurements for the current done for any of the 6 sample types.

12 Conclusions

The research conducted in this thesis shows that 316L-IN718 can be feasibly joined with PBF-LB\M. Additionally, the results indicate that heat treatment performs a crucial part in the performance of the bimetallic combination.

The manufacturability of the bimetallic combination of 316L-IN718 via PBF-LB\M was studied by manufacturing a set of workpieces where AMed 316L functioned as the substrate and IN718 was additively manufactured on top with varied parameters. The optimal parameters for the interface and porosity quality were determined by grading and a process of elimination.

A new set of workpieces were manufactured with the parameters chosen in the process of elimination and half of the workpieces were heat-treated with an IN718 focused heat treatment plan.

The porosity, microstructure, geometrical accuracy, hardness and corrosion behavior of the bimetallic combination were studied, in addition to the influence of the IN718 focused heat treatment on these characteristics.

The porosity and microstructure were analysed with microscopy, and micrographs were taken. Micrographs were analysed to determine observations about the microstructure and a Python program was developed to calculate the porosity visible in the micrographs. Heat treatment was determined to increase porosity, but with only a slight increase for IN718, with a notable increase for 316L, while the interface seemingly was an average of the IN718 and 316L values.

The geometrical accuracy was measured with a 3D surface analysis microscope. A point cloud was collected and later a line analysis was performed to the point cloud data. Geometrical accuracy was determined from the line analysis results. The geometrical accuracy results for both the as-built and heat-treated workpieces were within a reasonable margin from the ideal dimensions. Heat treatment did not seem to have a notable effect on the geometrical accuracy, as the results were similar between as-built and heat-treated. The greatest relative difference between the as-built and heat-treated deviations from the ideal measurements was in the rounding radius of 316L. However, it is questionable if this is due to the influence of the heat treatment, as the internal variance of the rounding radius measurement for any given sample may be greater than the influence of heat treatment.

As such the exact effect of heat treatment on the geometrical accuracy remains uncertain, but the findings suggest that the influence of heat treatment on the geometrical accuracy is limited.

Hardness tests were performed, and it was noted that heat treatment had significantly strengthened IN718, while slightly lowering the hardness of 316L. The interface was noted to have gained a slight increase in hardness after the heat treatment. Theory of the phases of IN718 and their microstructural influence on material was discussed.

Corrosion measurements were performed for corrosion samples cut from heat-treated and as-built workpieces. Corrosion experiments used a potentiostat and a 3,5% NaCl solution, the sample as the working electrode, a Ag/AgCl reference electrode and a graphite auxiliary electrode. The corrosion behavior was measured and the measurement results were analysed.

Corrosion rate was determined via potentiostat analysis and the Butler-Volmer equation was fitted to corrosion rate measurement data. The findings suggest that heat treatment increases the corrosion rate of IN718, 316L and the interface, with the greatest relative increase in corrosion rate post heat treatment being measured for the interface.

Overall, this thesis established an understanding of the PBF-LB\M of bimetallic 316L-IN718 and the properties of the bimetallic combination manufactured via PBF-LB.

All data will be made available upon request to the author or the University of Turku.

12.1 Synopsis of results

The main results are given again in this chapter.

Figure 43 shows the results of the porosity measurements.

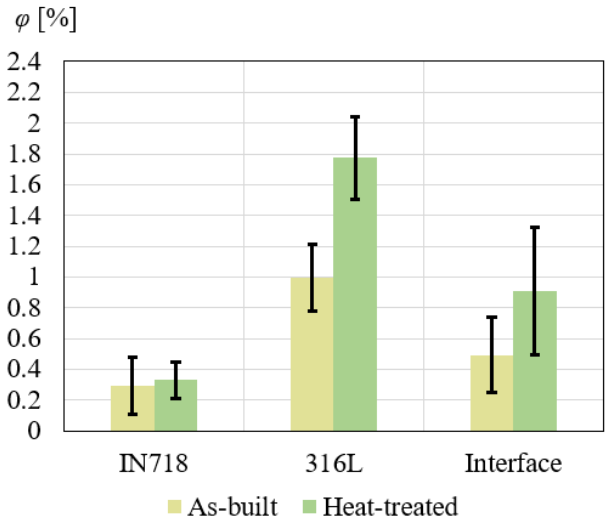

Figure 43. The 95% Confidence intervals for the levels of porosity of each type of measurement from Table 20 and Table 21 represented.

Figure 44 shows the results of the geometrical accuracy measurements.

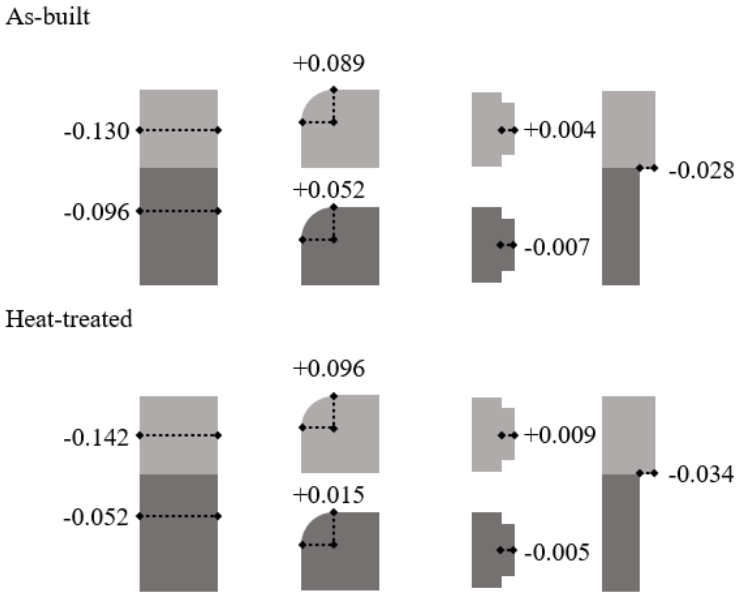

Figure 44. The deviation of the measured workpiece dimensions from the ideal workpiece dimensions given in millimeters. The negative sign signifies a dimension smaller than the ideal while a positive signifies opposite.

Figure 45 shows the results of the hardness measurements.

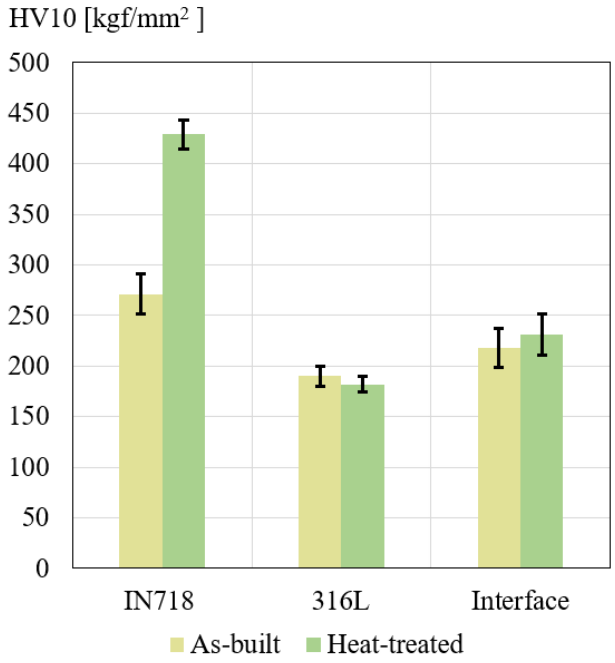

Figure 45. The 95% Confidence intervals for the HV10 values of each type of measurement from Table 25 and Table 26 represented.

Figure 46 shows the results of the corrosion rate measurements.

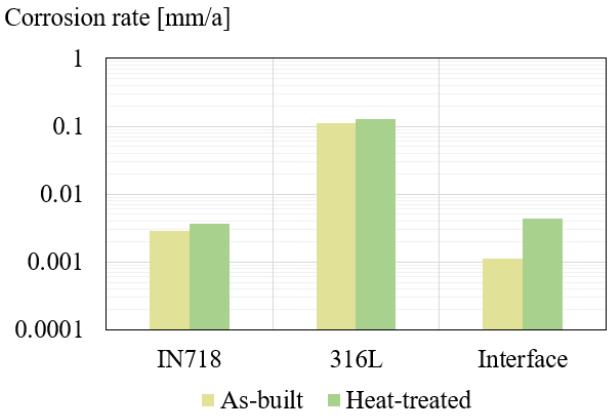

Figure 46. The results of the corrosion rate measurements. Note the logarithmic scale and the gridlines.

12.2 Future work

The project which governed this thesis had been limited in scope by regrettable circumstance. The foremost of which would be the unexpected inability for the thesis to include the dilatometry tests. Given this, it is concluded that a potential avenue of further study would be the dilatometry of 316L-IN718 pieces manufactured via PBF-LB\M.

Additionally, there were other aspects which were not measured in this project, namely tensile strength and wear resistance. The study of these would also be suitable future pursuits.

Furthermore, the original project outline defined the following aspects as out-of-scope:

- Fatigue investigation
- Computed tomography
- Residual stress analysis
- Helium leak test

Each of these could be set as an option for future study as well. To elaborate:

- Fatigue investigation would be ideal for the purposes of determining the limits and degree of viability of the bimetallic 316L-IN718 in industrial application.
- Computed tomography would allow for thorough analysis of the bimetallic 316L-IN718 material, with the ability to utilize a 3D visualization of defects and use this to possibly determine a connection between certain defects and different scanning strategies and process parameters as well as different heat treatments.
- Residual stress analysis, like fatigue investigation, would be important to study so that the real-world application of the bimetal could be ascertained.
- Helium leak tests would be another way to study the integrity of the microstructure of the material, and would be useful to know, if the material would be used in applications related to fluids.

Scanning electron microscopy and energy dispersive spectroscopy of the interface area are also suggested as avenues of further research, to allow for a more comprehensive understanding of the interface microstructure, porosity and metallurgical bonding.

Process simulation would also be an interesting aspect to study in the field of bimetals, as it would allow for cost effective ways to study phenomena, even if simulations would have to be confirmed with laboratory experiments.

A concept of using in-situ process monitoring techniques to corroborate with simulations is proposed as a potential research topic of interest.

13 Acknowledgements

A special thanks belongs to Muhammad Ammar Anjum for his contributions to the design of the experimental set-up, expert counsel during the project, operation of the PBF-LB\M machine for the purposes of manufacturing the workpieces and assistance in the preparation of the corrosion samples.

A special thanks also to Inka Väisänen and Eter Tourunen for their contribution in the geometrical accuracy measurements and operation of the Alicona microscope.

Senior research scientist Heidi Piili, assistant professor Mohsen Amrei, postdoctoral researcher Nikhil Kamboj and university lecturer Vigneashwara Pandiyan are thanked for their role of advisors in this thesis.

Heidi Piili is additionally thanked for her role of primary advisor in this thesis.

Professor Antti Salminen, docent Matti Murtomaa and associate professor Ashish Ganvir are thanked for their role of supervisor in this thesis.

Olivia Iizuka and Janne Hirvonen are thanked for their assistance and contributions in the project as fellow thesis authors in the project.

The Bimetallic Research Project shareholders are thanked for the funding of this thesis as well as the guidance and management of the project.

References

[1] I. H. ZainElabdeen, L. Ismail, O. F. Mohamed, K. A. Khan, and A. Schiffer, "Recent advancements in hybrid additive manufacturing of similar and dissimilar metals via laser powder bed fusion," *Materials Science and Engineering: A*, vol. 909, p. 146833, Sept. 2024, doi: 10.1016/j.msea.2024.146833.

[2] S. Lim, R. A. Buswell, T. T. Le, S. A. Austin, A. G. F. Gibb, and T. Thorpe, "Developments in construction-scale additive manufacturing processes," *Automation in Construction*, vol. 21, pp. 262–268, Jan. 2012, doi: 10.1016/j.autcon.2011.06.010.

[3] D. Chauhan, A. P. Singh, A. Chauhan, and R. Arora, "Sustainable supply chain: An optimization and resource efficiency in additive manufacturing for automotive spare part," *Sustainable Futures*, vol. 9, p. 100563, June 2025, doi: 10.1016/j.sftr.2025.100563.

[4] M. H. Razzaq, M. U. Zaheer, H. Asghar, O. C. Aktas, M. F. Aycan, and Y. K. Mishra, "Additive manufacturing for biomedical bone implants: Shaping the future of bones," *Materials Science and Engineering: R: Reports*, vol. 163, p. 100931, Apr. 2025, doi: 10.1016/j.mser.2025.100931.

[5] *Selective Laser Melting: Selective Laser Melting*. MDPI, 2020. doi: 10.3390/books978-3-03928-579-2.

[6] W. Ji, R. Zhou, P. Viveganantha n, M. See Wu, H. Gao, and K. Zhou, "Recent progress in gradient-structured metals and alloys," *Progress in Materials Science*, vol. 140, p. 101194, Dec. 2023, doi: 10.1016/j.pmatsci.2023.101194.

[7] H. Shen, J. Yan, and X. Niu, "Thermo-Fluid-Dynamic Modeling of the Melt Pool during Selective Laser Melting for AZ91D Magnesium Alloy," *Materials*, vol. 13, no. 18, p. 4157, Sept. 2020, doi: 10.3390/ma13184157.

[8] M. Liu *et al.*, "Effective thermal conductivities of metal powders for additive manufacturing," *Powder Technology*, vol. 401, p. 117323, Mar. 2022, doi: 10.1016/j.powtec.2022.117323.

[9] H. Yeung, B. Lane, J. Fox, F. Kim, J. Heigel, and J. Neira, *Continuous laser scan strategy for faster build speeds in laser powder bed fusion system*. 2017.

[10] J. Dar, A. G. Ponsot, C. J. Jolma, and D. Lin, "A review on scan strategies in laser-based metal additive manufacturing," *Journal of Materials Research and Technology*, vol. 36, pp. 5425–5467, May 2025, doi: 10.1016/j.jmrt.2025.04.068.

[11] J. Zhu, H. Zhou, C. Wang, L. Zhou, S. Yuan, and W. Zhang, "A review of topology optimization for additive manufacturing: Status and challenges," *Chinese Journal of Aeronautics*, vol. 34, no. 1, pp. 91–110, Jan. 2021, doi: 10.1016/j.cja.2020.09.020.

[12] C. B. Dilgen, S. B. Dilgen, D. R. Fuhrman, O. Sigmund, and B. S. Lazarov, "Topology optimization of turbulent flows," *Computer Methods in Applied Mechanics and Engineering*, vol. 331, pp. 363–393, Apr. 2018, doi: 10.1016/j.cma.2017.11.029.

[13] X. Wang *et al.*, "Topology-optimized heat sinks with superior thermo-mechanical properties fabricated by laser powder bed fusion," *Applied Thermal Engineering*, vol. 263, p. 125359, Mar. 2025, doi: 10.1016/j.applthermaleng.2024.125359.

[14] K. Cui, H. Zhao, Z. Zhang, T. Han, K. He, and X. Yan, "Investigations into hydrothermal performance of porous-ribbed microchannels based on topology optimizations," *Applied Thermal Engineering*, vol. 279, p. 127850, Nov. 2025, doi: 10.1016/j.applthermaleng.2025.127850.

[15] W. Fang, J. Sang, H. Li, S. Yin, and Y. Huang, "Development of hydrodynamic and thermal boundary layer in the entrance region with hydrophobic surfaces," *International Journal of Heat and Mass Transfer*, vol. 253, p. 127618, Dec. 2025, doi: 10.1016/j.ijheatmasstransfer.2025.127618.

[16] S. Mohd Yusuf *et al.*, “Microstructures and Hardening Mechanisms of a 316L Stainless Steel/Inconel 718 Interface Additively Manufactured by Multi-Material Selective Laser Melting,” *Metals*, vol. 13, no. 2, p. 400, Feb. 2023, doi: 10.3390/met13020400.

[17] A. Hinojos *et al.*, “Joining of Inconel 718 and 316 Stainless Steel using electron beam melting additive manufacturing technology,” *Materials & Design*, vol. 94, pp. 17–27, Mar. 2016, doi: 10.1016/j.matdes.2016.01.041.

[18] A. Paraschiv, G. Matache, M. R. Condruz, T. F. Frigioescu, and L. Pambaguian, “Laser Powder Bed Fusion Process Parameters’ Optimization for Fabrication of Dense IN 625,” *Materials*, vol. 15, no. 16, p. 5777, Aug. 2022, doi: 10.3390/ma15165777.

[19] J. Grünewald, P. Clarkson, R. Salveson, G. Fey, and K. Wudy, “Influence of Pulsed Exposure Strategies on Overhang Structures in Powder Bed Fusion of Ti6Al4V Using Laser Beam,” *Metals*, vol. 11, no. 7, p. 1125, July 2021, doi: 10.3390/met11071125.

[20] A. Hussain and D. Kim, “Fabrication of metal alloy structures with overhang features in laser-based powder bed fusion: A critical review of challenges and latest developments,” *Journal of Manufacturing Processes*, vol. 135, pp. 112–130, Feb. 2025, doi: 10.1016/j.jmapro.2025.01.031.

[21] I. Günther, B. Zillmann, and T. Niendorf, “Metal powder bed fusion of pure and coated copper for power electronics applications using a green laser,” *Journal of Materials Research and Technology*, vol. 38, pp. 5250–5262, Sept. 2025, doi: 10.1016/j.jmrt.2025.09.007.

[22] F. Ahsan, J. Razmi, and L. Ladani, “Experimental measurement of thermal diffusivity, conductivity and specific heat capacity of metallic powders at room and high temperatures,” *Powder Technology*, vol. 374, pp. 648–657, Sept. 2020, doi: 10.1016/j.powtec.2020.07.043.

[23] F. M. Carter *et al.*, “Melt pool instability detection using coaxial photodiode system validated by in-situ X-ray imaging,” *CIRP Annals*, vol. 72, no. 1, pp. 205–208, 2023, doi: 10.1016/j.cirp.2023.03.031.

[24] B. Cox, M. Ghayoor, S. Pasebani, and J. Gess, “Tracking of Marangoni driven motion during laser powder bed fusion,” *Powder Technology*, vol. 425, p. 118610, July 2023, doi: 10.1016/j.powtec.2023.118610.

[25] Y. Zhang, S. Wu, Z. Guo, G. Peng, L. Wang, and W. Yan, “Defects caused by powder spattering and entrainment in laser powder bed fusion process: High-fidelity modeling of gas, melt pool and powder dynamics,” *Acta Materialia*, vol. 288, p. 120816, Apr. 2025, doi: 10.1016/j.actamat.2025.120816.

[26] Z. Zhang, T. Zhang, C. Sun, S. Karna, and L. Yuan, “Understanding Melt Pool Behavior of 316L Stainless Steel in Laser Powder Bed Fusion Additive Manufacturing,” *Micromachines*, vol. 15, no. 2, p. 170, Jan. 2024, doi: 10.3390/mi15020170.

[27] Z. Tao, A. Thanki, L. Goossens, A. Witvrouw, B. Vrancken, and W. Dewulf, “Data-driven keyhole pore detection in laser powder bed fusion: Integrating process insights with X-CT,” *Journal of Manufacturing Processes*, vol. 142, pp. 293–316, May 2025, doi: 10.1016/j.jmapro.2025.03.107.

[28] M. Jaskari *et al.*, “Effects of volumetric energy density on defect structure and fatigue behaviour of powder bed fusion manufactured 316L stainless steel,” *Materials Science and Engineering: A*, vol. 925, p. 147868, Mar. 2025, doi: 10.1016/j.msea.2025.147868.

[29] G. Huang, K. Wei, J. Deng, M. Liu, and X. Zeng, “High-power laser powder bed fusion of 316L stainless steel: Defects, microstructure, and mechanical properties,” *Journal of Manufacturing Processes*, vol. 83, pp. 235–245, Nov. 2022, doi: 10.1016/j.jmapro.2022.08.066.

[30] K. Zhuang, C. Hu, J. Zhou, and R. Lin Peng, “Investigation on work hardening phenomenon in turning Inconel 718 with chamfered inserts considering thermal-mechanical loads,” *Procedia CIRP*, vol. 87, pp. 47–52, 2020, doi: 10.1016/j.procir.2020.02.071.

[31] S. Zhang *et al.*, “Optimizing the corrosion resistance of selective laser melted 316L austenitic stainless steel by adjusting solid solution treatment parameters,” *Vacuum*, vol. 241, p. 114631, Nov. 2025, doi: 10.1016/j.vacuum.2025.114631.

[32] X. Mei, X. Wang, Y. Peng, H. Gu, G. Zhong, and S. Yang, “Interfacial characterization and mechanical properties of 316L stainless steel/inconel 718 manufactured by selective laser melting,” *Materials Science and Engineering: A*, vol. 758, pp. 185–191, June 2019, doi: 10.1016/j.msea.2019.05.011.

[33] W. W. Wits and E. Amsterdam, “Graded structures by multi-material mixing in laser powder bed fusion,” *CIRP Annals*, vol. 70, no. 1, pp. 159–162, 2021, doi: 10.1016/j.cirp.2021.03.005.

[34] S. P. Singh, A. Aggarwal, R. K. Upadhyay, and A. Kumar, “Processing of IN718-SS316L bimetallic-structure using laser powder bed fusion technique,” *Materials and Manufacturing Processes*, vol. 36, no. 9, pp. 1028–1039, July 2021, doi: 10.1080/10426914.2021.1885701.

[35] Y. Bai, C. Zhao, Y. Zhang, and H. Wang, “Microstructure and mechanical properties of additively manufactured multi-material component with maraging steel on CrMn steel,” *Materials Science and Engineering: A*, vol. 802, p. 140630, Jan. 2021, doi: 10.1016/j.msea.2020.140630.

[36] W. M. Tucho *et al.*, “Effects of δ Phase and Annealing Twins on Mechanical Properties and Impact Toughness of L-PBF Inconel 718,” *JMMP*, vol. 8, no. 4, p. 135, June 2024, doi: 10.3390/jmmp8040135.

[37] S. Mohd Yusuf, X. Zhao, S. Yang, and N. Gao, “Interfacial characterisation of multi-material 316L stainless steel/Inconel 718 fabricated by laser powder bed fusion,” *Materials Letters*, vol. 284, p. 128928, Feb. 2021, doi: 10.1016/j.matlet.2020.128928.

[38] R. Ghanavati, E. Lannunziata, E. Norouzi, S. Bagherifard, L. Iuliano, and A. Saboori, “Design and development of SS316L-IN718 functionally graded materials via laser powder bed fusion,” *Materials Letters*, vol. 349, p. 134793, Oct. 2023, doi: 10.1016/j.matlet.2023.134793.

[39] M.-S. Duval-Chaneac *et al.*, “Effect of heat treatment on fatigue crack growth in IN718/316L multiple-materials layered structures fabricated by laser powder bed fusion,” *International Journal of Fatigue*, vol. 160, p. 106852, July 2022, doi: 10.1016/j.ijfatigue.2022.106852.

[40] M. S. Duval-Chaneac *et al.*, “Fatigue crack growth in IN718/316L multi-materials layered structures fabricated by laser powder bed fusion,” *International Journal of Fatigue*, vol. 152, p. 106454, Nov. 2021, doi: 10.1016/j.ijfatigue.2021.106454.

[41] S. Sahu, J. Harris, A. R. Hamilton, and N. Gao, “Interfacial characteristics of multi-material SS316L/IN718 fabricated by laser powder bed fusion and processed by high-pressure torsion,” *Journal of Manufacturing Processes*, vol. 110, pp. 52–69, Jan. 2024, doi: 10.1016/j.jmapro.2023.12.051.

[42] L. Yao, S. Huang, U. Ramamurty, and Z. Xiao, “On the formation of ‘Fish-scale’ morphology with curved grain interfacial microstructures during selective laser melting of dissimilar alloys,” *Acta Materialia*, vol. 220, p. 117331, Nov. 2021, doi: 10.1016/j.actamat.2021.117331.

[43] S. Wen, K. Chen, Y. Che, Y. Liu, J. Gan, and Y. Zhou, “Tailored microstructure and robust joint of Inconel 718/316L bimetallic multi-material fabricated by selective laser melting,” Dec. 07, 2020. doi: 10.21203/rs.3.rs-118341/v1.

[44] Z. Li *et al.*, “Selective laser melting of 316L–CuCrZr bimetallic structure via IN718 transition layer,” *Journal of Materials Research and Technology*, vol. 25, pp. 3819–3834, July 2023, doi: 10.1016/j.jmrt.2023.06.196.

[45] Y. Wen *et al.*, “Microstructure-property correlations in as-built and heat-treated compositionally graded stainless steel 316L-Inconel 718 alloy fabricated by laser powder bed fusion,” *Materials Science and Engineering: A*, vol. 862, p. 144515, Jan. 2023, doi: 10.1016/j.msea.2022.144515.

[46] A. Angelastro, P. Posa, V. Errico, and S. L. Campanelli, “A Systematic Study on Layer-Level Multi-Material Fabrication of Parts via Laser-Powder Bed Fusion Process,” *Metals*, vol. 13, no. 9, p. 1588, Sept. 2023, doi: 10.3390/met13091588.

[47] K. Gruber, W. Stopyra, K. Kobiela, B. Madejski, M. Malicki, and T. Kurzynowski, “Mechanical properties of Inconel 718 additively manufactured by laser powder bed fusion after industrial high-temperature heat treatment,” *Journal of Manufacturing Processes*, vol. 73, pp. 642–659, Jan. 2022, doi: 10.1016/j.jmapro.2021.11.053.

[48] G. M. Domínguez Almaraz, M. G. Tapia, and I. F. Zuñiga Tello, “Ultrasonic fatigue endurance of Inconel 718 after the heat treatments: solution annealing and double aging,” *Procedia Structural Integrity*, vol. 39, pp. 281–289, 2022, doi: 10.1016/j.prostr.2022.03.098.

[49] C. Slama, C. Servant, and G. Cizeron, “Aging of the Inconel 718 alloy between 500 and 750 °C,” *J. Mater. Res.*, vol. 12, no. 9, pp. 2298–2316, Sept. 1997, doi: 10.1557/JMR.1997.0306.

[50] “316L ASTM A276 / DIN EN 10088 / 1.4404 MATERIAL DATA SHEET.” SLM Solutions, 2024. [Online]. Available: https://www.slm-solutions.com/fileadmin/Content/Powder/MDS/nw/nw2024/mds5130.pdf

[51] “IN718 ASTM F3055 / ASTM B637 / AMS5664 MATERIAL DATA SHEET.” SLM Solutions, 2024. [Online]. Available: https://www.slm-solutions.com/fileadmin/Content/Powder/MDS/nw/2024/MDS_IN718_2024-04.1_EN.pdf

[52] “Open-source multi-material metal and ceramic 3D printer – Aconity MIDI+ | University of Turku.” Accessed: Oct. 10, 2025. [Online]. Available: https://www.utu.fi/en/susfab/equipment/open_source_multi_material_metal_ceramic_3d_printer_aconity_midi

[53] “Aconity3D GmbH - Additive Manufacturing,” Aconity3D. Accessed: Oct. 10, 2025. [Online]. Available: https://aconity3d.com/

[54] “AE2000MET trinocular AE2000MET Series.” Accessed: Oct. 10, 2025. [Online]. Available: https://www.motic.com/As_Industrial_AE2000MET/product_477.html

[55] “Optical 3D Surface Roughness Measurement Instrument - Alicona.” Accessed: Oct. 10, 2025. [Online]. Available: https://www.alicona.com/en/products/infinitefocus

[56] C. Morano and L. Pagnotta, “On Powder Bed Fusion Manufactured Parts: Porosity and its Measurement,” *CMS*, vol. 17, no. 3, pp. 185–197, Sept. 2024, doi: 10.2174/2666145416666230427093421.

[57] A. C. Fischer-Cripps, “The measurement of hardness of very hard materials,” *Surface and Coatings Technology*, vol. 291, pp. 314–317, Apr. 2016, doi: 10.1016/j.surfcoat.2016.02.063.

[58] R. J. Brook, R. W. Cahn, and M. B. Bever, *Concise encyclopedia of advanced ceramic materials*, 1st ed. in Advances in materials science and engineering. Oxford New York Cambridge, Mass., USA: Pergamon Press Distributed in North and South America by the MIT Press, 1991.

[59] “Potentiostat - an overview | ScienceDirect Topics.” Accessed: Nov. 07, 2025. [Online]. Available: https://www.sciencedirect.com/topics/engineering/potentiostat

[60] R. A. Serway, *Physics for scientists & engineers, with modern physics*, 4th ed. in Saunders golden sunburst series. Philadelphia: Saunders College Pub, 1996.
[61] T. F. Fuller and J. N. Harb, *Electrochemical engineering*. Hoboken, NJ: Wiley, 2018.
[62] R. C. Alkire, D. M. Kolb, L. A. Kibler, and J. Lipkowski, *Electrocatalysis: theoretical foundations and model experiments*. in Advances in electrochemical sciences and engineering, no. 14. Weinheim: Wiley-VCH, 2013.
[63] E. J. F. Dickinson and A. J. Wain, "The Butler-Volmer equation in electrochemical theory: Origins, value, and practical application," *Journal of Electroanalytical Chemistry*, vol. 872, p. 114145, Sept. 2020, doi: 10.1016/j.jelechem.2020.114145.
[64] B. Sundén, "Transport phenomena in batteries," in *Hydrogen, Batteries and Fuel Cells*, Elsevier, 2019, pp. 81–91. doi: 10.1016/B978-0-12-816950-6.00005-1.
[65] "Butler-Volmer Kinetics - an overview | ScienceDirect Topics." Accessed: Oct. 13, 2025. [Online]. Available: https://www.sciencedirect.com/topics/engineering/butler-volmer-kinetics
[66] M. Ganta, M. Kurek, A. Emdadi, T. Łagoda, and M. Pagáč, "Effect of powder recycling on powder characteristics and mechanical properties of materials produced by laser powder bed fusion (LPBF): A review," *Sustainable Materials and Technologies*, vol. 46, p. e01714, Dec. 2025, doi: 10.1016/j.susmat.2025.e01714.
[67] Z. Snow, A. R. Nassar, and E. W. Reutzel, "Invited Review Article: Review of the formation and impact of flaws in powder bed fusion additive manufacturing," *Additive Manufacturing*, vol. 36, p. 101457, Dec. 2020, doi: 10.1016/j.addma.2020.101457.
[68] J. K. Veetil *et al.*, "Build position-based dimensional deviations of laser powder-bed fusion of stainless steel 316L," *Precision Engineering*, vol. 67, pp. 58–68, Jan. 2021, doi: 10.1016/j.precisioneng.2020.09.024.
[69] P. R. Gradl, D. C. Tinker, J. Ivester, S. W. Skinner, T. Teasley, and J. L. Bili, "Geometric feature reproducibility for laser powder bed fusion (L-PBF) additive manufacturing with Inconel 718," *Additive Manufacturing*, vol. 47, p. 102305, Nov. 2021, doi: 10.1016/j.addma.2021.102305.
[70] C. Slama and M. Abdellaoui, "Precipitation kinetics of γ′ and γ″ particles in Inconel 718 and its influence on mechanical properties," *Materials Today Communications*, vol. 38, p. 108158, Mar. 2024, doi: 10.1016/j.mtcomm.2024.108158.
[71] S. Zhang, C. Guo, X. Lin, H. Zhao, H. Yang, and W. Huang, "Deformation behavior of selective laser-melted Inconel 718 superalloy," *Materials Characterization*, vol. 216, p. 114180, Oct. 2024, doi: 10.1016/j.matchar.2024.114180.
[72] M. Sundararaman, P. Mukhopadhyay, and S. Banerjee, "Deformation behaviour of γ″ strengthened inconel 718," *Acta Metallurgica*, vol. 36, no. 4, pp. 847–864, Apr. 1988, doi: 10.1016/0001-6160(88)90139-3.
[73] P. Suárez Ocaño *et al.*, "Effect of 700–900 °C heat treatments and room and high temperature tensile deformation on the microstructure of laser powder bed fused 316L stainless steel," *Materials Science and Engineering: A*, vol. 939, p. 148469, Sept. 2025, doi: 10.1016/j.msea.2025.148469.
[74] S. Naskar, S. Suryakumar, and B. B. Panigrahi, "Post-processing of Inconel 718 superalloy by Laser-based Powder Bed Fusion: Microstructures and properties evaluation," *Materials Science and Engineering: A*, vol. 921, p. 147601, Jan. 2025, doi: 10.1016/j.msea.2024.147601.
[75] K. Grzelak *et al.*, "A Comparative Study on Laser Powder Bed Fusion of Differently Atomized 316L Stainless Steel," *Materials*, vol. 15, no. 14, p. 4938, July 2022, doi: 10.3390/ma15144938.
[76] A. Siddaiah, A. Kasar, P. Kumar, J. Akram, M. Misra, and P. L. Menezes, "Tribocorrosion Behavior of Inconel 718 Fabricated by Laser Powder Bed Fusion-Based

Additive Manufacturing," *Coatings*, vol. 11, no. 2, p. 195, Feb. 2021, doi: 10.3390/coatings11020195.

[77] O. V. Mythreyi, B. K. Nagesha, and R. Jayaganthan, "Microstructural evolution & corrosion behavior of Laser –powder-bed–fused Inconel 718 subjected to surface and heat treatments," *Journal of Materials Research and Technology*, vol. 19, pp. 3201–3215, July 2022, doi: 10.1016/j.jmrt.2022.05.123.

[78] M. A. S. Yousif, I. A. Al-Deheish, U. Ali, S. S. Akhtar, and K. S. Al-Athel, "Mechanical, tribological, and corrosion behavior of laser powder-bed fusion 316L stainless steel parts: Effect of build orientation," *Journal of Materials Research and Technology*, vol. 33, pp. 1220–1233, Nov. 2024, doi: 10.1016/j.jmrt.2024.09.105.

[79] L. Xing, J. Xuan, and P. K. Das, "Fuel cell fundamentals," in *Fuel Cells for Transportation*, Elsevier, 2023, pp. 29–72. doi: 10.1016/B978-0-323-99485-9.00006-X.

[80] "Exchange Current Density - an overview | ScienceDirect Topics." Accessed: Oct. 16, 2025. [Online]. Available: https://www.sciencedirect.com/topics/engineering/exchange-current-density

Appendices

Appendix 1. Use of AI in the Thesis.

No AI was used in this thesis.

Appendix 2. Corrosion measurement data

All corrosion measurement data will be made available upon request to the author or the University of Turku.

The “Eoc monitor” measurement results are seen in Figure 47, Figure 48 and Figure 49, where the measured potential (E) is shown as a function of measurement time (τ).

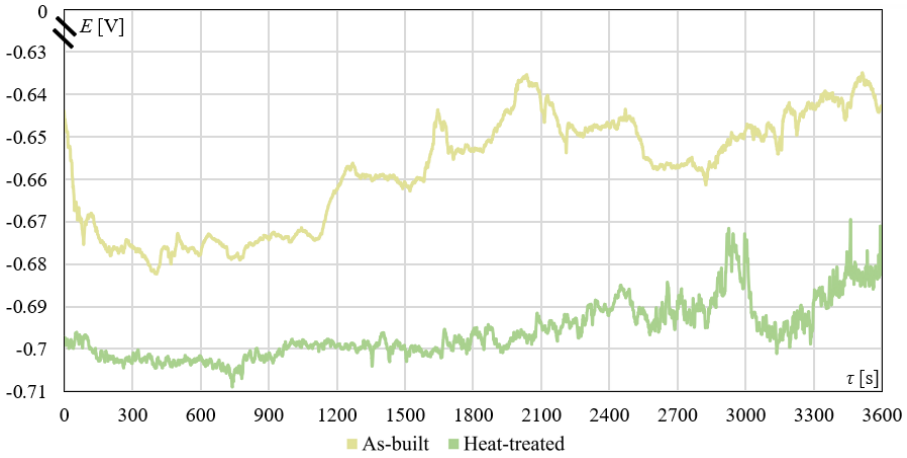

Figure 47. The Eoc monitor measurement data for the as-built and heat-treated corrosion samples for 316L.

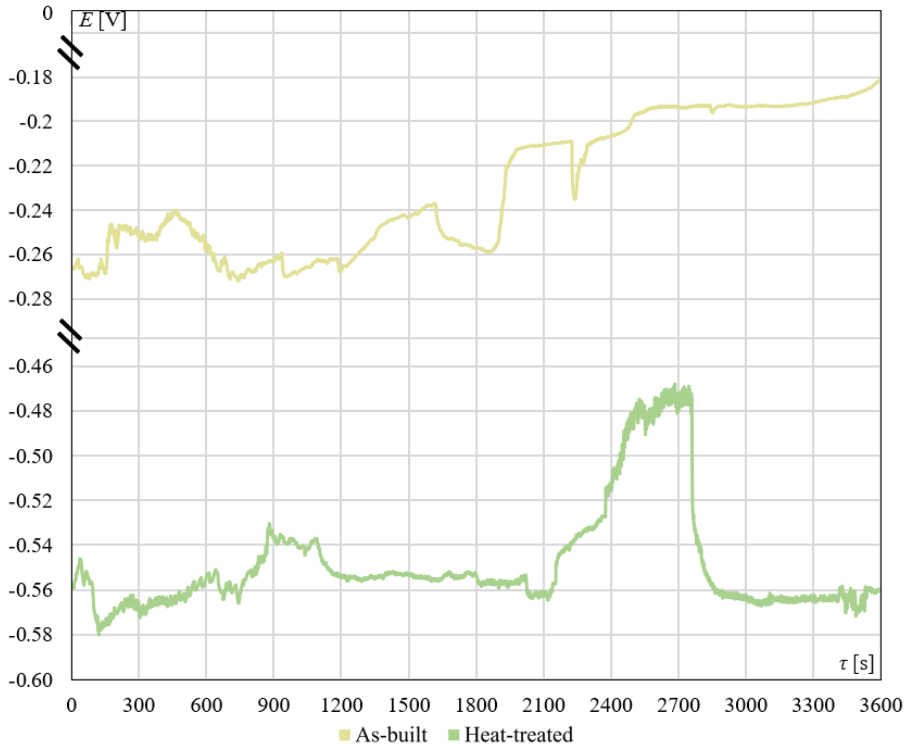

Figure 48. The Eoc monitor measurement data for the as-built and heat-treated corrosion samples for the interface.

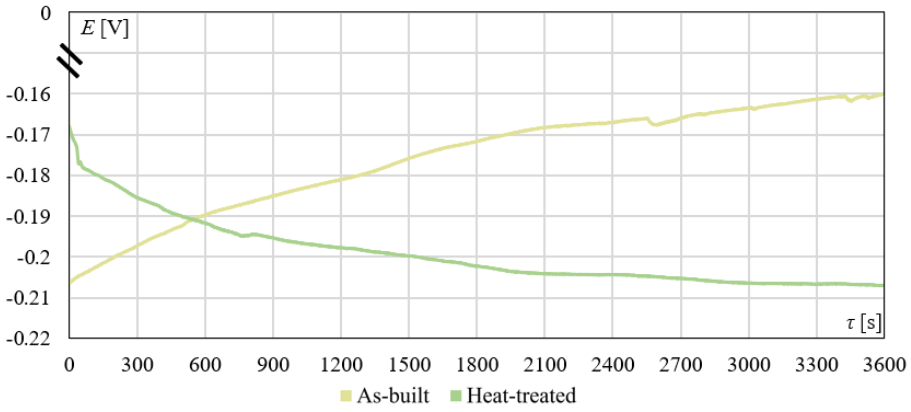

Figure 49. The Eoc monitor measurement data for the as-built and heat-treated corrosion samples for IN718.